

The background of the cover features a complex, geometric structure of red and white metal beams, resembling a truss or a modern architectural framework, set against a clear blue sky. The structure is composed of numerous intersecting lines that create a sense of depth and complexity.

IntechOpen

# Array Pattern Optimization

*Edited by Jafar Ramadhan Mohammed  
and Khalil Hassan Sayidmarie*





---

# Array Pattern Optimization

*Edited by Jafar Ramadhan Mohammed  
and Khalil Hassan Sayidmarie*

Published in London, United Kingdom

---



## IntechOpen





*Supporting open minds since 2005*



Array Pattern Optimization

<http://dx.doi.org/10.5772/intechopen.73353>

Edited by Jafar Ramadhan Mohammed and Khalil Hassan Sayidmarie

#### Contributors

Vincenzo Inzillo, Alfonso Ariza Quintana, Floriano De Rango, Luigi Zampogna, Daehee Park, Dong-Ho Cho, Daniele Inserra, Guangjun Wen, Mikhail Belkin, Dmitriy Fofanov, Vladislav Golovin, Yuri Tyschuk, Alexander Sigov, Jafar Ramadhan Mohammed, Khalil Sayidmarie

© The Editor(s) and the Author(s) 2019

The rights of the editor(s) and the author(s) have been asserted in accordance with the Copyright, Designs and Patents Act 1988. All rights to the book as a whole are reserved by INTECHOPEN LIMITED. The book as a whole (compilation) cannot be reproduced, distributed or used for commercial or non-commercial purposes without INTECHOPEN LIMITED's written permission. Enquiries concerning the use of the book should be directed to INTECHOPEN LIMITED rights and permissions department ([permissions@intechopen.com](mailto:permissions@intechopen.com)).

Violations are liable to prosecution under the governing Copyright Law.



Individual chapters of this publication are distributed under the terms of the Creative Commons Attribution 3.0 Unported License which permits commercial use, distribution and reproduction of the individual chapters, provided the original author(s) and source publication are appropriately acknowledged. If so indicated, certain images may not be included under the Creative Commons license. In such cases users will need to obtain permission from the license holder to reproduce the material. More details and guidelines concerning content reuse and adaptation can be found at <http://www.intechopen.com/copyright-policy.html>.

#### Notice

Statements and opinions expressed in the chapters are those of the individual contributors and not necessarily those of the editors or publisher. No responsibility is accepted for the accuracy of information contained in the published chapters. The publisher assumes no responsibility for any damage or injury to persons or property arising out of the use of any materials, instructions, methods or ideas contained in the book.

First published in London, United Kingdom, 2019 by IntechOpen

eBook (PDF) Published by IntechOpen, 2019

IntechOpen is the global imprint of INTECHOPEN LIMITED, registered in England and Wales, registration number: 11086078, The Shard, 25th floor, 32 London Bridge Street

London, SE19SG – United Kingdom

Printed in Croatia

British Library Cataloguing-in-Publication Data

A catalogue record for this book is available from the British Library

Additional hard and PDF copies can be obtained from [orders@intechopen.com](mailto:orders@intechopen.com)

Array Pattern Optimization

Edited by Jafar Ramadhan Mohammed and Khalil Hassan Sayidmarie

p. cm.

Print ISBN 978-1-78985-741-2

Online ISBN 978-1-78985-742-9

eBook (PDF) ISBN 978-1-83962-097-3

# We are IntechOpen, the world's leading publisher of Open Access books Built by scientists, for scientists

**4,100+**

Open access books available

**116,000+**

International authors and editors

**120M+**

Downloads

**151**

Countries delivered to

Our authors are among the  
**Top 1%**

most cited scientists

**12.2%**

Contributors from top 500 universities



**WEB OF SCIENCE™**

Selection of our books indexed in the Book Citation Index  
in Web of Science™ Core Collection (BKCI)

Interested in publishing with us?  
Contact [book.department@intechopen.com](mailto:book.department@intechopen.com)

Numbers displayed above are based on latest data collected.  
For more information visit [www.intechopen.com](http://www.intechopen.com)







# Meet the editors



Jafar Ramadhan Mohammed received his B.Sc. and M.Sc. degrees in Electronic and Communication Engineering from Mosul University, Mosul, IRAQ in 1998, and 2001, respectively, and his Ph.D. degree in Digital Communication Engineering from Panjab University, INDIA in 2009. He worked as senior lecturer at the Faculty of Electronic and Computer Engineering, Malaysia Technical University Melaka (UTeM), Melaka, Malaysia in 2011 and was a visiting researcher at Autonomia University of Madrid, Spain in 2013. He is currently an Assistant Professor and Vice Chancellor for Scientific Affairs at Ninevah University, Mosul, IRAQ. He has authored more than 45 scientific articles in international peer-refereed journals and conference proceedings. His main research interests are in the area of adaptive signal processing, antenna array synthesis, array pattern optimization, and interference suppression. In 2011, he was listed in the Marquis Who's Who Professionals in the World for Science and Engineering field (Edition 28). In 2018, he was selected for the Marquis Who's Who Lifetime Achievement Award.



Khalil Sayidmarie received his B.Sc. degree in Electronic and Communication Engineering from Mosul University, Iraq, in 1976, and his Ph.D. degree from Sheffield University, U.K. in 1981. He then joined the College of Engineering/Mosul University in 1983 and was promoted to full Professor in 1992. He worked as the head of the Electrical Engineering Department, University of Mosul for 9 years, and was the manager of the engineering consulting bureau, University of Mosul for 5 years. He was the acting dean of the College of Electronic Engineering at Mosul University from 2002 to 2003. Sayidmarie worked as a Professor of communication engineering at the College of Engineering, University of Amman, /Jordan from 2006 to 2009, where he was the dean of the Faculty of Engineering for the academic year 2008-2009. Sayidmarie has been Professor of communication engineering at the College of Electronic Engineering, Ninevah University since 2002. Sayidmarie's research interests cover antennas, propagation, and microwaves, and he has published more than 120 papers and has supervised 38 Ph.D. and M.Sc. theses.



# Contents

<b>Preface</b>	<b>XIII</b>
<b>Chapter 1</b> Introductory Chapter: Introduction to Array Pattern Optimization <i>by Khalil H. Sayidmarie and Jafar Ramadhan Mohammed</i>	<b>1</b>
<b>Chapter 2</b> Sidelobe Nulling by Optimizing Selected Elements in the Linear and Planar Arrays <i>by Jafar Ramadhan Mohammed and Khalil H. Sayidmarie</i>	<b>7</b>
<b>Chapter 3</b> Array Pattern Synthesis for ETC Applications <i>by Daniele Inserra and Guangjun Wen</i>	<b>31</b>
<b>Chapter 4</b> Design and Optimization of Photonics-Based Beamforming Networks for Ultra-Wide mmWave-Band Antenna Arrays <i>by Mikhail E. Belkin, Dmitriy Fofanov, Vladislav Golovin, Yuriy Tyschuk and Alexander S. Sigov</i>	<b>47</b>
<b>Chapter 5</b> Array Pattern Based on Integrated Antenna <i>by Daehee Park and Dong-Ho Cho</i>	<b>69</b>
<b>Chapter 6</b> Smart Antenna Systems Model Simulation Design for 5G Wireless Network Systems <i>by Vincenzo Inzillo, Floriano De Rango, Luigi Zampogna and Alfonso A. Quintana</i>	<b>87</b>



# Preface

With the increasing demand for antennas and narrow beam widths with beam steering capabilities, array antennas have become a wise choice as they offer versatile and flexible solutions for desired radiation patterns. The radiated field of the array depends on the main design parameters, such as the geometrical layout of the elements and their spacings, the excitation in amplitude, and/or phase of the individual elements, and finally the pattern of the individual elements. Many array synthesis techniques that use either analytical or numerical approaches have been extensively employed to improve the radiation pattern of the array. This book addresses recent techniques that aim to improve and optimize the radiation pattern of the array antenna. The book presents a concerted set of issues related to design concepts and methodologies that have recently been proposed to develop and improve the radiation characteristics of antenna arrays.

While most of the array pattern synthesis approaches deal with all of the elements of the array antenna, recent techniques try to offer easier solutions as only a limited number of the elements need to have their magnitudes and/or phases adjusted. Such approaches reduce the cost and complexity of the optimization process by dealing with a small number of selected elements. Whether dealing with all the array elements or a selected number of them, the analytical approaches give better insight and a more explicit way to synthesize the desired pattern. However, global numerical optimization methods have easier and shorter paths towards achieving better performance and optimum results. As the distribution of the power density in the near field of the array is required in some applications, the problem of array synthesis using numerical approaches becomes more desirable than using analytical ways as the latter will involve lengthy and cumbersome derivations.

Beamforming techniques have been an important approach to the design and optimization of the array pattern. Here the array elements are fed through a network that furnishes the phases and magnitudes necessary to obtain the desired radiation pattern. This approach offers the capability to employ various algorithms that are intended for the next generation ultra-wideband millimeter-wave phased array antennas. This book tries to augment this recent issue to the field of array synthesis.

In compliance with the development of massive MIMO and beamforming techniques in 5G technology, increasing the number of antenna elements has become an issue for further concern. The integrated antenna, which is composed of multiple antenna elements, can be a promising candidate for the next generation of technologies. The Smart Antenna Systems (SAS) and Massive MIMO systems are giving a strong and increasing impact relative to 5G wireless communication systems. They offer many benefits in terms of performance improvements with respect to omnidirectional antennas.

Therefore, this book aims to provide a good reference for practicing engineers as well as postgraduate students and researchers working in the field of antenna arrays. The book uses fundamental concepts that are necessary to explain the recent applications to provide a base on which the interested reader can either acquire new

knowledge about antenna array or furnish a platform for improving the existing antenna arrays for modern applications. The book can also serve as a useful tool for researchers (academia and industry) to draw inspiration for the design and development of array antennas for next-generation systems. This book is recommended for researchers and professionals in the field and may be used as a supplementary reference book on array antennas as it offers a concise guide for students and readers interested in studying arrays and their design optimization.

**Jafar Ramadhan Mohammed**  
College of Electronic Engineering,  
Ninevah University, Mosul, Iraq

**Khalil Hassan Sayidmarie**  
College of Electronic Engineering,  
Ninevah University, Mosul, Iraq

# Introductory Chapter: Introduction to Array Pattern Optimization

*Khalil H. Sayidmarie and Jafar Ramadhan Mohammed*

Array antennas offer versatile and flexible solutions to the requirement for desired radiation patterns. The total field of the array can be controlled by five array parameters that are the main design parameters [1]. These are: the geometrical layout of the array elements and their spacings, the excitation amplitude and phase of the individual elements, and finally the pattern of the individual elements. These factors have been utilized by many array synthesis techniques that use either analytical or numerical approaches. These techniques have been extensively studied and are well documented [2, 3]. This chapter aims at presenting recent techniques that aim to improve and optimize the radiation pattern of array antennas.

While most of the array pattern synthesis approaches deal with all of the elements of the array antenna, the techniques presented in Chapter 2 offer easier solutions as only a limited number of the elements need to have their magnitudes and phases adjusted. Such approaches reduce the cost and complexity of the optimization process and achieve the desired radiation patterns by modifying the excitations of a small number of elements. Toward achieving this goal, earlier techniques that were based on simple analytical procedures have utilized only two or four elements at the side of the array to reduce the sidelobe level [4–9]. These simple analytical approaches have demonstrated the feasibility of the techniques in finding the proper excitations of the side elements. The same idea was developed to the case of planar arrays where much larger number of elements is used and much less number of controllable elements was required. Thus, it would be more economical if only the side elements are made controllable for the improvement of the array pattern [10]. The deployment of the side elements was also found applicable to improve the sum and difference patterns [11]. Some other effective methods based on either controlling the steer angle in a certain sub-array configuration or even sharing the element excitations at the tail of the array were also used to generate an improved sum and difference patterns in the tracking antenna arrays [12, 13]. The use of the side elements for obtaining a wide-angle null in the radiation pattern was presented in [14, 15]. Other approaches have utilized few elements at the center of the array to achieve better adaptive responses [16]. The side element idea was also deployed for the synthesis of asymmetrical radiation pattern where it is desirable to highly reduce the sidelobe on one side of the main beam while tolerating a higher sidelobes on the other side [17].

While simple analytical approaches give better insight into the mechanism of the antenna pattern improvement, global numerical optimization methods have been proved to give better performance and optimum results [18–20] than those analytical approaches. In order to show the superiority and the power of the global optimization methods that were presented in [18–20] among the analytical approaches that were

presented in [10, 15], the nonsymmetric array is considered as an example. For this case, the mathematical equation of the array factor with two variable parameters on each side of the array cannot be solved analytically using the method introduced in [15], since it is a function of four unknown parameters, that is, two different attenuators and two different phase shifters. However, this case can be efficiently solved, and optimal values of the unknown parameters in the array factor can be easily found using any global optimization algorithm such as genetic algorithm or particle swarm optimization (PSO) as it was shown in [18–20]. On the other hand, the analytical approaches [10, 15] were able to solve this case only under the assumption of symmetric array and by assuming a proper value of the required phase shifter and then find the value of unknown parameter of the required amplitude excitation. However, the symmetric array is not a general case especially in practice.

Most of the designs dealing with array antennas, as those described in Chapter 2, are concerned with the radiation pattern in the farfield region at a constant distance or equivalently across the surface of a sphere. In some applications, the designed array antenna is required to supply field or power density distribution of certain characteristics across a plane surface. This goal can be approached through one of the synthesis techniques. The problem of antenna array synthesis for radiation pattern defined on a planar surface is examined in Chapter 3. In this situation, the distance from the array to the planar surface cannot be assumed constant, and thus the  $1/r$  decay factor effect cannot be neglected. One example of such case is an antenna array that is mechanically tilted and a pattern defined in terms of Cartesian coordinates, as in the electronic toll collection (ETC) scenario [21]. In this application, the plane surface is parallel to and just above the ground, while the transmitting and receiving antennas are a few meters above the ground. Chapter 3 presents two possible approaches to this issue [22, 23]. The first one aims at the precise synthesis of the pattern in the case both a constant power bounded area and a sidelobe suppression region are defined and the required element excitations need to be found. In the second approach, the coverage area is stretched toward the travel length (without considering a precise definition of the communication area). This is to increase the available identification time with an iterative methodology. The chapter presents an antenna prototype which was fabricated and experimentally tested to confirm the validity of the approach [24].

An important approach to the design and optimization of array patterns is the beamforming techniques. Here, the array elements are fed through a network that furnishes the phases and magnitudes necessary to obtain the desired radiation pattern. Chapter 4 reviews the worldwide progress in the design of optical beamforming networks that are intended to the next-generation ultra-wideband millimeter-wave phased array antennas [25, 26]. Such approaches are prepared for the incoming 5G wireless systems, which in recent years are under investigation and development of worldwide communication community. Toward this goal, the chapter presents a detailed study for the design concepts below true-time delay photonics beamforming networks based on switchable or continuously tunable control. The NI AWRDE CAD-based simulation experiments are presented in the frequency range of 57–76 GHz on design of two 16-channel photonics beamforming networks using true time delay approach [27]. In the first scheme of the known configuration, each channel includes laser, optical modulator, and 5-bit binary switchable chain of optical delay lines. The second scheme has an optimized configuration based on only 3-bit binary switchable chain of optical delay lines in each channel, all of which are driven by four lasers with wavelength division multiplexing and a common optical modulator. In the result, the novel structurally and cost-efficient configuration of microwave-photonics beamforming network combining wavelength division multiplexing and true time delay techniques is proposed and investigated.



As the applications of the array antenna principles are developing, the number of the required antenna elements is rapidly increasing, as for the case of scanned radars and synthetic imaging radars. In compliance with the development of massive multiple-input multiple-output (MIMO) and beamforming techniques in 5G technology increased antenna elements became of further concern. The integrated antenna, which is composed of multiple antenna elements, will be considered for next generation technologies. Therefore, chapter 5 provides the mathematical and practical explanation of the integrated antenna for the next generation technologies. The integrated antenna array consists of multiple array elements, and the array element has multiple antenna elements. Each antenna element of the integrated antenna has different radiation patterns to increase the spectral efficiency in wireless communication area. This chapter first presents a mathematical expression of the antenna element based on the spherical vector wave modes [28], then the channel models for the integrated antenna, and the antenna array based on the integrated antenna are explained. Second, the chapter provides practical antennas designed based on the integrated antenna approach, and it is verified that the integrated antenna array can be implemented practically [29]. Last, the performance of the integrated antenna array compared to mono-polarization and dual-polarization dipole arrays is compared.


The most recent antenna array technologies such as smart antenna system (SAS) and massive multiple-input multiple-output (MIMO) system are giving a strong and increasing impact relative to 5G wireless communication systems. This is due to the benefits that are obtainable in terms of performance improvements with respect to omnidirectional antennas. A considerable number of theoretical proposals have been presented in this field [30, 31]. However, the most commonly used network simulators do not implement the latest wireless network standards. Consequently, most simulators do not offer the possibility to emulate scenarios in which SAS and massive MIMO system are employed. This aspect heavily affects the quality of the network performance analysis with regard to the next generation wireless communication systems. To overcome this issue, it is possible, for example, to extend the default features offered by one of the most used network simulators such as Omnet++ which provides a very complete suite of network protocols and patterns that can be adapted in order to support the latest antenna array systems. The main goal of Chapter 6 is to illustrate the improvements accomplished in this field, allowing to enhance the basic functionalities of the Omnet++ simulator by implementing the most modern antenna array technologies [32].

## Author details

Khalil H. Sayidmarie and Jafar Ramadhan Mohammed\*  
College of Electronic Engineering, Ninevah University, Mosul, Iraq

\*Address all correspondence to: [jafarram@yahoo.com](mailto:jafarram@yahoo.com)

## IntechOpen

© 2019 The Author(s). Licensee IntechOpen. This chapter is distributed under the terms of the Creative Commons Attribution License (<http://creativecommons.org/licenses/by/3.0>), which permits unrestricted use, distribution, and reproduction in any medium, provided the original work is properly cited. 

## References

- [1] Balanis CA. *Antenna Theory, Analysis and Design*. 4th ed. Hoboken, New Jersey: Wiley; 2016
- [2] Mailloux RJ. *Phased Array Antenna Handbook*. 2nd ed. Norwood, MA: Artech House; 2005
- [3] Haupt RL. *Antenna Arrays: A Computational Approach*. Hoboken, New Jersey: John Wiley & Sons; 2010
- [4] Mohammed JR. An investigation into side lobe reduction and cancellation techniques [M.Sc. thesis]. College of Engineering, Mosul University; 2001
- [5] Sayidmarie KH, Mohammed JR. A simple technique for side lobe reduction and cancellation. *Al-Rafiddin Engineering Journal*. 2002;**10**(1):53-62
- [6] Sayidmarie KH, Mohammed JR. Design of a linear array with asymmetric low side lobes. *Al-Rafiddin Engineering Journal*. 2004;**12**(1):1-9
- [7] Sayidmarie KH, Mohammed JR. A simple technique for sidelobe reduction and cancellation. *Al Rafiddin Engineering Journal*. 2002;**10**(1):53-62
- [8] About AH, Sayidmarie KH. Reduction of sidelobe structure in phased arrays by auxiliary antenna. In: *Asia-Pacific Radio Science Conference AP-RSC04*; 24-27 August 2004; Qingdao, China. 2004
- [9] About AH, Sayidmarie KH. Reduction of sidelobe structure in phased arrays by a 4-element auxiliary antenna. In: *3rd IEEE Int. Conf. On Systems, Signals & Devices*; Tunisia. 2005
- [10] Mohammed JR, Sayidmarie KH. Sidelobe cancellation for uniformly excited planar array antennas by controlling the side elements. *IEEE Antennas and Wireless Propagation Letters*. 2014;**13**:987-990
- [11] Mohammed JR, Sayidmarie KH. A new technique for obtaining wide-angular nulling in the sum and difference patterns of monopulse antenna. *IEEE Antennas and Wireless Propagation Letters*. 2012;**11**:1245-1248. And its correction on 26 March 2013
- [12] Mohammed JR. Synthesizing sum and difference patterns with low complexity feeding network by sharing element excitations. *International Journal of Antennas and Propagation*. 2017;**2017**:7. Article ID 2563901
- [13] Mohammed JR. Synthesizing uniform sum and difference patterns by controlling steer angle and using sub-arrays. *Global Journal of Research in Engineering*. 2017;**17**(7):33-41
- [14] Sayidmarie KH, Mohammed JR. Performance of a wide angle and wideband nulling method for phased arrays. *Progress in Electromagnetics Research*. 2013;**33**:239-249
- [15] Mohammed JR, Sayidmarie KH. Null steering method by controlling two elements. *IET Microwaves, Antennas and Propagation*. 2014;**8**(15):1348-1355
- [16] Mohammed JR, Sayidmarie KH. Performance evaluation of the adaptive sidelobe canceller system with various auxiliary configurations. *International Journal of Electronics and Communications*. 2017;**80**:179-185
- [17] Mohammed JR, Sayidmarie KH. Synthesizing asymmetric side lobe pattern with steered nulling in nonuniformly excited linear arrays by controlling edge elements. *International Journal of Antennas and Propagation*. 2017;**7**:1-7
- [18] Mohammed JR. Element selection for optimized multi-wide nulls in

almost uniformly excited arrays. *IEEE Antennas and Wireless Propagation Letters*. 2018;**17**(4):629-632

[19] Mohammed JR. Thinning a subset of selected elements for null steering using binary genetic algorithm. *Progress in Electromagnetics Research*. 2018;**67**:147-155

[20] Mohammed JR. Optimal null steering method in uniformly excited equally spaced linear arrays by optimising two edge elements. *Electronics Letters*. 2017;**53**(13):835-837

[21] Inserra D, Wen G. Communication area synthesis for next generation highway ETC systems. In: *Proceeding of IEEE International Conference on Communications in China (ICCC'16)*; 27-29 July 2016; Chengdu, China. 2016. pp. 1-6

[22] Inserra D, Wen G, Hu W. Linear optimization of antenna array for radiation pattern defined on a planar surface. *Journal of Electromagnetic Waves and Applications*. 2018;**32**(16):2030-2045

[23] Inserra D, Hu W, Wen G. Antenna array synthesis for RFID-based electronic toll collection. *IEEE Transactions on Antennas and Propagation*. 2018;**66**(9):4596-4605

[24] Inserra D, Hu W, Wen G. Design of a microstrip series power divider for sequentially rotated nonuniform antenna array. *International Journal of Antennas and Propagation*. 2017;**8**:1-8

[25] Seeds AJ, Williams KJ. Microwave photonics. *IEEE/OSA Journal of Lightwave Technology*. 2006;**24**(12):4628-4641

[26] Belkin ME, Golovin V, Tyschuk Y, Sigov AS. Comparison of RF photonics-based beamformers for super-wide bandwidth phased array antennas. *IOP*

*Conference Series: Materials Science and Engineering*. 2017;**198**:1-4

[27] Belkin ME, Golovin V, Tyschuk Y, Sigov AS. A simulation technique for designing next-generation information and communication systems based on off-the-shelf microwave electronics computer tool. *International Journal of Simulation and Process Modelling*. 2018;**13**(3):238-254

[28] Glazunov AA. A survey of the application of the spherical vector wave mode expansion approach to antenna-channel interaction modeling. *Radio Science*. 2014;**49**(8):663-679

[29] Park D, Cho DH. Analysis of pattern gain of compact directional 16-port antenna. *IEEE Antennas and Wireless Propagation Letters*. 2015;**14**:902-905

[30] Lu L, Li G, et al. An overview of massive MIMO: Benefits and challenges. *IEEE Journal of Selected Topics in Signal Processing*. 2014;**8**(5):742-758

[31] Molisch AF, Ratnam V, Han S, et al. Hybrid beamforming for massive MIMO: A survey. *IEEE Communications Magazine*. 2017;**55**(9):134-141

[32] Inzillo V, De Rango F, Santamaria AF, Ariza AQ. A new switched beam smart antenna model for supporting asymmetrical communications extending Inet omnet++ framework. In: *Proceedings of International Symposium on Performance Evaluation of Computer and Telecommunication Systems (SPECTS)*. 2017. pp. 1-7



# Sidelobe Nulling by Optimizing Selected Elements in the Linear and Planar Arrays

*Jafar Ramadhan Mohammed and Khalil H. Sayidmarie*

## Abstract

Currently, there are significant interests in the antenna arrays that are composed of a large number of elements controlled by an appropriate optimizer for the next generation of wireless communication systems, where the massive multiple-inputs multiple-outputs (MIMO) systems are expected to play a major role in such systems. On the other hand, the interfering signals which are expected to rise dramatically in these applications due to the crowded spectrum represent a real challenging issue that limits and causes great degradation in their performances. To achieve an optimum performance, these antenna arrays should be optimized and designed to have maximum gain, narrow beam width, and very low sidelobes or deep nulls. Toward achieving this goal, the overall array performance can be either electronically controlling the design parameters, such as amplitude and/or phase excitations of the individual elements, or mechanically controlling the element positions. This chapter discusses techniques proposed for sidelobe nulling by optimizing the excitations and positions of selected elements in the linear and planar arrays.

**Keywords:** antenna arrays, array pattern synthesis, null steering, sidelobe reduction, optimization algorithms

## 1. Introduction

Antenna arrays can be designed to reconfigure their radiation characteristics either by electronically controlling the amplitude and/or phase excitations of the array elements or by mechanically controlling the separation distances between the array elements. Accordingly, the null steering methods are generally divided into two main categories: electronic null steering and mechanical null steering. Each of them has its own advantages and disadvantages as will be shown in the following sections.

Generally, large antenna arrays are characterized by very high gains and narrow main beams. Thus, they are widely used in many applications including satellites, radio telescopes, communication systems, radar, sonar, and many other systems including future fifth generation (5G) wireless communication systems. The performances of these systems may degrade severely under the presence of interfering signals and/or ground clutter, which are unavoidable in such applications. Therefore, it is highly desirable to suppress, or at least reduce, the sidelobes into which the interfering signals are coming. This means that the shape of the radiation

pattern of such antenna arrays can be reconfigured to have maximum directive gain in the direction of its main beam and low sidelobes or deep nulls toward other unwanted directions.

In the literature, several strategies have been described to reshape the array radiation pattern. Among them, electronic phased arrays or more specifically beam forming has received considerable attention [1–3]. However, most of the adaptive algorithms that were used in such type of antennas are time-consuming because they involve a large number of iterations and they are not able to provide global optimum solutions. Reconfiguration of the array pattern with prescribed sidelobe structure mask can be also achieved by means of the global optimization approaches. The proposed approaches were genetic algorithm [4, 5], particle swarm optimization [6, 7], simulated annealing [8, 9], ant colony optimization [10], differential evolution algorithm [11], firefly algorithm [12], and some other methods [13], where the amplitude and/or phase of the elements excitations are the optimization parameters.

Apart from the aforementioned approaches, new directions in antenna array pattern reconfiguration have been proposed based on either adding a small number of extra elements on each side of the linear array [14–16], or by reusing the side (or end) elements of the linear arrays [17] or planar arrays [18, 19]. In these papers, the calculations that were required to find the values of the amplitude and phase excitations of the side elements basically relied on simple mathematical formulations and none of the optimization algorithms were used. Thus, the solutions were not optimum and there was a necessary need to search for an optimum solution for such an important scenario. Therefore, instead of a simple analytical method that was presented in [17], a more powerful method based on the genetic algorithm was proposed to find the optimal values of the amplitude and phase excitations for those electronically controllable edge elements with less computational time [20]. The method presented in [20] is further extended to obtain multiple wide nulls by properly selecting and optimizing the most effective elements in the array [21]. Wide nulls were also obtained by turning off some selected elements in the uniformly spaced linear arrays by means of binary genetic algorithm [22]. In all of those previous works, the null steering was performed electronically by controlling the amplitude and phase excitations of the array elements.

On the other hand, the mechanical null steering methods that are based on the controlling of the separation distance between the array elements were considered as an alternative and competitive solution to the electronic counterpart [23–25]. In [26], the author proved that the mechanical null steering made better patterns when compared with the electronic counterpart [20], by mechanically controlling the positions of the extreme elements while leaving all the electronic excitations including the edge elements constant.

The chapter is organized as follows: Section 2 provides a theoretical overview about electronic null steering including fully and partially controlled array elements. It also contains the sensitivity analysis of the generated nulls as well as how much the nulling is robust with respect to variations in the reconfigured amplitude and phase excitations. Section 3 provides a theoretical overview of a mechanical null steering including fully nonuniform spaced arrays and the proposed solution. It also explains the implementation strategies of the aforementioned technologies.

## **2. Electronic null steering methods**

This technique involves the modification of amplitude and/or phase excitations of an  $N$ -element array. The amplitude and/or phase excitations of these array

elements should be specifically selected through an appropriate control system that is connected to each of the array elements. Clearly, for such electronic null steering strategy and for  $N$  elements linear array, we need  $N$  variable attenuators and  $N$  variable phase shifters for the feeding network. This results in a very complex feeding network especially for a large number of elements which, of course, becomes expensive and may be impractical. Therefore, a less costly and simpler system for reducing the effect of interfering signals is needed. In this section, a simple technique for sidelobe nulling over a wide angular region in the linear arrays is introduced, where only the electronic excitations of the two side elements of the array were needed to be controllable while maintaining the same performance of interference suppression. Thus, the feeding network of the proposed linear array contains, in most designs, only two phase shifters and one attenuator.

## 2.1 Linear array

Consider a linear array of  $N$  isotropic elements which are mechanically fixed by selecting the separation distance between the array elements to be uniform at a constant value  $d$ . These elements are symmetrically disposed with respect to the origin along the  $x$ -axis and suppose that a harmonic plane wave with wavelength  $\lambda$  is incident from direction  $\theta$  and propagates across the array. The  $I$  signal outputs from the array elements are weighted by the amplitude excitation coefficients  $A_n$  and phase excitation coefficients  $P_n$  then summed to give the linear array output. The sidelobe nulling was achieved by properly adjusting the values of the attenuators and phase shifters that are connected to each element.

### 2.1.1 Single null

This subsection presents an efficient method for controlling the amplitude and phase excitations of the end elements by means of global optimization algorithms such as genetic algorithm or particle swarm optimization to generate a sector sidelobe nulling in the linear arrays without any reduction in the array gain [20]. To maintain the gain of the designed array and also to increase the convergence rate of the used optimization algorithms, some constraints on the searching spaces are included.

### 2.1.2 The electronic single null steering method

The structure of the electronically null steering array, with controlled amplitudes  $A_1$  and  $A_N$  as well as controlled phases  $P_1$  and  $P_N$  for the first and the last elements in a linear array is shown in **Figure 1** [20]. The amplitudes and phases of the edge-element excitations can be considered as either symmetric or asymmetric excitation. Note that the proposed array under the asymmetric excitation will have 4 degrees of freedom, while for the symmetric case it will have only 2 degrees of freedom. These numbers are also true when considering the optimization parameters. The far-field pattern of the electronically null steering array with controlled amplitude and phase excitations, assuming even number of elements, can be written as [20]:

$$AF(u) = \underbrace{\sum_{n=2}^{N/2} \cos\left(n - \frac{1}{2}\right)\psi}_{N-2 \text{ uniform array}} + \underbrace{A_1 e^{j\left(\frac{N-1}{2}\right)\psi + P_1} + A_N e^{-j\left(\frac{N-1}{2}\right)\psi + P_N}}_{\text{Edge elements alone}} \quad (1)$$

where  $\psi = (2\pi d/\lambda)u + \beta$ . Here,  $u = \sin(\theta)$ , and  $\theta$  is the observation angle from the array normal,  $d$  is the element spacing which is selected to be fixed at  $d = \lambda/2$  for all array elements, and  $\beta$  is the phase shift required to steer the angle of the main beam. Knowing the direction of the interfering signals,  $u_i$ ,  $i = 1, 2, \dots, I$  (where  $I$  is the total number of interfering signals), and substituting for  $AF(u_i) = 0$  according to the interference suppression condition, the nulls directions  $u_i$  can be computed from (1).

For asymmetric array, note that the above equation cannot be solved analytically using the method introduced in [17] since it is a function of four unknown parameters, i.e.,  $A_1$ ,  $A_N$ ,  $P_1$ , and  $P_N$ . On the other hand, the optimal values of these four parameters, subject to some constraints, can be easily found using any global optimization algorithm such as genetic algorithm or particle swarm optimization (PSO), as can be seen in the following subsection [20]. As mentioned earlier, the main constraints that are applied during the optimization process are the depth of the generated nulls and the main beam shape preservation. Moreover, some constraints on the optimization parameters are also considered, where the minimum and maximum values of the optimized amplitudes  $A_1$  and  $A_N$  are set to 0 and 1, respectively, and for optimized phases  $P_1$  and  $P_N$  are set to  $-\pi/2$  and  $\pi/2$ , respectively [20]. To show the effectiveness of the proposed method, it is applied to uniformly excited linear arrays as well as some nonuniformly excited linear arrays such as Dolph and Taylor arrays as can be seen in the following subsection [20].

### 2.1.3 The results

In order to show the advantages of the proposed array with controlled two edge elements, first the fully controlled array (i.e., the amplitude excitation of all array

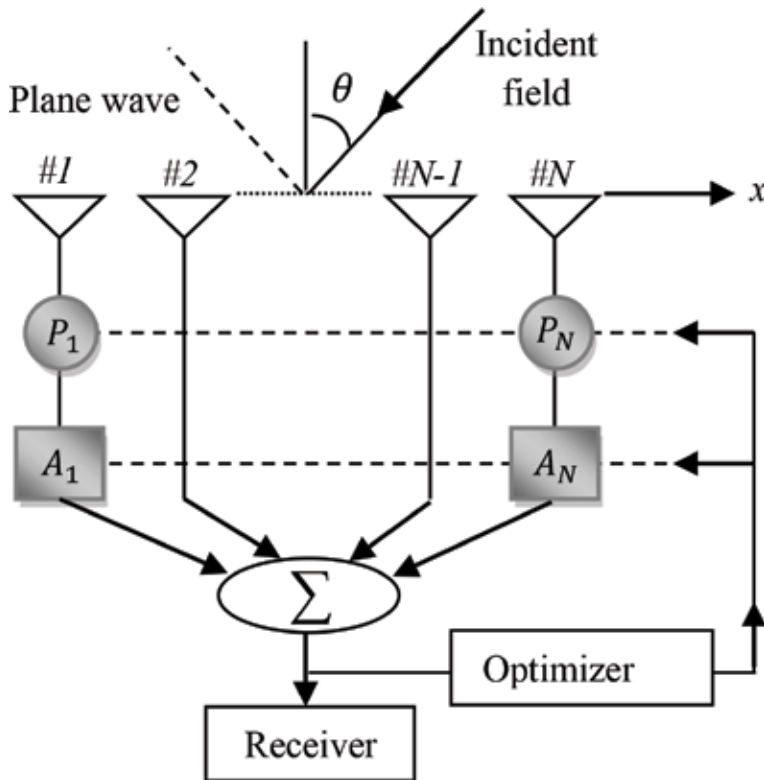


**Figure 1.** Block diagram of the single wide null method [20].



elements are controlled including the two edge elements) is considered. In this example, the total number of array elements are chosen to be  $N = 30$  elements, the amplitude excitation of the original array elements is chosen to be uniform and the phase excitation is set to zero. In this scenario, the genetic algorithm is used to optimize the amplitude excitations of all array elements while the phase excitations are left unchanged. The required sidelobe level was set at  $-40$  dB. **Figure 2** shows the optimized array pattern along with the original uniform array pattern. It can be seen that the required sidelobe level is accurately achieved while the HPBW and FNBW have increased. The amplitude excitations of all array elements are greatly changed except a small number of the central elements. Moreover, the optimizer needs at least 250 iterations to converge.

For a fully controlled array, the number of degrees of freedom is quite enough to reduce the sidelobe level and at the same time to place the desired nulls, as shown in **Figure 3**. Here, as in the previous case, the required sidelobe level is chosen to be

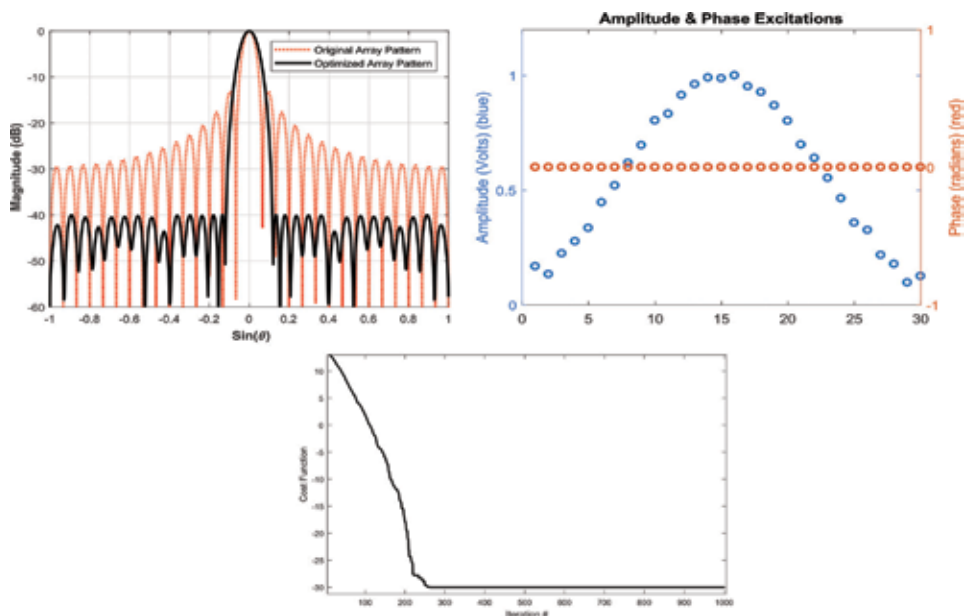


**Figure 2.**  
 Results for fully electronic null steering method for  $N = 30$  and  $SLL = -40$  dB.

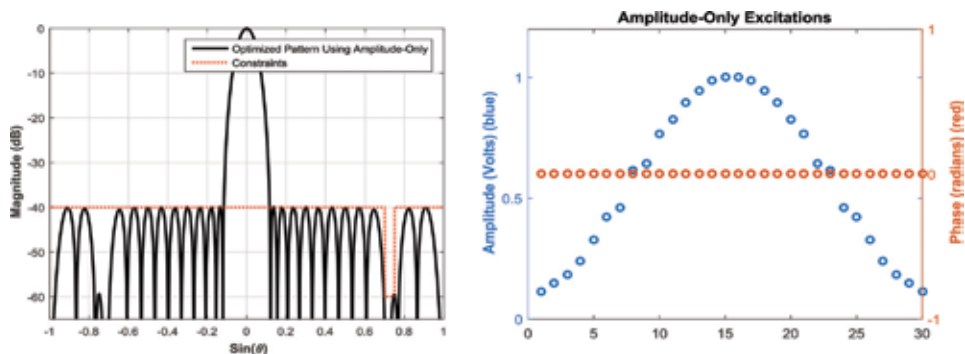


**Figure 3.**  
 Results for fully electronic null steering method with amplitude only control for  $N = 30$ ,  $SLL = -40$  dB, and a single wide null.

−40 dB and a single wide null centered at  $u = 0.75$  (ranged from  $u = 0.73$  to  $0.77$ ) is considered. Similar results are obtained when the amplitude and the phase excitations of the full elements are optimized are shown in **Figure 4**.

All of the above results show clearly that the required shape of the array pattern can be obtained only when precisely choosing the values of the attenuators. In practice, the attenuators are digital and they have a limited number of quantized levels. Thus, these required shapes are far or even impossible to get. Therefore, the arrays that are composed of a few controllable elements are very desirable in practice. In the next example, we consider an array of  $N = 100$  elements and only the edge element are optimized by either the GA or PSO algorithm. Here, only a single wide null is required to be placed from  $u = 0.4$  to  $0.5$  with depth −60 dB. Moreover, the original excitations of all array elements are assumed to be uniform. **Figure 5** shows the radiation patterns of the optimized arrays using GA and PSO along with the original uniform array pattern. This figure also shows the convergence rate of the optimizer under these two different algorithms.

It can be seen that the optimized arrays by GA and PSO are equally capable of achieving the required wide sidelobe nulling. The HPBW of the original uniform array, and the optimized array are  $1.0084$  and  $1.0314^\circ$ , respectively. For this case, the optimized values of  $A_1$ ,  $A_N$ ,  $P_1$ , and  $P_N$  using GA were found to be  $0.8181$ ,  $0.7313$ ,  $52.2824$  and  $-47.6185^\circ$ , respectively; whereas, these value were found to be  $0.7322$ ,  $0.8179$ ,  $47.7388$  and  $-52.4027^\circ$  for PSO design. The computational times for GA and PSO were found to be  $0.15429$  and  $0.12667$  min, respectively.

In **Figure 6**, the results of the proposed single null steering method is examined for  $N = 30$  elements and the desired null is from  $u = 0.7$  to  $0.75$  with a depth equal to −60 dB. This figure also shows the required amplitudes and phases of both the original and optimized arrays.

By comparing the results of **Figure 6** with those of **Figure 3** or **Figure 4**, it can be clearly seen that the proposed single null steering method requires only one attenuator and two phase shifters to realize the modified element excitations. However, the fully controlled array requires at least 30 attenuators and 30 phase shifters to realize the reconfigured amplitude and phase weights. This fully confirms the effectiveness of the proposed single null steering method.

Moreover, to show the generality of the proposed method, we extend it to the nonuniformly excited arrays such as Dolph and Taylor arrays. **Figures 7** and **8** show the radiation patterns of the Dolph and Taylor arrays ( $N = 30$  elements, and  $SLL = -40$  dB), where the excitations of the edge elements are optimized using GA for the purpose of generating sector sidelobe nulling with same width and depth as in the previous example.

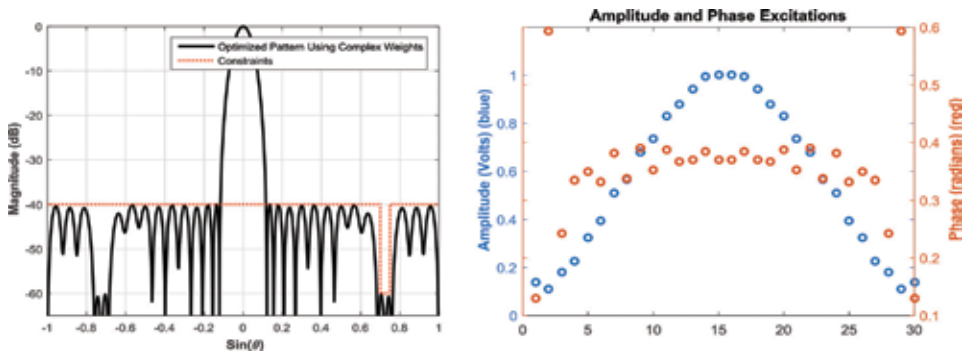


**Figure 4.** The results for fully electronic null steering method with amplitude and phase excitations for  $N = 30$ ,  $SLL = -40$  dB, and a single wide null.

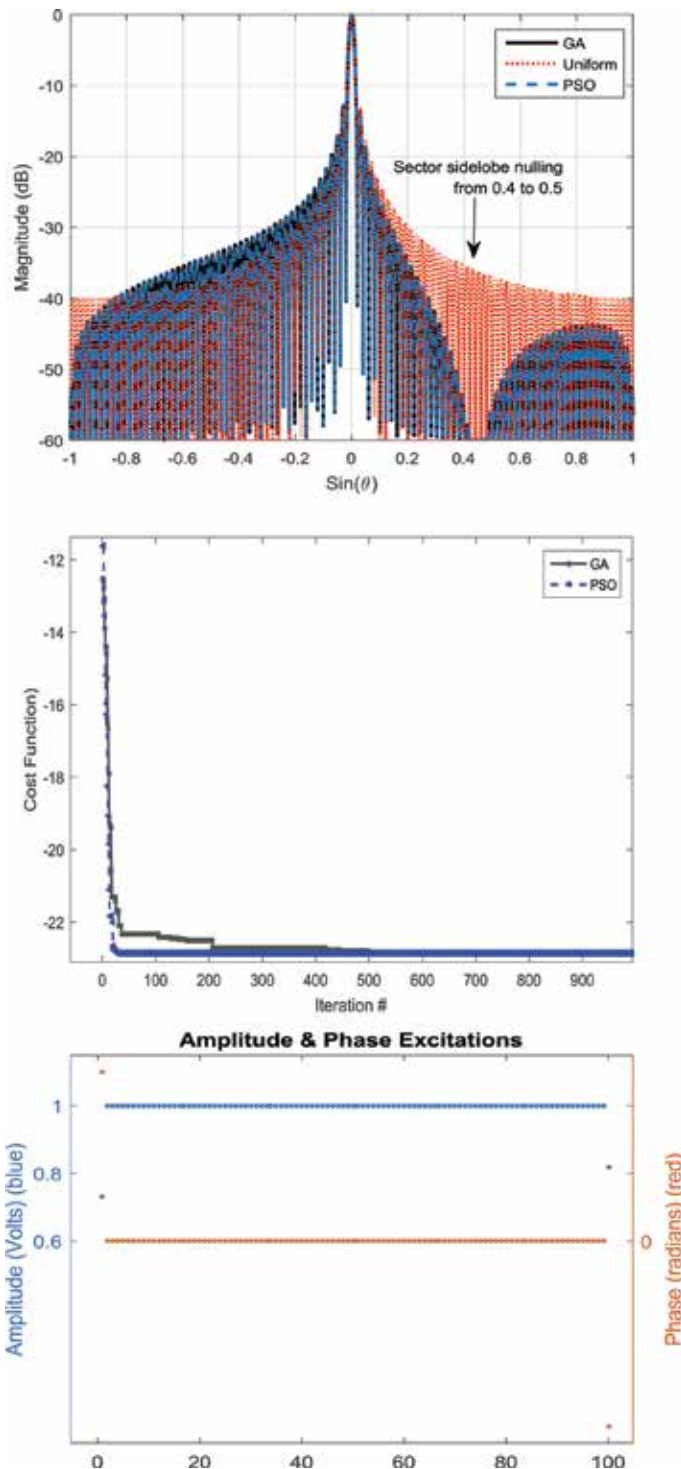


**Figure 5.**  
The results for the proposed single null steering method for  $N = 100$ .

#### 2.1.4 Multiple nulls

As we have shown in the previous subsection that a single wide null requires at least controlling the excitations of the two end elements in a linear array. In many

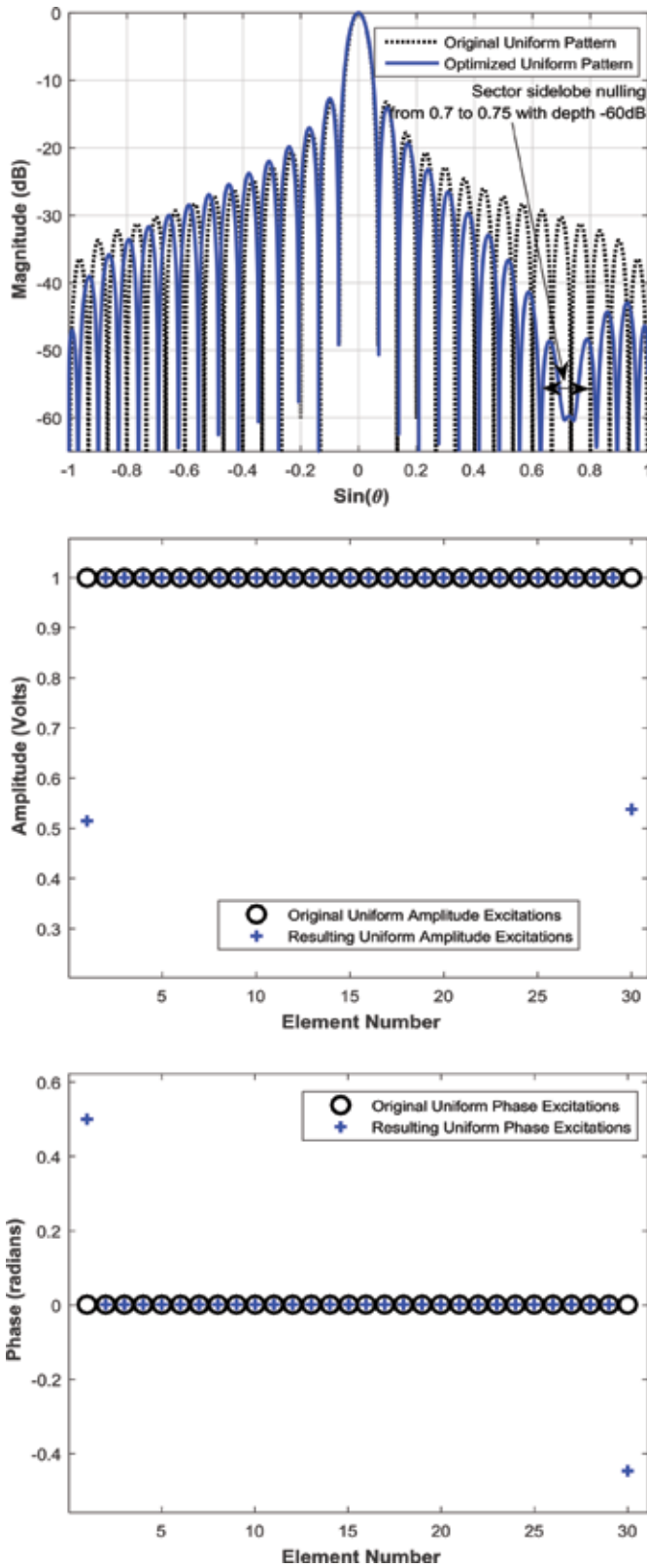
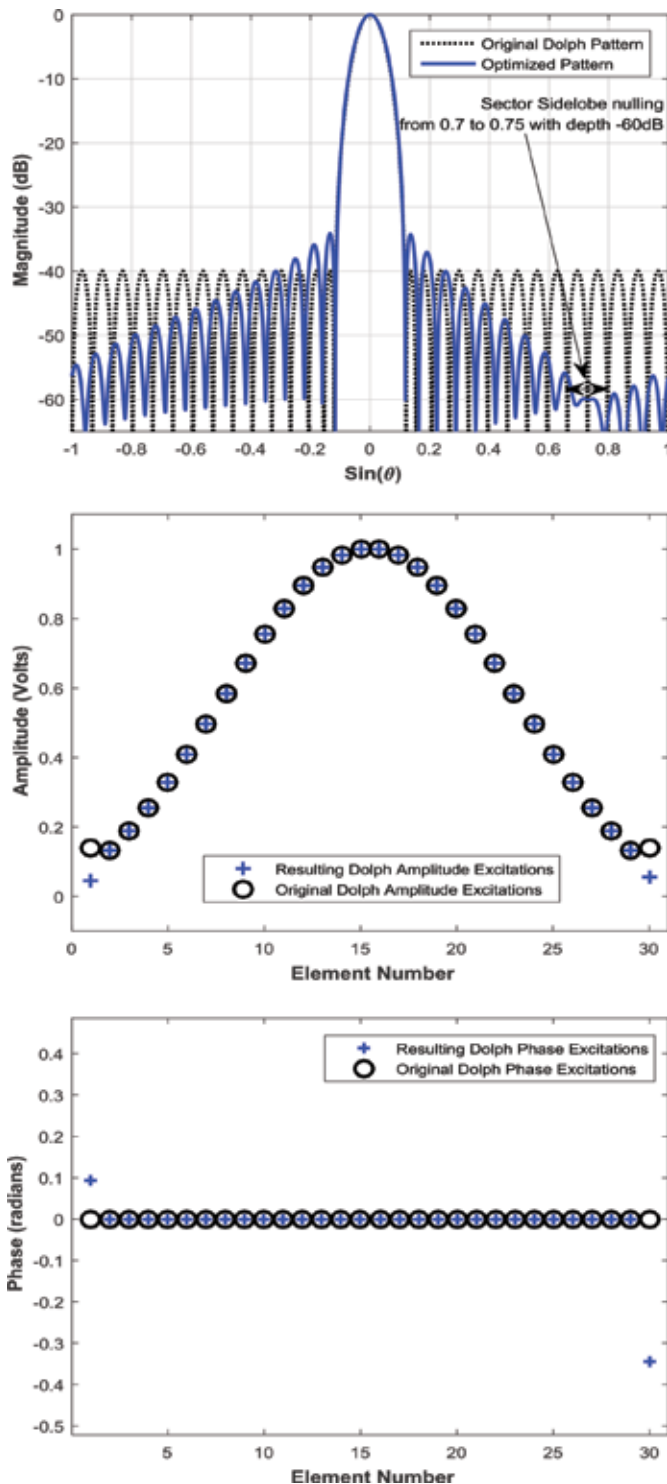
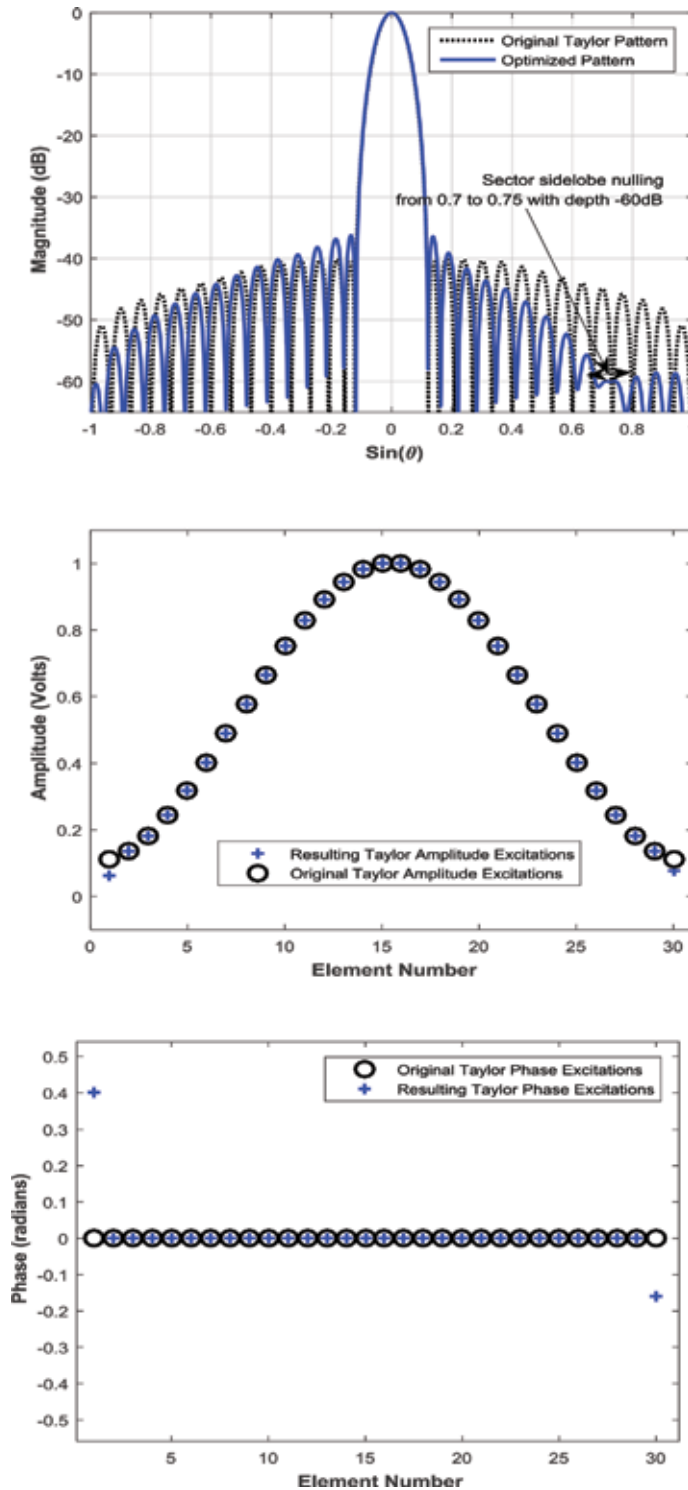


Figure 6. The results for the proposed single null steering method for  $N = 30$ .



**Figure 7.**  
 Results for the proposed single null steering method for  $N = 30$  and Dolph excitation.

applications with multi interference environment, it is desirable to generate multiple wide nulls in the radiation pattern; thus, a set of element excitations have to be modified. In this subsection, a subset of a small number of adjustable elements on



**Figure 8.** Results for the proposed single null steering method for  $N = 30$  and Taylor excitation.

both sides of the array is considered. Therefore, the far-field equation of the overall array is formulated as the summation of two independent array subsets. The first array subset is referred to as a uniform array, which contains the majority of the

array elements; whereas, the second array subset contains only a small number of the array elements that will be adjusted adaptively. The GA is used to optimize the amplitude and phase excitations of the second array subset elements [21].

#### 2.1.4.1 The electronic multiple null steering method

Here in this subsection, the solution proposed in Section 2.1.2 is further extended to include which elements are to be optimized and to what extent. The small number of the selected elements should have an impact on the controllable nulls. Therefore, we examine three different selection strategies. The first strategy selects the most effective elements that are located on the extremes of the array; while in the second and third strategies, the selections consider the elements that are located at the center of the array or randomly chosen from the whole array elements [21]. The idea of the second strategy was employed in a sidelobe adaptive canceller system [27]. By adapting few elements at the center of the array, the system is capable to produce multiple nulls toward a number of interfering signals [27]. Experience with these three selection strategies showed that the first strategy provides best performance for interference suppression [21]. To apply the first strategy, first, consider an array of an even number of elements  $2N$ , with uniform amplitude excitations and mechanically fixed locations with uniform inter-element spacing  $d$ , symmetrically positioned about the origin (i.e.,  $N$  elements are placed on each side of the origin). Assuming a subset of only  $2M$  elements (out of the  $2N$ -element array) is optimized to generate the required nulls at unwanted directions (i.e.,  $M$  outer elements on each end of the array). The remaining  $2N-2M$  elements are kept unchanged, i.e., having uniform amplitude and equal-phase excitations. The overall far-field pattern due to the  $2N-2M$  uniformly excited array elements and the  $2M$  adaptive array elements can be written as [21]:

$$AF(u) = 2 \underbrace{\sum_{n=1}^{(N-M)} \cos \left[ \frac{(2n-1)kdu}{2} \right]}_{2N-2M \text{ uniform array}} + \underbrace{\sum_{m=N-M+1}^N \left\{ A_{m_r} e^{j\left(\frac{2m-1}{2}kdu+P_{m_r}\right)} + A_{m_l} e^{-j\left(\frac{2m-1}{2}kdu+P_{m_l}\right)} \right\}}_{2M \text{ elements array}} \quad (2)$$

where  $k = 2\pi/\lambda$ . From (2), it can be noted that the amplitudes ( $A_{m_r}$  and  $A_{m_l}$  for right and left subset elements) and phases ( $P_{m_r}$  and  $P_{m_l}$  for right and left subset elements) of  $2M$  adjustable elements array can be considered either symmetric or nonsymmetric (i.e.,  $A_{m_l} \neq A_{m_r}$  and  $P_{m_l} \neq P_{m_r}$ ) like the earlier method. Also note that the  $2M$  adjustable elements are selected from the extremes of the array and they play an important role in generating the required nulls. The structure of the interior  $2N-2M$  uniformly excited array elements with adjustable amplitude and phase excitations of the outer  $M$  elements on each side of the array is shown in **Figure 9** [21].

#### 2.1.4.2 The results

An original uniform linear array with  $2N = 100$  elements located at fixed positions and having element separation equals to half the wavelength is considered. **Figure 10** shows the results obtained from the original uniform array and the optimized array patterns with four required wide nulls each of width  $u = 0.05$  and depth =  $-60$  dB. Five elements at each side of the linear array are used here as the elements to be controlled. To show the effectiveness of the proposed array with respect to the fully optimized array, the radiation pattern of the fully phase-only optimized array and its convergence speed are also included in **Figure 10**. It can be

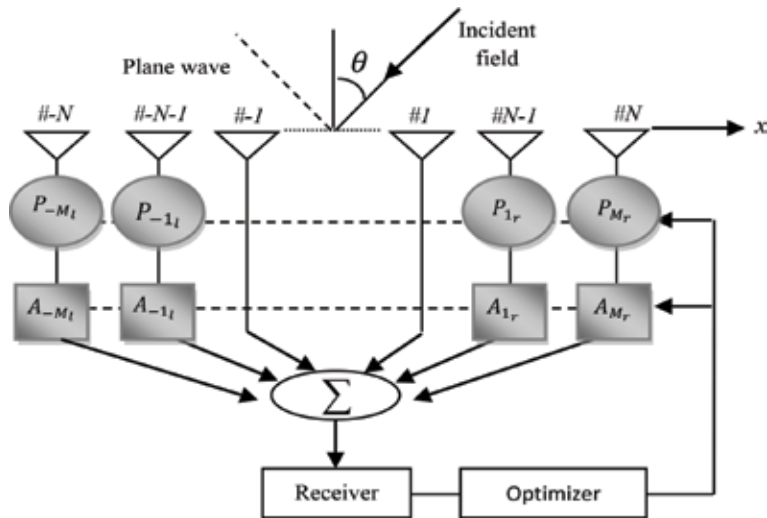


**Figure 9.** Configuration of the multiple null steering method [21].

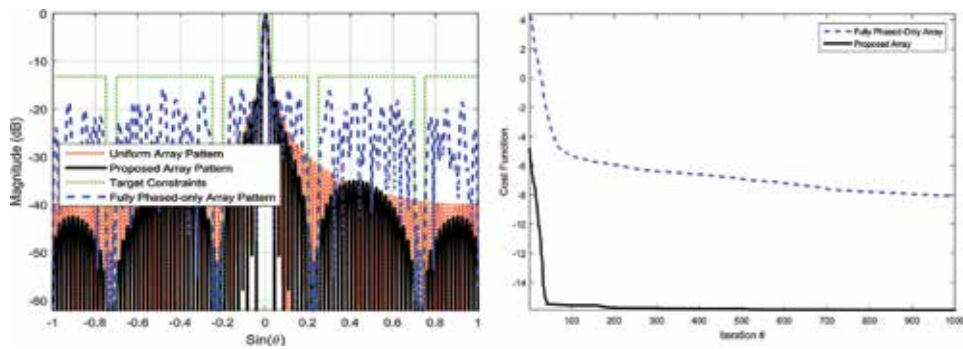


**Figure 10.** Results of multiple wide null steering method.

seen that the proposed array with only 10 adjustable outer elements is capable of generating the required multi nulls at pre-specified depths and widths. The same performance is obtained with the fully phase-only optimized array but with an extra requirement of modifying the phases of 100 elements (i.e., more cost and more optimization parameters). The half power beam width of the fully uniform and the proposed arrays are  $1.0085^\circ$  and  $1.0772^\circ$ , respectively. Moreover, the proposed method converges much faster than the method of fully phased-only optimized array. The amplitude and phase excitations of the proposed and the fully phased-only optimized arrays are shown in **Figure 11**. From this figure, it can be seen that the required percentage of the perturbed element excitation represents only 10% of those needed for the fully phased-only optimized array. This drastically reduces the RF components of the feeding network and consequently the cost while maintaining the same performance of interference suppression.

## 2.2 Planar array

In this section, the selection process of the controllable elements is extended to the large planar arrays to reach the desired radiation pattern with a minimum



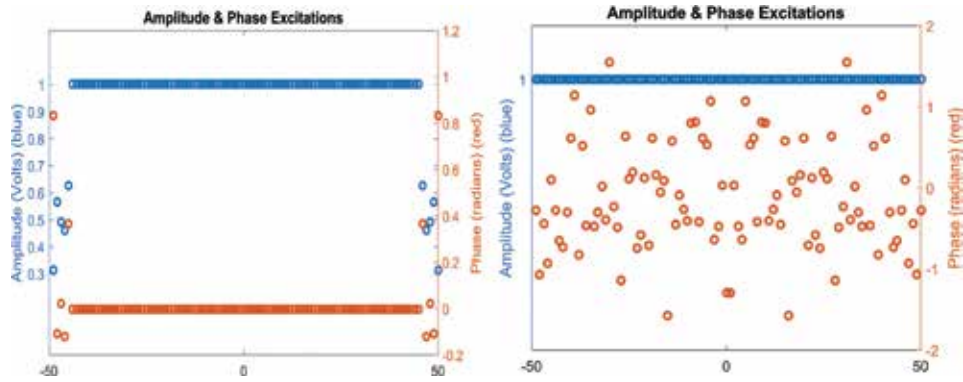


**Figure 11.**  
 Amplitude and phase excitations of the proposed array and fully phase-only array.

number of adjustable elements, where the searching spaces are restricted to include only the elements on the array's perimeter [28]. The optimization was performed under some constraints to obtain the desired radiation characteristics such as narrower beamwidth, asymmetric low sidelobes, and controlled nulls in some pre-specified directions. Unlike the existing methods, in which all the array elements are changeable, the proposed planar array enjoys a faster convergence of the optimizer as its interior elements are fixed and the whole array keeps maintaining a good performance [28].

### 2.2.1 The electronic planar null steering method

Consider a rectangular planar array composed of  $N$  rows and  $M$  columns of isotropic elements with mechanically fixed inter-element spacing  $d = \lambda/2$  in both  $x$  and  $y$  directions. The radiation pattern of such rectangular planar array can be written as [28]

$$AF(\theta, \phi) = \sum_{n=1}^N \sum_{m=1}^M w_{nm} e^{j\frac{2\pi d}{\lambda} [(n-\frac{N+1}{2})(\sin(\theta)\cos(\phi)-\beta_x) + (m-\frac{M+1}{2})(\sin(\theta)\sin(\phi)-\beta_y)]} \quad (3)$$

where  $\theta$  is the elevation angle,  $\phi$  is the azimuth angle, and  $\beta_x = \sin(\theta_0)\cos(\phi_0)$ ,  $\beta_y = \sin(\theta_0)\sin(\phi_0)$  are progressive phase shifts in  $x$  and  $y$  directions that are necessary to direct the mainbeam to the angle  $(\theta_0, \phi_0)$ , and  $w_{nm}$  is the complex weight of the  $(n, m)$ th element. Clearly, the array factor in (3) represents a fully controllable planar array in which all of its elements are adjustable and the resulting feeding network is a relatively complex system. Furthermore, to meet the required radiation characteristics, it is necessary to impose some constraints on the array weights which lead to an added complexity to the adaptive system. Thus, the necessity of controlling a small number of array elements arises especially with the practical implementation of large planar arrays or when faster adaptation is desirable.

In this work, the weights of the interior elements of the array (i.e., the central part having dimensions  $(N-2) \times (M-2)$ ) are assumed to be constant, i.e.,  $w_{nm} = 1$ , while the elements on the perimeter are only considered to be adjustable (or controllable) subject to some required constraints. Thus, the array factor of (3) can be rewritten as [28]

$$\begin{aligned}
 AF(\theta, \phi) = & \underbrace{\sum_{n=2}^{N-1} \sum_{m=2}^{M-1} e^{j\frac{2\pi d}{\lambda} \left[ \left( n - \frac{N+1}{2} \right) (\sin(\theta) \cos(\phi) - \beta_x) + \left( m - \frac{M+1}{2} \right) (\sin(\theta) \sin(\phi) - \beta_y) \right]}}_{\text{interiorelements}} \\
 & + \underbrace{\sum_{m=1}^M (w_{1m}\{\cdot\} + w_{Nm}\{\cdot\}) + \sum_{n=2}^{N-1} (w_{n1}\{\cdot\} + w_{nM}\{\cdot\})}_{\text{Perimetelements}}
 \end{aligned} \tag{4}$$

where  $\{\cdot\}$  represents the exponential term as expressed in the first term of Eq. (3). The perimeter elements in the lower term of (4) are expressed as the sum of 2 rows and 2 columns. In the two rows, the value of  $n$  is set to  $n = 1$  and  $n = N$ , while the value of  $m$  is allowed to change from 1 to  $M$ . In the two columns, the value of  $m$  is set to  $m = 1$  and  $m = M$ , while the value of  $n$  is allowed to change from 2 to  $M-1$  [28].

### 2.2.2 The results

In this subsection, a uniform planar array with  $N = 6$  and  $M = 6$  isotropic elements spaced by half a wavelength is considered. The required half power beamwidth (HPBW) of the proposed planar array pattern is chosen to be  $17^\circ$ , i.e.,  $\Omega_{BW} = 8.5^\circ$ . Note that, for a uniformly excited planar array with size  $6 \times 6$  elements the HPBW is also  $17^\circ$ . This means that the HPBW of the optimized array is constrained to be the same as that of the uniformly excited planar array.

Assume the direction of the desired signal is known, which is set to be  $90^\circ$ . The weights of the perimeter elements in the proposed planar array are optimized such that the corresponding radiation pattern has equal sidelobe level at  $-20$  dB and two nulls at  $\phi = -30^\circ, \theta = 80^\circ$  (i.e.,  $u_x = 0.852, u_y = -0.492$ ) and  $\phi = 45^\circ, \theta = -70^\circ$  (i.e.,  $u_x = -0.664, u_y = -0.664$ ). **Figure 12** shows the radiation patterns of the original uniform planar array and the proposed array. It can be seen that the required sidelobe level and the desired null are efficiently accomplished by optimizing only the perimeter elements.

The corresponding complex weights (i.e., the magnitudes and the phases) of all elements in the proposed planar array are shown in **Figure 13**. It can be seen that only the magnitudes and the phases of the 20 perimeter elements are adjusted, whereas the 16 interior elements remain holding their uniform excitations.

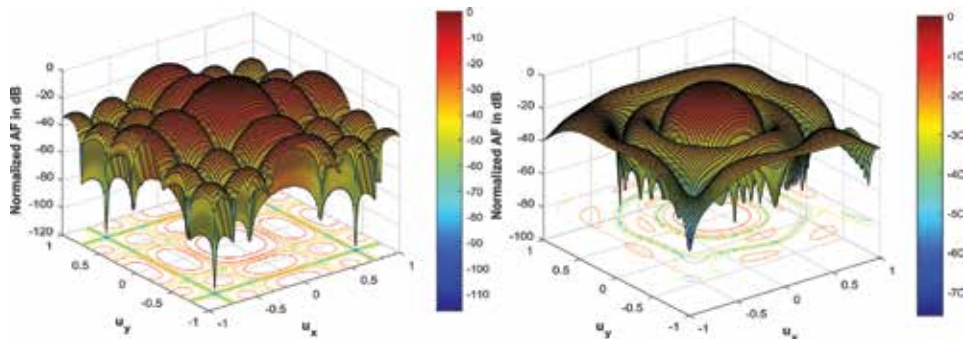


**Figure 12.** Optimized radiation pattern of the proposed planar array (right) and the uniformly excited planar array (left).

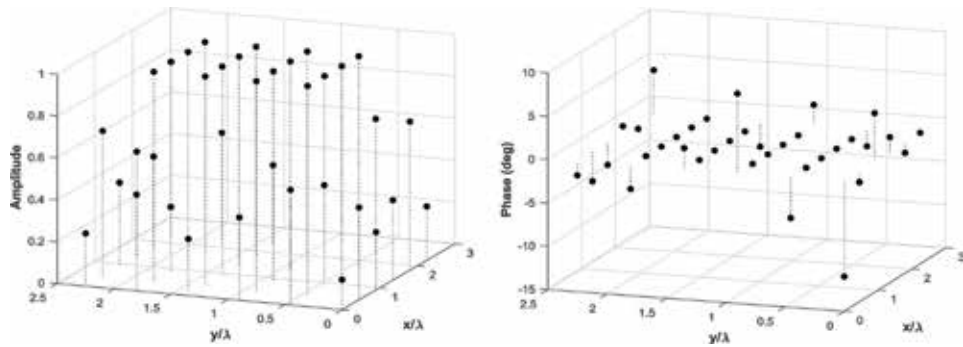


**Figure 13.**  
*Amplitude and phase excitations of the proposed planar array pattern that is shown in Figure 12.*

### 2.3 The sensitivity analysis

In this section, a realistic situation is investigated where the required element excitations in amplitude and phase cannot be realized exactly in practice, or when there is some fluctuation in the frequency of operation. The performance of the proposed optimization techniques and the null positions are investigated when there are some errors in the excitation of the array elements.

#### 2.3.1 The effect of quantization levels on the generated nulls

In this section, the sensitivity analysis is concerned with how much the generated nulls are robust with respect to unavoidable variations of the reconfigured amplitude and phase weights due to the quantization errors that are associated with the used digital attenuators and/or digital phase shifters. The electronic null steering methods including the above-mentioned methods require phase shifters and attenuators that are digitally controlled. With such digital components, it is well-known that only a finite number of quantized values are available. For example, a one-bit digital phase shifter produces only two phase values of 0 and  $\pi$ , while a two-bit digital shifter can realize four phases of 0,  $\pi/2$ ,  $\pi$ , and  $3\pi/2$ . Accordingly, with the use of discrete phase shifters and/or discrete attenuators, precise control over both amplitudes and phases of the adjustable elements is not possible. Therefore, unavoidable quantization error in the phase and/or amplitude excitations causes some modifications of the radiation pattern from the desired one. However, such performance degradations may be lesser in the proposed approaches than that in the fully optimized array elements where the number of the adjustable elements is small. **Figure 14** shows the sensitivity of the proposed multiple null steering method to various phase quantization levels. The effect is obvious on the sidelobe level and null depths.

The degradation in the optimized array pattern due to random errors in the phase and amplitude of the element excitations was investigated in [29]. Such errors can cause an elevation in the sidelobe level and changing the angular locations of the desired nulls. The simulation results showed that the nulls and the sidelobe level in the adaptive arrays are more sensitive to random errors in the element phase excitations as compared to amplitude excitations.

#### 2.3.2 The effect of frequency fluctuation on the generated nulls

In this subsection, we assume that there is a fluctuation in the frequency of operation, or the system works on a certain band of frequencies around the center

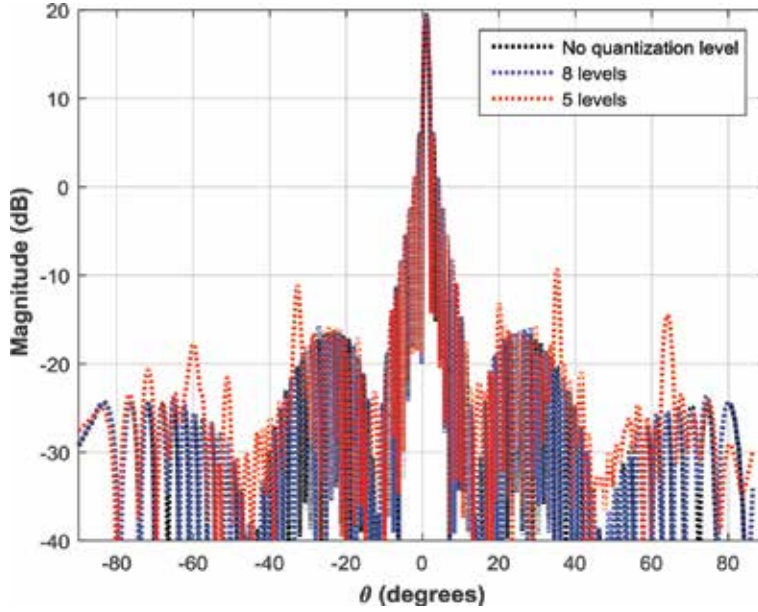


**Figure 14.** Sensitivity of the proposed multiple null steering method to various phase quantization levels.

frequency. It is assumed that the element positions can be accurately fixed at the design frequency  $f_o$ , and element separation is fixed at  $d = \lambda_o/2$ , where  $\lambda_o$  is the free-space wavelength at the frequency  $f_o$ . In this case, the array factor of the uniformly excited equally spaced linear array can be found from [30] as:

$$AF(f, \theta) = \frac{\sin \left[ \frac{Nf}{2f_o} \pi \sin(\theta) \right]}{\sin \left[ \frac{1}{2} \frac{f}{f_o} \pi \sin(\theta) \right]} \quad (5)$$

where  $f$  is instantaneous frequency, and  $f/f_o$  is the fluctuation or deviation ratio. From (5), the angle of the  $n^{\text{th}}$  null  $\theta_n$  as a function of the frequency can be written as [30]:

$$\theta_n(f) = \sin^{-1} \left[ \frac{f_o}{f} \left( \pm \frac{2n}{N} \right) \right] \quad (6)$$

A sample array of  $N = 10$  elements working at an instantaneous frequency  $f$  and design frequency of  $f_o = 3$  GHz is investigated here. **Figure 15**(left) shows the radiation patterns of the uniform array, plotted for frequencies higher than the design value  $f_o = 3$  GHz. It can be seen that the angular location of the first null, in the uniform pattern is  $11.54^\circ$ , whereas this null is shifted to  $9.871^\circ$  when  $f$  is changed from 3 to 3.5 GHz. The figure also shows that, as the frequency departs from the design value  $f_o = 3$  GHz, the nulls move toward main beam resulting in an increased magnitude at the original directions of the nulls. **Figure 15**(right) shows the radiation patterns of the same array plotted for frequencies lower than the design value  $f_o$ . It can be seen that the angular location of the first null is shifted from  $11.54$  to  $13.8^\circ$  when  $f$  is changed from 3 to 2.5 GHz; whereas, the fourth null is shifted from  $53.33$  to  $74.0^\circ$  when  $f$  is changed from 3 to 2.5 GHz. The figure shows that, for frequencies lower than the design value  $f_o = 3$  GHz, the nulls move far from the main beam resulting in an increased magnitude at the original directions of the

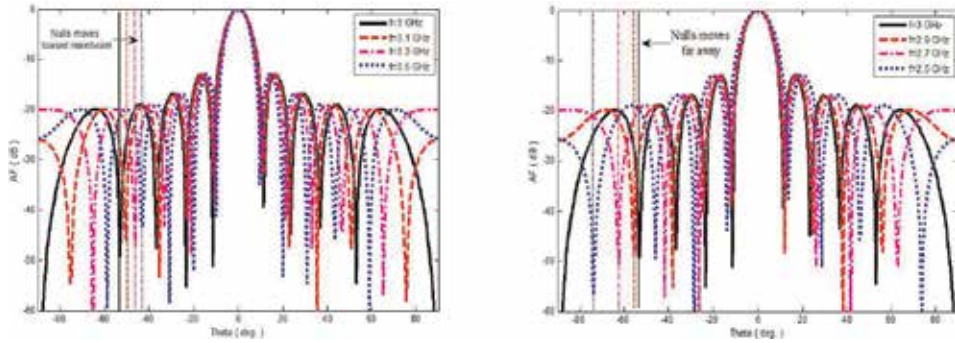


**Figure 15.** The effect of the frequency changes on the null positions for  $N = 10$  elements, and design frequency  $f_0 = 3\text{GHz}$  [30].

nulls. Generally, it is noticed that the nulls positions are sensitive to frequency changes. The sensitivity of the null angle  $\theta_n$  to frequency can be found from Eq. (6) as [30]:

$$\frac{d\theta_n}{df} = \frac{1}{\sqrt{1 - \left(\frac{2mf_0}{Nf}\right)^2}} \quad (7)$$

The above relation shows that the sensitivity is a nonlinear function of the frequency deviation. This nonlinearity can be obviously noticed by comparing **Figure 15**(left) and (right), where a 0.5 GHz change in frequency produces different shifts in the null positions depending if the change is positive or negative. It has been found that a  $\pm 16.7\%$  changes in the frequency result in a shift of 2.26 and 1.67°, respectively, for the first null position. In this example, a relatively large frequency span of 1 GHz has produced null movement of only 3.89°.

### 3. Mechanical null steering methods

As we have shown in the previous section, the practical implementation of the feeding network in the electronically null steering methods is a real challenging issue, especially when dealing with large arrays. To solve this problem, many researchers, for example, see [22–26], proposed to mechanically control the spacing between the array elements instead of electronically controlling the amplitude and/or phase excitations to achieve the required null steering. However, in practice, these fully nonuniform spaced arrays have also some disadvantages and difficulties to build. These difficulties may especially arise when dealing with movable or unknown interfering directions where in such a case it is required to continuously readjust the element positions to achieve the desired null steering. This means that the mechanical position of all elements in an array needs repeatedly to be recalculated and accordingly the whole array elements need to be removed for each specific interfering direction. In such methods of mechanically nonuniform spaced arrays, the simplest way to change the position of the array elements is to use a set of servo-motors connected to each element. For large arrays with fully nonuniform spaced elements, i.e., large number of the movable elements, the computational time (i.e., the number of iterations that are required by the optimization algorithm to converge) becomes a real challenging issue. In addition, an extra time is needed

for mechanical movement of the element positions. Thus, these methods of fully nonuniform spaced arrays were not widely used in practice.

To overcome these problems and make them more amendable in practice, some researchers, for example, see [22–25], have found that the required nulls can be introduced by controlling the positions of only selected elements rather than controlling the positions of all elements.

### 3.1 Fully nonuniform spaced array

Generally, the optimization parameters of the mechanically nonuniformly spaced arrays can be chosen by either in terms of inter-element spacing between successive elements or in terms of absolute positions of the elements from the center of the array. These two structures are illustrated in **Figure 16**. Choosing the second structure in the optimization process may cause the element positions to overlap. The overlapping between any two or more elements may help to remove (or turn it off) some redundant elements for the thinning arrays. Thus, the second structure is considered in the present work.

The far-field radiation pattern of an array consisting of  $N$  isotropic mechanically movable elements that are arranged in nonuniform locations  $x_n$  according to the second structure (see **Figure 16**), can be written by [26]

$$AF(u) = 2 \sum_{n=1}^{N/2} a_n \cos(kx_n u) \quad (8)$$

where  $N$  is assumed an even number, and  $a_n$  is the electronic weighting of the array elements which is chosen to be constant or uniform in this method. In order to introduce the required nulls and at the same time reducing the sidelobe level in the array pattern of (8), the following cost function is used [26]

$$CostFunction = 10 \log_{10} \left[ \max(|AF(u)|^2) + \sum_{i=1}^I |AF(u_{i_{upperbound}} \& u_{i_{lowerbound}})| \right] \quad (9)$$

where  $\lambda/Nd \leq u \leq 1$ , and  $i = 1, 2, \dots, I$ . Note that  $\lambda/Nd$  represents the angular location of the first null in the array pattern and  $I$  represents the total number of the steered nulls. To control the width of the produced nulls, some constraints on the upper and lower bounds are imposed in (9). Note that the first term in (9) corresponds to the peak sidelobe level and the second term corresponds to the required nulls with pre-specified width.

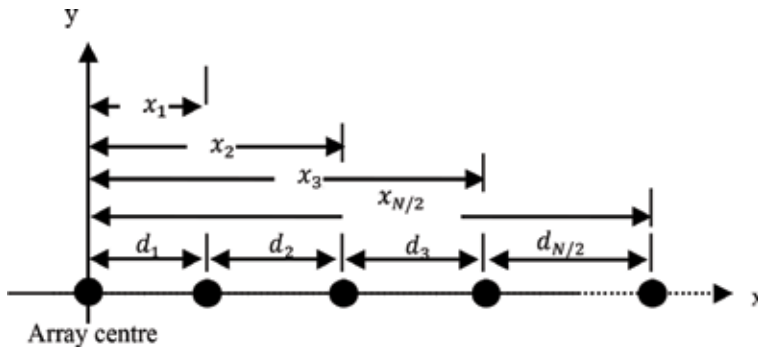


**Figure 16.** Array structures in terms of Inter-element spacing and absolute locations from the array center [26].

As can be seen from (8) and (9), the positions of all elements are needed to be moveable to meet the required goals. To perform such movements, a number of servo-motors equal to  $N$  are needed. These fully mechanical nonuniform spaced arrays may perform very well against the interfering signals that originate from fixed and pre-defined directions. However, such arrays may become impractical in the case of unknown direction or in the case of moving interfering signal (i.e., its incoming direction is changing repeatedly). This means that the designer needs to continuously and quickly recalculate the new location of all elements before the interfering signal can change its direction. Redesigning the array in a very short time interval is really a challenging problem. One effective and simple solution to this important problem is addressed and proposed in [26].

### 3.2 The results

Each wide null at the desired direction is generated by forming two adjacent nulls with a small spacing equal to  $u = 0.02$  around the interfering directions. The effectiveness of the simplified null steering array [26] compared to the fully nonuniform spaced array has been illustrated by the design of 30 elements linear array with the main beam directed toward the broadside. The smoothing, elite sample selection and population parameters of the optimization algorithm are chosen to be 0.7, 0.1, and 100, respectively [26].

In the first example, the fully nonuniform spaced array where all of its elements are made movable is considered. It is assumed that the width of the required nulls in the optimized array are from 0.42 to 0.44 and from 0.61 to 0.63 in  $u$ -space, while the depth of these two nulls is chosen to be  $-40$  dB. Also, it is assumed that the electronic amplitude and phase excitations for all elements in the considered array are uniform, i.e.,  $a_n = 1$ . Note, to maintain the overall array length unchanged, the first and the last array elements' locations are fixed. Moreover, in all cases, the cost function represented in (9) is chosen such that it minimizes the output power at the intended null direction(s), i.e., it contains only the second term while the first term which is responsible for sidelobe reduction is omitted. **Figure 17** shows the radiation pattern of the fully nonuniform spaced array. For comparison, the radiation pattern of the fully uniform spaced array is also shown in **Figure 17**(right). From this figure, it can be seen that the capability of the fully nonuniform spaced array for accomplishing the required nulls is more than satisfactory. This is mainly due to the availability of many degrees of freedom. On the other hand, the sidelobe structure has generally increased by few dBs. This is mainly due to the considered cost function as mentioned earlier. The optimized location of all elements with respect to that of the uniformly spaced array is shown in **Figure 17**(left). Note that, as

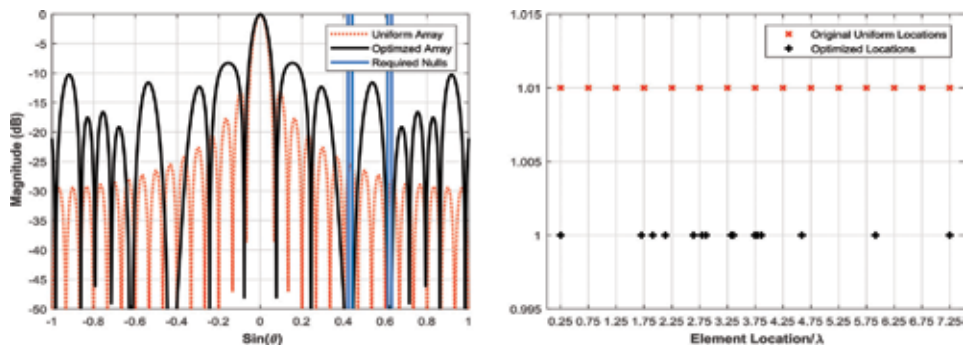


**Figure 17.**  
 Results of fully uniform and nonuniform spaced arrays for  $N = 30$  elements, and two wide nulls.

mentioned earlier, many elements have moved by more than a wavelength, and many of the new locations are overlapped with the formerly adjacent ones. The overlapping may be exploited in the array thinning, while the elements that are located closer than a half wavelength may result in a high mutual coupling. This mutual coupling could completely deteriorate the nulling capability of such arrays. **Table 1** shows the optimized values of the element locations compared to those of the uniformly spaced array.

**Figure 18**(left) shows the variation of the cost function, i.e., output power at the desired nulls, with respect to the iteration number in the optimized fully nonuniform spaced array. It can be seen that it takes more than 140 iterations to reach the required depth of  $-40$  dB. **Figure 18**(right) shows the instantaneous

The Methods			
Element #	Original uniformly spaced array	Fully nonuniform spaced array	
1	0.25	0.2500	
2	0.75	<b>0.7087</b>	
3	1.25	<b>1.0444</b>	
4	1.75	<b>1.3522</b>	
5	2.25	<b>1.9881</b>	
6	2.75	<b>2.3441</b>	
7	3.25	<b>2.8279</b>	
8	3.75	<b>3.1272</b>	
9	4.25	<b>3.5675</b>	
10	4.75	<b>4.0763</b>	
11	5.25	<b>4.5535</b>	
12	5.75	<b>4.8767</b>	
13	6.25	<b>5.7395</b>	
14	6.75	<b>6.5707</b>	
15	7.25	<b>7.2500</b>	

*The bold values represent the optimized values.*

**Table 1.**  
Element locations (in wavelength).

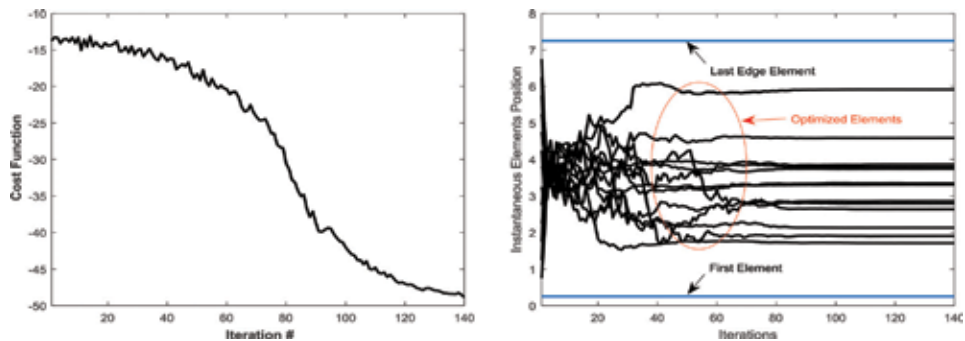


**Figure 18.**  
Convergence speed of the optimizer (left) and the Instantaneous element positions (right).



elements' positions during the optimization process. Note that the initial positions were chosen to start from a uniformly spaced state. Clearly, the computational time that is required by the optimizer to reach the final optimized positions is relatively high since the location of all array elements are made movable. It is shown that the fully nonuniform spaced array performs very well in suppressing the undesired interfering signals, but, at the cost of extra mechanical parts. This problem was efficiently solved in [26] while still maintaining the same performance for interference suppression. More results and discussions can be found in [26].

#### 4. Conclusions

It is shown that the required sidelobe nulling can be accomplished either electronically by controlling the amplitude and/or phase of the excitations of the array elements or mechanically by controlling the positions of all or a small number of the array elements. Each approach has its own advantages and disadvantages. The electronic null steering methods are easy to implement, however, they are associated with some practical problems such as quantization errors which may cause a significant deviation in the desired null directions and finally leads to noticeable performance degradation. On the other hand, the mechanical null steering methods does not need digital attenuator and/or digital phase shifters, thus, they are free from any quantization errors. Instead, each array element in the mechanical null steering methods needs a servo-motor to make the element moveable. If all or most of the array elements are required to be movable, then a considerable extra time is needed for mechanical movement of the elements. This represents a real challenging issue in the practice.

To solve these aforementioned problems that were associated with both electronic and mechanical methods of sidelobe nulling, it is proposed to control only some selected elements rather than controlling all of the array elements that were required for array pattern reconfiguration. The number of the array elements, the operating frequency, and the accuracy at which the desired pattern is needed influence the final choice between the two approaches of electronic and mechanical sidelobe nulling.

#### Author details

Jafar Ramadhan Mohammed\* and Khalil H. Sayidmarie  
College of Electronic Engineering, Ninevah University, Mosul, Iraq

\*Address all correspondence to: [jafarram@yahoo.com](mailto:jafarram@yahoo.com)

#### IntechOpen

© 2019 The Author(s). Licensee IntechOpen. This chapter is distributed under the terms of the Creative Commons Attribution License (<http://creativecommons.org/licenses/by/3.0>), which permits unrestricted use, distribution, and reproduction in any medium, provided the original work is properly cited. 

## References

- [1] Compton RT. Adaptive Antennas. New Jersey: Prentice Hall; 1988
- [2] Van Veen BD, Buckley KM. Beamforming: A versatile approach to spatial filtering. *IEEE ASSP Magazine*. 1988;5(2):4-24
- [3] Haupt RL. Phase-only adaptive nulling with a genetic algorithm. *IEEE Transactions on Antennas and Propagation*. 1997;45(6):1009-1015
- [4] Rocca P, Mailloux RJ, Toso G. Ga-based optimization of irregular subarray layouts for wideband phased arrays design. *IEEE Antennas and Wireless Propagation Letters*. 2015;14:131-134
- [5] Steyskal H, Shore RA, Haupt RL. Methods for null control and their effects on the radiation pattern. *IEEE Transactions on Antennas and Propagation*. 1986;34:404-409
- [6] Rahman SU, Qunsheng C, Muhammad M, Hisham K. Analysis for linear antenna array for minimum sidelobe level, half power beamwidth, and null control using PSO. *Journal of Microwaves, Optoelectronics and Electromagnetic Applications*. 2017;16(2):577-591
- [7] Khodier MM, Christodoulou CG. Linear array geometry synthesis with minimum sidelobe level and null control using particle swarm optimization. *IEEE Transactions on Antennas and Propagation*. 2005;53(8):2674-2679
- [8] Trastoy A, Ares F, Moreno E. Phase-only control of antenna sum and shaped patterns through null perturbation. *IEEE Antennas and Propagation Magazine*. 2001;43(6):45-54
- [9] Smith SK, Bregains JC, Melde KL, Ares F. A comparison of optimization techniques for power patterns with low sidelobes generated by linear arrays with efficient excitation distribution. *Microwave and Optical Technology Letters*. 2005;45(1):57-60
- [10] Prerna S, Ashwin K. Ant Lion Optimization algorithm to control sidelobe level and null depths in linear antenna arrays. *AEU - International Journal of Electronics and Communications*. 2016;70(9):1339-1349
- [11] Gopi R, Durbadal M, Rajib K, Sakti PG. Directivity maximization and optimal far-field pattern of time modulated linear antenna arrays using evolutionary algorithms. *AEU - International Journal of Electronics and Communications*. 2015;69(12):1800-1809
- [12] Banerjee S, Mandal D. Array pattern optimization for a steerable circular isotropic antenna array using the firefly algorithm. *Journal of Computational Electronics*. 2017;16(3):952-976
- [13] Faridani M, Ghalamkari B. Four-element lens array antenna for advanced point-to-(multi)point high-bandwidth wireless communication. *Journal of Computational Electronics*. 2018;17(3):1082-1089
- [14] Mohammed JR, Sayidmarie KH. A new technique for obtaining wide-angular nulling in the sum and difference patterns of monopulse antenna. *IEEE Antennas and Wireless Propagation Letters*. 2012;11:1242-1245
- [15] Mohammed JR. Phased array antenna with ultra-low sidelobes. *Electronics Letters*. 2013;49(17):1055-1056
- [16] Mohammed JR. A new antenna array pattern synthesis method with sidelobe control. *International Journal of Telecommunication, Electronics, and*

Computer Engineering. 2018;**10**(3):  
31-36

[17] Mohammed JR, Sayidmarie KH. Null steering method by controlling two elements. *IET Microwaves, Antennas and Propagation*. 2014;**8**(15):1348-1355

[18] Mohammed JR, Sayidmarie KH. Sidelobe cancellation for uniformly excited planar array antennas by controlling the side elements. *IEEE Antennas and Wireless Propagation Letters*. 2014;**13**:987-990

[19] Mohammed JR, Sayidmarie KH. Synthesizing asymmetric side lobe pattern with steered nulling in nonuniformly excited linear arrays by controlling edge elements. *International Journal of Antennas and Propagation*. 24 May 2017;**2017**:1-7. Article ID: 9293031. <https://doi.org/10.1155/2017/9293031>

[20] Mohammed JR. Optimal null steering method in uniformly excited equally spaced linear arrays by optimizing two edge elements. *Electronics Letters*. 2017;**53**(13):835-837

[21] Mohammed JR. Element selection for optimized multi-wide nulls in almost uniformly excited arrays. *IEEE Antennas and Wireless Propagation Letters*. 2018;**17**(4):629-632

[22] Mohammed JR. Thinning a subset of selected elements for null steering using binary genetic algorithm. *Progress in Electromagnetics Research M*. 2018;**67**: 147-157

[23] Hejres J. Null steering in phased arrays by controlling the positions of selected elements. *IEEE Transactions on Antennas and Propagation*. 2004;**52**(11): 2891-2895

[24] Tokan F, Güneş F. Interference suppression by optimizing the positions of selected elements using generalized pattern search algorithm. *IET*

*Microwaves, Antennas and Propagation*. 2011;**5**(2):127-135

[25] Basbug S. Design and synthesis of antenna array with movable elements along semicircular paths. *IEEE Antennas and Wireless Propagation Letters*. 2017; **16**:3059-3062

[26] Mohammed JR. Obtaining wide steered nulls in linear array patterns by controlling the locations of two edge elements. *AEU - International Journal of Electronics and Communications*. Accepted for publication

[27] Mohammed JR, Sayidmarie KH. Performance evaluation of the adaptive sidelobe canceller system with various auxiliary configurations. *International Journal of Electronics and Communications (AEÜ)*. 2017;**80**: 179-185

[28] Mohammed JR, Sayidmarie KH. Planar array with optimized perimeter elements. In: 2018 Advances in Wireless and Optical Communications (RTUWO); 15–16 November, 2018; Riga, Latvia. Accepted for presentation

[29] Mohammed JR, Sayidmarie KH. Sensitivity of the adaptive nulling to random errors in amplitude and phase excitations in array elements. *International Journal of Telecommunication, Electronics, and Computer Engineering*. 2018;**10**(1): 51-56

[30] Sayidmarie KH, Mohammed JR. Performance of a wide angle and wideband nulling method for phased arrays. *Progress in Electromagnetics Research M*. 2013;**33**:239-249



# Array Pattern Synthesis for ETC Applications

*Daniele Inserra and Guangjun Wen*

## Abstract

The problem of antenna array synthesis for radiation pattern defined on a planar surface will be considered in this chapter. This situation could happen when the electric field  $r$ -decay factor effect cannot be neglected, for example, an antenna array mechanically tilted and a pattern defined in terms of Cartesian coordinates, as in the electronic toll collection (ETC) scenario. Two possible approaches will be presented: the first one aims at the precise synthesis of the pattern in the case both a constant power-bounded area and a sidelobe suppression region are defined and required to be synthesized. The second approach instead devotes at stretching the coverage area toward the travel length (without considering a precise definition of the communication area) to increase the available identification time with an iterative methodology. For the latter, an antenna prototype has been fabricated, and measurement results have confirmed the approach validity.

**Keywords:** antenna arrays, radiation pattern synthesis, linear programming, electronic toll collection (ETC), radio frequency identification (RFID)

## 1. Introduction

Most parts of literature on antenna array describe the synthesis of the *array factor* [1]. In fact, when the antenna array elements are the same, and assuming that the single antenna beamwidth is broader than that of the final array, it is possible to observe that the magnitude of the array factor is proportional to that of the total radiated electric field. Lots of synthesis methodologies have been presented over the years for both simple array structures, for example, linear uniform arrays [2], and more complex geometries (which require the use of optimization algorithms) [3–7]. Nevertheless, there exist other situations which require the whole electric field behavior control and, in particular, its  $r$ -decay behavior. In literature, these problems are called *beam-shaped pattern* or *contoured pattern synthesis*. Possible applications for these methods are in the field of satellite communications where small antennas or antenna arrays are employed for illuminating a profiled reflector, as described in [8]. Besides the use of a profiled reflector, other techniques have been developed and proposed [9–12]. The minimum least square error (MLSE) criteria are used in [9] for the synthesis of a desired contoured pattern specified with points in the angular domain. Moreover, a discrete Fourier transform (DFT) shape of the synthesis function is assigned to provide a better radiation control. In [10], a successive projection

method (SPM) procedure is developed which exploits a new set of basis functions instead of the DFT. This reduces the number of optimization variables with respect to the conventional SPM [11]. Another example of synthesis technique which minimizes the difference with a desired pattern in an iterative fashion can be found in [12].

Besides the case of satellite communications, there exist other applications in the context of vehicular communications and, in particular, for vehicle-to-infrastructure connection and vice versa, in which the electric field  $r$ -decay behavior affects the beam pattern, for example, a road side unit (RSU) equipped with an antenna array which has to radiate toward a specific area, defined on the road surface, for dedicated short-range communications (DSRC). This specific problem is usually not addressed as a beam-shaped pattern problem because nowadays electronic toll collection (ETC) is still performed with low-speed dedicated corridor sufficient to guarantee the automatic vehicle identification (AVI). However, in the futuristic envision of multilane free flow (MLFF) in which vehicles will perform tolling operation without reducing travel speed [13], an efficient beam pattern synthesis will become fundamental. In order to better highlight this point, let us consider **Figure 1**, in which a MLFF situation is depicted. In this example, each roadlane is managed by a dedicated RSU antenna array which radiates a certain beam pattern on the road surface.

If this beam pattern is synthesized for guaranteeing the correct communication between RSU and on-board unit (OBU) within a certain coverage area of length  $l_{ca}$ , it is possible to approximate the maximum available time to perform the toll transaction  $\tau_{trav}$  as a function of the vehicle speed  $v_{car}$ , as shown in **Figure 2** [14]. Obviously, the vehicle speed increase reduces the available transaction time, making the ETC system design more challenging. Nonetheless, the length of the coverage area  $l_{ca}$  is also fundamental to increase the available transaction time and relax the ETC system requirements, and for this reason, the antenna array beam pattern synthesis should be carefully optimized.

Motivated by the above considerations, the problem of antenna array synthesis when the electric field  $r$ -decay effect cannot be neglected is treated in this chapter, with particular emphasis on the context of vehicular communications where a RSU equipped with a mechanically tilted antenna array has to radiate a beam pattern defined on the road surface. The problem will be addressed in two different ways: firstly, a generic optimization problem will be presented for the case of a precise pattern definition; a circular objective area will be considered and synthesized together with a suppression surrounding area (useful for guaranteeing a minimum sidelobe level margin) [15]; and then, the coverage area stretching toward the travel

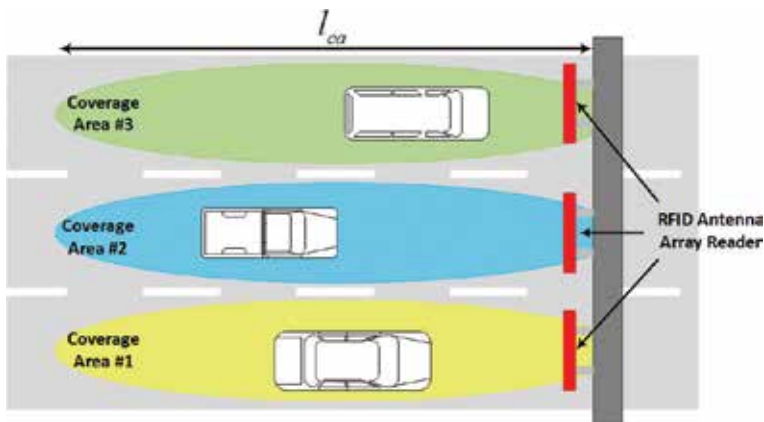


**Figure 1.** Example of three-roadway highway tolling system with RFID antenna reader.

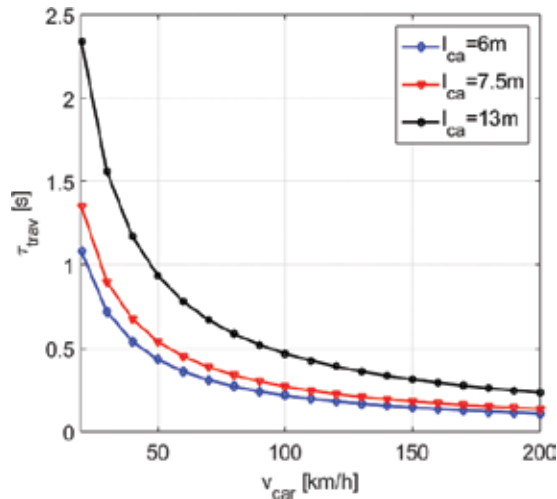


**Figure 2.**  
 Maximum available transaction time as function of the vehicle speed.

direction will be investigated with the objective of increasing the available transaction time for radio frequency identification (RFID)-based DSRC, and a simple iterative approach will be presented [16]. Both the presented methodologies will be analyzed with the aid of numerical results. Moreover, the second approach will be confirmed by experimental results.

## 2. Problem statement and reference system description

Let us consider the design of an antenna array. The total electric field radiated by an array of identical antenna elements can be written by using the well-known pattern multiplication property [2] and reads

$$\bar{E}_{tot}(r, \phi, \theta) = \bar{E}_0(r, \phi, \theta) \cdot AF(\phi, \theta) \quad (1)$$

where  $\bar{E}_0(r, \phi, \theta)$  is the single antenna electric field vector and  $AF(\phi, \theta)$  is the array factor. By assuming that the single antenna beamwidth is broader than the desired one, only the term  $AF(\phi, \theta)$  can be considered in the design. Nonetheless, the single antenna radiation pattern can also be included in the synthesis process. In fact, if  $\bar{E}_0(r, \phi, \theta)$  can be decomposed as

$$\bar{E}_0(r, \phi, \theta) = \frac{e^{-jk_0 r}}{r} (E_\phi \cdot \hat{\phi} + E_\theta \cdot \hat{\theta}) \quad (2)$$

where  $k_0$  is the wavenumber, and if the maximum absolute value of the electric field components is  $E_0$ , then it is possible to define the function:

$$f(\phi, \theta) = \sqrt{\left(\frac{E_\phi}{E_0}\right)^2 + \left(\frac{E_\theta}{E_0}\right)^2} \quad (3)$$

and to include it into the synthesis process, that is, the function that has to be synthesized becomes  $f(\phi, \theta) \cdot AR(\phi, \theta)$ . The function  $f(\phi, \theta)$  is usually called *antenna pattern*.

It is now clear that the distance  $r$  is not included in the synthesis process. For this reason, the synthesized pattern preserves its characteristics uniquely on an  $r$ -constant surface, that is, a spherical surface. If an arbitrarily beam-shaped pattern is required to be synthesized (a pattern defined on a nonspherical surface), the  $r$ -decay factor of  $\bar{E}_0(r, \phi, \theta)$  must be included into the synthesis process. For this reason, the normalized function that has to be optimized becomes

$$F(\phi, \theta) = \frac{r_0}{r} \frac{f(\phi, \theta)}{f(\phi_0, \theta_0)} \cdot AF(\phi, \theta) \quad (4)$$

where  $(\phi_0, \theta_0)$  is the electrical steering direction and  $r_0$  is the reference distance from the antenna array to the synthesis surface (included for function normalization).

Let us assume a RSU with an antenna array placed at height  $h_A$  which can be mechanically tilted by an angle  $\theta_A$  (this can be required to better address a specific coverage area requirement on a planar surface). In this case, both the array electrical steering direction  $(\phi_0, \theta_0)$  and the mechanical tilt steer the beam pattern. **Figure 3(a)** describes this scenario. The coverage area (herein defined as the region where the normalized total electric field on the road surface is larger than a certain threshold value) could be arbitrarily assigned in shape, even if circular or elliptical is a more realistic hypothesis. A coverage area might be required for high-power reception within a high data-rate service spatial area or to guarantee signal reception as it will be described later for the specific case of RFID-based ETC. Furthermore, the synthesized beam sidelobe-level control might also be important to avoid signal interference with other coverage zones illuminated by other RSUs as in **Figure 3(b)**. Finally, other situations could require to limit the coverage area extension toward a specific direction in order to avoid possible overlap with other coverage areas.

**Figure 4** depicts the antenna array reference system in spherical coordinates  $r$ ,  $\phi$ , and  $\theta$  and in Cartesian coordinates  $x$ ,  $y$ , and  $z$  and the coverage area reference system in Cartesian coordinates  $x_R$ ,  $y_R$ , and  $z_R$ . Moreover, a RSU is placed on a  $h_A$  height pole (or a highway gate tolling station), and the coverage area is defined on the road plane, that is,  $z_R = 0$ . However, the presented methodology can also address the case in which  $z_R = h_{tag}$ . It is worth noting that  $h_{tag}$  which represents the OBU height (usually installed on the vehicle windshield) depends on the vehicle model and a univocal solution for the coverage area at a fixed height cannot be specified. For this reason, a reference OBU height can be defined for carrying out the synthesis process of the antenna array, and then synthesis results at different heights  $h_{tag}$  should be verified.

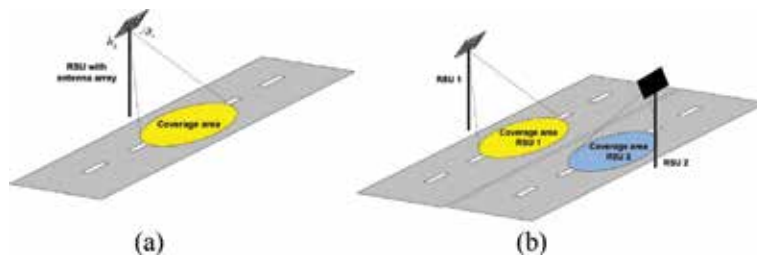


**Figure 3.** Example of RSU displacement and coverage areas. (a) RSU with a coverage area defined on a road surface and (b) RSUs with close coverage areas.



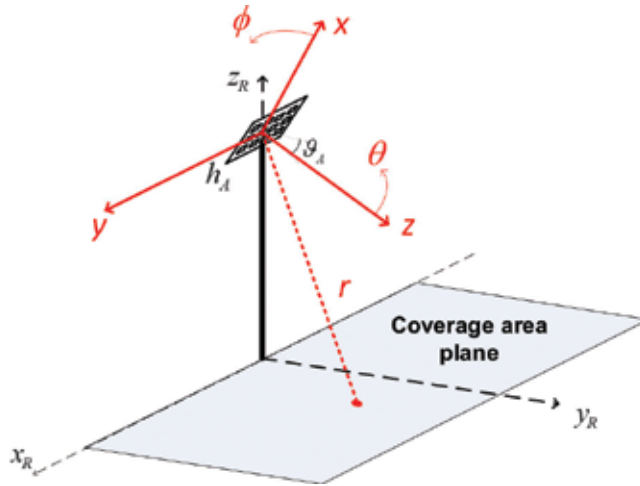


**Figure 4.**  
 Antenna array and coverage area reference systems.

The antenna array reference system can be obtained by a rototranslation of the coverage area reference system [17]. Particularly, the following relations can be obtained:

$$\begin{cases} x_R = y \\ y_R = \cos(\theta_A)z - \sin(\theta_A)x \\ z_R = \sin(\theta_A)z + \cos(\theta_A)x + h_A \\ x = \sin(\theta_A)y_R + \cos(\theta_A)(z_R - h_A) \\ y = x_R \\ z = \cos(\theta_A)y_R - \sin(\theta_A)(z_R - h_A) \end{cases} \quad (5)$$

$$\begin{cases} r = \sqrt{x_R^2 + y_R^2 + (z_R - h_A)^2} \\ \phi = \arctan \left\{ \frac{x_R}{\sin(\theta_A)y_R + \cos(\theta_A)(z_R - h_A)} \right\} \\ \theta = \arccos \left\{ \frac{\cos(\theta_A)y_R - \sin(\theta_A)(z_R - h_A)}{\sqrt{x_R^2 + y_R^2 + (z_R - h_A)^2}} \right\} \end{cases}$$

It should be noted that other synthesis surfaces could be considered with the method herein presented. For the sake of comprehension simplification, and also because it represents a practical situation, the case  $z_R$  constant is herein described. In this case, it is straightforward to understand that  $r = r(\phi, \theta)$ , and then also the normalized function  $F(r, \phi, \theta)$  in (4) becomes  $F = F(\phi, \theta)$ .

### 3. Optimization problem and antenna array synthesis

A generic planar array of  $N$  elements lying on the  $xy$ -plane of **Figure 4** is assumed. The synthesis function in (4) can be written as follows:

$$F(\phi, \theta) = \frac{r_0}{r} \frac{f(\phi, \theta)}{f(\phi_0, \theta_0)} \sum_{n=1}^N w_n e^{j(k_x x_n + k_y y_n)} \quad (6)$$

where  $k_x = \frac{2\pi}{\lambda_0} \cos(\phi) \sin(\theta)$ ,  $k_y = \frac{2\pi}{\lambda_0} \sin(\phi) \sin(\theta)$ ,  $w_n$  is the  $n$ th element amplitude excitation,  $w_n \in \mathbb{C}$ ,  $n \in \{1, \dots, N\}$  [18], and  $(x_n, y_n)$  is the position of the  $n$ th antenna element on the  $xy$ -plane. Let us now consider the case of a synthesis on the plane  $z_R = 0$  as illustrated in **Figure 4**. Defining a suppression region  $\Sigma$ , where the maximum sidelobe level  $t = \max_{(\phi_i, \theta_i) \in \Sigma} |F(\phi_i, \theta_i)|$  has to be minimized, that is,

$$|F(\phi_i, \theta_i)| \leq t, (\phi_i, \theta_i) \in \Sigma \quad (7)$$

and a coverage area  $C$ , where it is desired that the normalized electric field is larger than a certain bound value  $P_{bound}$  (expressed in dB), that is,

$$|F(\phi_k, \theta_k)| \geq 10^{P_{bound}/20}, (\phi_k, \theta_k) \in C \quad (8)$$

it is possible to derive the generic optimization problem as

$$\begin{aligned} & \min_{\phi_0, \theta_0, w_n, n \in \{1, \dots, N\}} t \\ \text{s.t.} \quad & F(\phi_0, \theta_0) = 1 \\ & |F(\phi_i, \theta_i)| \leq t, (\phi_i, \theta_i) \in \Sigma \\ & |F(\phi_j, \theta_j)| = 10^{P_{bound}/20}, (\phi_j, \theta_j) \in B \\ & |F(\phi_h, \theta_h)| \leq 10^{P_{bound}/20}, (\phi_h, \theta_h) \in \Omega \\ & |F(\phi_k, \theta_k)| \leq 1, (\phi_k, \theta_k) \in C \\ & |F(\phi_k, \theta_k)| \geq 10^{P_{bound}/20}, (\phi_k, \theta_k) \in C \end{aligned} \quad (9)$$

Some additional constraints are included to better define the function trend within the area of interest. In particular, the constraint  $|F(\phi_j, \theta_j)| = 10^{P_{bound}/20}, (\phi_j, \theta_j) \in B$  fixes the function value on the coverage area bound  $B$ , while  $|F(\phi_h, \theta_h)| \leq 10^{P_{bound}/20}, (\phi_h, \theta_h) \in \Omega$  defines a criterion within  $\Omega$  that is the space between the coverage area and the suppression region. It is worth noting that  $(\phi_i, \theta_i)$  are related to the coordinates  $x_R$  and  $y_R$  according to (5).

The mechanical tilt  $\theta_A$  has not been included in the optimization problem because its choice is usually not arbitrary. It could be preliminarily selected to radiate toward a specific direction, and its choice is left to common sense.

### 3.1 Derivation of suboptimal problem

The steering direction  $(\phi_0, \theta_0)$  and the last inequality in (9) lead to a nonlinear optimization problem with a non-convex constraint, and according to [5], the global optimality cannot be guaranteed, with computation time extremely large.

Two hypotheses have been considered for reducing the problem complexity. In particular, a known steering direction  $(\phi_0, \theta_0)$  and symmetric antenna array with respect to the axes origin are assumed. Since there is no way to know a priori the optimum steering direction, the first hypothesis will lead to a suboptimal solution based on a common sense selection of the steering direction. Furthermore, it has been observed experimentally that if the array pattern is steered toward the center

point of the coverage area, this always leads to a feasible solution with an acceptable array size. Another criterion for the steering direction choice is to select  $(\phi_0, \theta_0)$  in order to synthesize the array factor as much symmetrical as possible [15].

The second hypothesis, instead, addresses the most part of practical cases.

Based on the choice of the steering direction  $(\phi_0, \theta_0)$ , two main practical cases can be distinguished: the broadside array  $(\phi_0 = 0, \theta_0 = 0)$  and the steered array  $(\phi_0 \neq 0, \theta_0 \neq 0)$ .

### 3.1.1 Broadside array

The broadside array is the most considered case for practical usage. Under the hypothesis of symmetric antenna array with respect to the axes origin, the synthesis function in (4) can be written as follows:

$$F(\phi, \theta) = 2 \frac{r_0}{r} \frac{f(\phi, \theta)}{f(\phi_0, \theta_0)} \sum_{n=1}^{N/2} w_n \cos(k_x x_n + k_y y_n) \quad (10)$$

In this case, the amplitude excitations  $w_n \in \mathbb{R}, n \in \{1, \dots, N\}$  [18], and, consequently, the function  $F(\phi, \theta)$  are real. In this way, the lower bound inequality in (9) can be rewritten as a convex constraint. In fact, since the real function  $F(\phi, \theta)$  is close to its maximum value in the bounded area  $C$ , it is plausible that within  $C$  it is also strictly positive; thus, the inequality can be simplified as

$F(\phi_k, \theta_k) \geq 10^{P_{\text{bound}}/20}, (\phi_k, \theta_k) \in C$ , and, finally, written in the form  $-F(\phi_k, \theta_k) \leq 10^{P_{\text{bound}}/20}, (\phi_k, \theta_k) \in C$  that can be included as a convex constraint in the optimization.

The optimization problem (9) for the broadside direction can now be written as

$$\begin{aligned} \min_{w_n, n \in \{1, \dots, N\}} \quad & t \\ \text{s.t.} \quad & F(\phi_0, \theta_0) = 1 \\ & |F(\phi_i, \theta_i)| \leq t, (\phi_i, \theta_i) \in \Sigma \\ & F(\phi_j, \theta_j) = 10^{\frac{P_{\text{bound}}}{20}}, (\phi_j, \theta_j) \in B \\ & |F(\phi_h, \theta_h)| \leq 10^{\frac{P_{\text{bound}}}{20}}, (\phi_h, \theta_h) \in \Omega \\ & F(\phi_k, \theta_k) \leq 1, (\phi_k, \theta_k) \in C \\ & -F(\phi_k, \theta_k) \leq -10^{\frac{P_{\text{bound}}}{20}}, (\phi_k, \theta_k) \in C \end{aligned} \quad (11)$$

The last constraint has been introduced because in the case of a high number of antennas, the array factor exhibits very large oscillations which might cause the function  $F(\phi, \theta)$  to be lower than  $10^{P_{\text{bound}}/20}$  within the coverage area.

The optimization problem in (11) can now be written in the form of a linear program as described in [15] with the great advantage of a lower computational complexity.

### 3.1.2 Non-broadside array

When the mechanical tilt  $\theta_A$  cannot be arbitrarily steered to comply with a specific coverage direction, or if it is necessary to synthesize more coverage areas toward different directions, the synthesis function in (4) is not real because  $w_n \in \mathbb{C}, n \in \{1, \dots, N\}$ . For this reason, another simplification of the problem is herein

proposed. In fact, if a particular shape of the weights is chosen, that is,

$w_n = a_n e^{-j(k_{x,0}x_n + k_{y,0}y_n)}$ , where  $a_n \in \mathbb{R}$ ,  $n \in \{1, \dots, N\}$ ,  $k_{x,0} = k_x(\phi = \phi_0, \theta = \theta_0)$ , and  $k_{y,0} = k_y(\phi = \phi_0, \theta = \theta_0)$ , the synthesis function (4) reads

$$F(\phi, \theta) = 2 \frac{r_0}{r} \frac{f(\phi, \theta)}{f(\phi_0, \theta_0)} \cdot \sum_{n=1}^{\frac{N}{2}} a_n \cos[(k_x - k_{x,0})x_n + (k_y - k_{y,0})y_n] \quad (12)$$

which is again a real function. As for the broadside array case, the optimization problem (9) in the known direction  $(\phi_0, \theta_0)$  can be simplified as (11) and written in the form of a linear program as described in [15].

### 3.2 Simulation results

In this section, some numerical results which demonstrate the capability of the described method are presented. A circular shape for both the coverage area and the suppression region is considered, with diameter of 3.5 and 6.5 m, respectively. The two regions are centered in  $(0, y_0)$  and  $h_A = 5.5$  m. A rectangular array of  $N_x \times N_y$  elements with uniform interelement distance  $d = 0.6\lambda_0$  is synthesized, with antenna elements as microstrip patch antennas (theoretical formula of the radiation pattern  $f(\phi, \theta)$  has been taken as reported in [2, 19]).

The linear problem has been solved by the function **linprog** of the commercial software MATLAB [20]. The optimization has been done with a resolution of 0.25 m on the coverage area plane, with a total of 120,000 points. Both the coverage area and suppression region boundaries have been discretized with four points.

The antenna array normalized electric field when  $\theta_A = 60^\circ$ ,  $y_0 = 3.25$  m, and  $P_{\text{bound}} = -10$  dB is shown in **Figure 5(a)**, achieved with the broadside optimization and an array of size  $16 \times 12$ . **Figure 5(b)** also depicts the contour plot of the synthesized normalized electric field.

Good agreement between the required coverage area and the synthesized one confirms the capability of the proposed method. Furthermore, this result has been obtained in less than 2 minutes with a 2.6 GHz Intel Core i7 processor, which is important to prove the good trade-off between performance and computational complexity are achieved by the described solution.

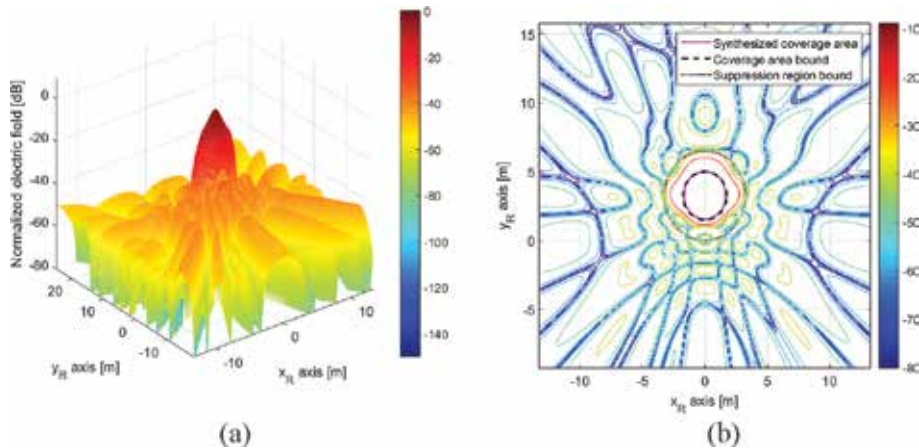


**Figure 5.** Antenna array normalized electric field with an array of size  $16 \times 12$  when  $\theta_A = 60^\circ$ ,  $y_0 = 3.25$  m,  $P_{\text{bound}} = -10$  dB, and broadside optimization. (a) Normalized electric field in  $x_R$  and  $y_R$  axes and (b) normalized electric field contour plot.

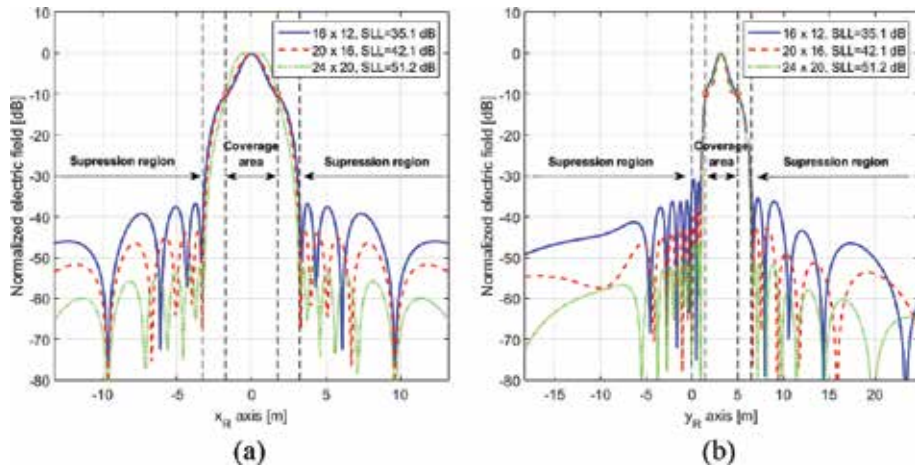


**Figure 6.** Antenna array normalized electric field with different numbers of antenna elements, with  $\theta_A = 60^\circ$ ,  $y_0 = 3.25$  m,  $P_{\text{bound}} = -10$  dB, and broadside optimization. (a) Normalized electric field in  $x_R$  axis, within  $y_R = 3.25$  m, and (b) normalized electric field in  $y_R$  axis, within  $x_R = 0$  m.

Now, the effectiveness of the proposed method is investigated for different synthesis parameters.

The broadside optimization presented in Section 3.1.1 is firstly analyzed for different numbers of antenna elements. Results are reported in **Figure 6** as a function of the coordinates  $x_R$  and  $y_R$ , with  $\theta_A = 60^\circ$ ,  $y_0 = 3.25$  m, and  $P_{\text{bound}} = -10$  dB.

The curve  $16 \times 12$  is the first feasible result which presents a sidelobe level of 35.1 dB within the suppression region. Other curves have been obtained with increased number of antenna elements. Obviously, the sidelobe-level performance improves with the increase of the antenna elements. All the synthesized results respect the  $P_{\text{bound}}$  constraint.

The influence of the mechanical tilt  $\theta_A$  choice on the optimization result is herein investigated. Broadside optimization along with the coordinate  $y_R$  for different mechanical tilt  $\theta_A$  is depicted in **Figure 7(a)**. It is worth noting that the coverage

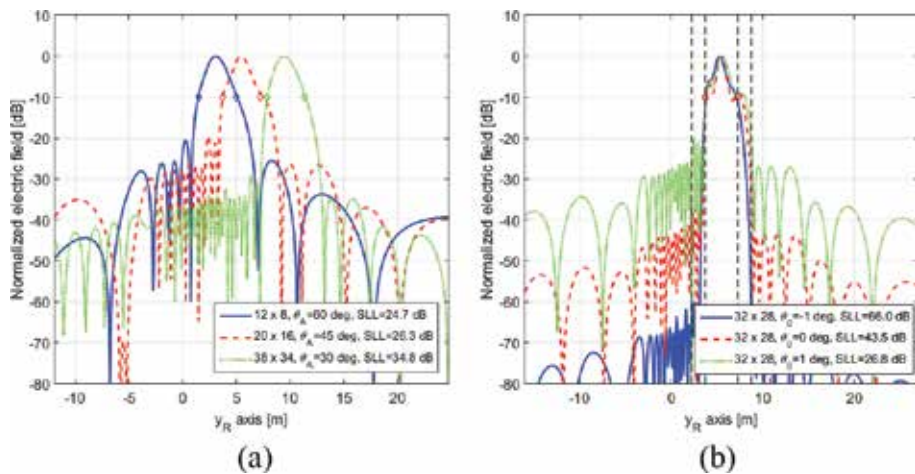


**Figure 7.** (a) Antenna array normalized electric field with different mechanical tilt  $\theta_A$  in  $x_R = 0$  m, with  $P_{\text{bound}} = -10$  dB, and broadside optimization and (b) antenna array normalized electric field with different steering directions  $\theta_0$  in  $x_0 = 0$  m, with  $y_0 = 3.25$  m, and  $P_{\text{bound}} = -10$  dB.

area center position  $y_0$  has been progressively increased to be the points on the coverage area plane which corresponds to the broadside direction, that is,  $y_0 = 3.25$  m with  $\theta_A = 60^\circ$ ,  $y_0 = 5.5$  m with  $\theta_A = 45^\circ$ , and  $y_0 = 9.5$  m with  $\theta_A = 30^\circ$ , and that the array is assumed to be of minimum size.

It is of interest to observe that a decrease in mechanical tilt leads to a decrease in the required beamwidth and, consequently, an increase in the required array size. The achieved sidelobe levels are larger than 20 dB.

The non-broadside case is also considered. In **Figure 7(b)** the performance of the broadside optimization and the non-broadside optimization is compared in order to confirm the steering direction choice discussed in Section 3.1.

It is clear from **Figure 7(b)** that the choice of the steering direction affects the sidelobe level outside the coverage area. In fact, a  $1^\circ$  decrease in the steering direction with respect to the broadside, that is, the steering direction which corresponds to the coverage area center point, yields a sidelobe-level improvement of 22.5 dB. On the other hand, an increase of  $1^\circ$  leads to a sidelobe deterioration.

## 4. Coverage area synthesis for RFID-based ETC system

After the description of a general optimization procedure for a pattern defined on a planar surface (which can be used for the synthesis of a high data-rate service area), in this section we will consider the coverage area synthesis problem from the ETC application point of view. As briefly described in Section 1, the objective of a coverage area synthesis in this context should be the maximization of the communication area length in the travel direction and not the synthesis of a specific pattern geometry. For this case, an optimization procedure similar to the one described in Section 3 might also be derived. Nonetheless, channel phenomena, for example, fading [21], are known and, together with other possible implementation tolerances, might lead to suboptimal solutions in spite of the synthesis effort.

For this reason, a simple iterative methodology for synthesizing a planar antenna array with both the aim of stretching the coverage area toward the longitudinal direction and confining it within a roadlane is described. This method has the advantage of providing acceptable results with a reduced number of antenna elements with respect to the optimization presented in Section 3.

### 4.1 RFID-based DSRC system

RFID technology is usually employed for the implementation of DSRC because of its well-known advantages of excellent accuracy and the possibility to be read at high speed [22]. A RFID-based DSRC system is basically realized by means of a RSU beacon reader, raised installed in order to guarantee sufficient visibility, and some OBU transponders. Moreover, antennas are constrained to radiate with circular polarization (CP) for two main reasons: CP reduces polarization mismatch due to reciprocal rotation between RSU and OBU devices and improves immunity to multipath effect [23]. The latter is a fundamental characteristic which guarantees the validity of a free space propagation loss model [21].

The coverage area definition is based on the threshold power  $P_{\text{bound}}$  which, in the case of a monostatic backscatter [22] RFID-based system, can be interpreted as the tag sensitivity threshold  $P_{\text{tag, th}}$  and the reader sensitivity  $P_{\text{reader, th}}$ . Therefore,

according to the free space propagation model, the communication area is defined as the set of coordinates  $x_R$  and  $y_R$  in the reference plane  $z_R = h_{tag}$  in which

$$\begin{cases} P_{\text{forward}}(x_R, y_R) = P_t + G_t(\phi, \theta) + G_r + 20 \log_{10} \left( \frac{\lambda_0}{4\pi r} \right) \geq P_{\text{tag, th}} \\ P_{\text{back}}(x_R, y_R) = P_{\text{forward}}(x_R, y_R) + G_t(\phi, \theta) + G_r + 20 \log_{10} \left( \frac{\lambda_0}{4\pi r} \right) + 10 \log_{10} M \geq P_{\text{reader, th}} \end{cases} \quad (13)$$

where  $P_t$  is the transmitted power,  $G_t(\phi, \theta) = G_{t, \max} + 20 \log_{10} F(\phi, \theta)$  represents the antenna array gain pattern (which includes the normalized synthesis function),  $G_r$  is the tag gain, and  $M$  is the modulation factor (for a passive tag,  $M = 0.25$  [22]).

## 4.2 Antenna array synthesis with iterative method

Let us consider the normalized synthesis function in (6) for a rectangular planar array of  $N_x \times N_y$  elements with uniform interelement distances  $d_x$  and  $d_y$  which can be rewritten as

$$F(\phi, \theta) = \frac{r_0}{r} \frac{f(\phi, \theta)}{f(\phi_0, \theta_0)} \sum_{n=1}^{N_x} \sum_{m=1}^{N_y} w_{n,m} e^{j[k_x(n-1)d_x + k_y(m-1)d_y]} \quad (14)$$

The synthesis problem is basically the definition of:

- Number of antenna elements  $N_x$  and  $N_y$
- Interelement distances  $d_x$  and  $d_y$
- Complex excitations  $w_{n,m}$

A simple iterative method to synthesize the coverage area with the objective of stretching its length toward the travel direction is described [16]. In this case, complex coefficients  $w_{n,m}$  are taken as in (12), that is,

$w_{n,m} = a_{n,m} e^{j[(k_x - k_{x,0})(n-1)d_x + (k_y - k_{y,0})(m-1)d_y]}$ , with  $a_{n,m}$  based on Tschebyscheff coefficients and  $R_x$  and  $R_y$  the Tschebyscheff design sidelobe level [2].

Then, the synthesis process can be performed according to the following steps:

1. Initialize the steering direction toward broadside ( $\phi_0 = 0, \theta_0 = 0$ ),  $R_x = R_y = 10$  dB, and the parameters  $d_x$  and  $d_y$  according to the antenna design requirements, for example, directivity, mutual coupling, size constraints, etc.
2. Starting from a minimum size  $N_x = 2$  and  $N_y = 2$ , increase the antenna array dimension  $N_y$  to cover a little bit more than the required transverse width.
3. Adjust the sidelobe level  $R_y$  according to the required horizontal power margin requirements.
4. Increase the antenna array dimension  $N_x$  in accordance with the antenna gain requirements.
5. Adjust the sidelobe level  $R_x$  to obtain the required vertical power margin.

6. Choose the best steering elevation  $\theta_0$  in the sense of maximizing the length of the coverage area along with the coordinate  $y_R$  (with starting coordinate  $y_R = 0$ ).

Each step is iteratively executed to compare the Tschebyscheff synthesis results and verify the conditions in (13) and then determine the coefficients  $a_{n,m}$ .

### 4.3 Synthesis example and experimental results

A coverage area synthesis is herein described for the case of a reader height  $h_A = 5.5$  m with mechanical tilt  $\theta_A = 45^\circ$ . and OBU height  $h_{tag} = 1.5$  m. System parameters are chosen according to the standard EPC Gen2 for UHF RFID [24] for the carrier frequency 920 MHz which limits the *effective isotropic radiated power* to the value  $P_{EIRP} = P_t + G_{t,max} = 36$  dBm. After that, the other parameters are  $G_r = 5$  dBi,  $P_{tag,th} = -20$  dBm (the sensitivity of the commercial product Impinj Monza R6 [25]), and  $P_{reader,tag} = -84$  dBm (the sensitivity of the commercial product Impinj Indy R2000 [26]).

Following the synthesis process described above, the optimized coverage area for a 6 m road width is achieved as depicted in **Figure 8(a)**, with the following synthesis parameters:  $N_x = 4$ ,  $N_y = 4$ ,  $d_x = 0.45\lambda_0$ ,  $d_y = 0.48\lambda_0$  (with  $\lambda_0$  evaluated at 920 MHz),  $\theta_0 = -5^\circ$ ,  $R_x = 30$  dB,  $R_y = 25$  dB, and the coefficients as in [27].

The achieved coverage area is 8 m long, covers the required transversal direction width, and presents very low lateral sidelobes. **Figure 8(b)** also presents the achieved coverage area at  $h_{tag} = 2.5$  m (it could represent the tag height of a truck) and  $h_{tag} = 1$  m (that can represent the tag height of a motorcycle) along with the coordinate  $y_R$ , and it shows that the higher the tag height  $h_{tag}$ , the shorter the coverage area. This is acceptable because the speed of a truck is usually lower than the speed of a common vehicle, so the available transaction time will be longer.

In order to confirm the simulation results, the synthesized antenna array has been designed and manufactured, as shown in **Figure 9(a)**. The design process of the  $4 \times 4$  CP microstrip patch antenna array is described in [27]. Furthermore, the 12 dBi RHCP gain antenna prototype has been fixed at the height  $h_A = 5.5$  m with a metallic scaffolding and used for collecting experimental results, as depicted in **Figure 9(b)**. A commercial Impinj Speedway R420 UHF reader [28] ( $P_{reader,th} = -84$  dBm) and a tag device with  $P_{tag,th} = -32$  dBm have been

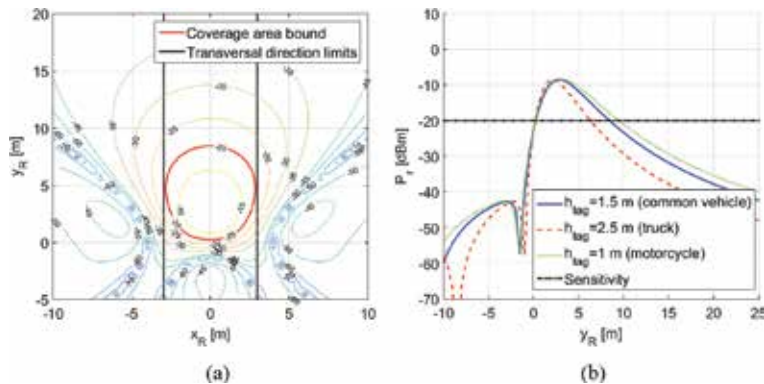


**Figure 8.** Synthesis example of the coverage area at 920 MHz. (a) Received power contour plot at  $h_{tag} = 1.5$  m and (b) received power profile along  $y_R$  coordinate as function of the tag height  $h_{tag}$ .





**Figure 9.** (a) 4 x 4 CP microstrip patch antenna array fabricated prototype and (b) experimental setup for the ETC antenna array system measurement.

employed. A compact CP UHF antenna with gain  $G_r = 4$  dBi has been used as tag antenna.

The transmitted power  $P_t$  has been regulated in the range  $5 \div 30$  dBm for each position of the tag device in the road plane  $(x_R, y_R)$  to determine the minimum value  $P_{t, min}$  which activates the tag, that is,  $P_{forward}(x_R, y_R) = P_{t, min} + G_t(\phi, \theta) + G_r + 20 \log_{10}(\frac{\lambda_0}{4\pi r}) = P_{tag, th}$ , under the condition that  $P_{back}(x_R, y_R) \geq P_{reader, th}$ . After that, in a similar way to what has been described in [29], the power  $P_{forward}(x_R, y_R)$  when a limited  $P_{EIRP} = 36$  dBm is applied and a specific  $P_{tag, th} = -20$  dBm is chosen has been inferred as  $P_{forward}(x_R, y_R) = P_{tag, th} + P_{EIRP} - P_{t, min} - G_{t, max}$  (cable losses have been compensated during the power evaluation). Experimental results are shown in **Figure 10(a)** and **(b)**.

Good correspondence among simulations (SR), antenna measurement projection on the road plane (AM), and experimental results (ER) is visible, and only few discrepancies arise. These are mainly due to the 1 dB tag antenna gain reduction with respect to the design parameter, the tag antenna radiation pattern (not taken into account), and other possible errors in fixing the antenna mechanical tilt  $\theta_A$ .

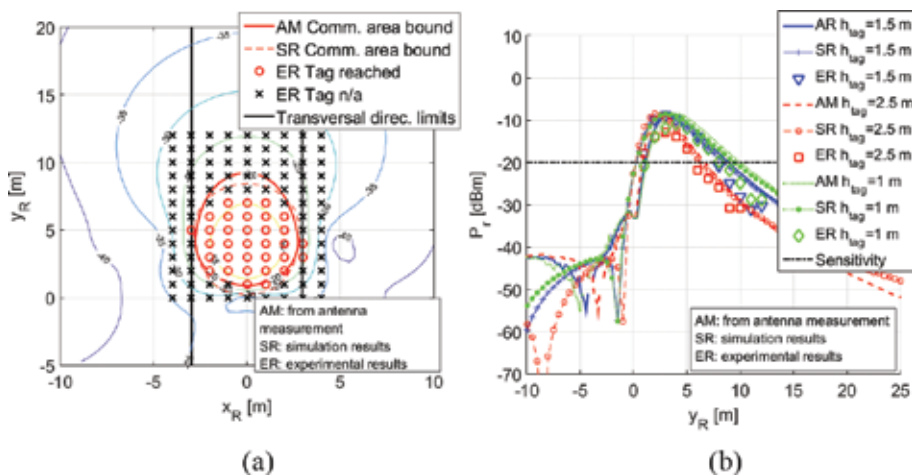


**Figure 10.** Comparison of synthesis results obtained by projecting the measurement results of the antenna to the road plane (AM), simulation (SR), and experimental results (ER). (a) Received power contour plot at  $h_{tag} = 1.5$  m and (b) received power profile along  $y_R$  coordinate as function of  $h_{tag}$ .

## 5. Conclusions

The optimization of an antenna array pattern when the electric field  $r$ -decay factor effect cannot be neglected has been described, with particular emphasis on the context of DSRC systems. In fact, in order to maximize the available transaction time of ETC for future MLFF, it has been shown that particular attention has to be dedicated to the antenna array beam pattern synthesis on the road surface (or in a parallel surface plane). The generic optimization problem of a beam pattern defined on a planar surface has been introduced with the concept of coverage area. The coverage area is a bounded portion of the space in which the communication between RSU and OBU has to be guaranteed. After that, an optimization algorithm for specific coverage area geometries has been derived and solved through linear programming, highlighting the difficulties in achieving the synthesis due to the  $r$ -decay factor effect. Then, the design of the antenna array for maximizing the coverage area length in the specific RFID-based ETC case by employing a simple iterative method has been described. A  $4 \times 4$  planar antenna array for UHF EPC Gen2 standard has been manufactured and employed as reader antenna during a measurement procedure which has demonstrated the validity of the proposed methodology.

## Acknowledgements

This work was supported in part by the National Natural Science Foundation of China (Nos. 61601093, 61701082, and 61701116), in part by Sichuan Provincial Science and Technology Planning Program of China (Nos. 2016GZ0061 and 18HH0034), in part by the fundamental research funds for the Central Universities (No. ZYGX2016Z011), and in part by Science and Technology on Electronic Information Control Laboratory.

## Conflict of interest

The authors declare that there is no conflict of interests regarding the publication of this chapter.

## Author details

Daniele Inserra\* and Guangjun Wen  
School of Information and Communication Engineering, University of Electronic Science and Technology of China, Chengdu, China

\*Address all correspondence to: [inserradaniele@uestc.edu.cn](mailto:inserradaniele@uestc.edu.cn)

## IntechOpen

© 2018 The Author(s). Licensee IntechOpen. This chapter is distributed under the terms of the Creative Commons Attribution License (<http://creativecommons.org/licenses/by/3.0>), which permits unrestricted use, distribution, and reproduction in any medium, provided the original work is properly cited. 

## References

- [1] Kummer WH. Basic array theory. *Proceedings of IEEE*. 1992;**80**(1): 127-140. DOI: 10.1109/5.119572
- [2] Balanis CA. *Antenna Theory: Analysis and Design*. 3rd ed. Hoboken: John Wiley & Sons, Inc.; 2005. 1117 p
- [3] Bevelacqua PJ, Balanis CA. Minimum sidelobe level for linear array. *IEEE Transactions on Antennas and Propagation*. 2007;**55**(12):3442-3449. DOI: 10.1109/TAP.2007.910490
- [4] Fuchs B. Shaped beam synthesis of arbitrary arrays via linear programming. *IEEE Antennas Wireless Propagation Letters*. 2010;**9**:481-484. DOI: 10.1109/LAWP.2010.2051210
- [5] Lebret H, Boyd S. Antenna array pattern synthesis via convex optimization. *IEEE Transactions on Signal Processing*. 1997;**45**(3):526-532. DOI: 10.1109/78.558465
- [6] Marcano D, Duran F. Synthesis of antenna arrays using genetic algorithms. *IEEE Antennas Propagation Magazine*. 2000;**42**(3):12-20. DOI: 10.1109/74.848944
- [7] Bevelacqua PJ, Balanis CA. Optimizing antenna array geometry for interference suppression. *IEEE Transactions on Antennas and Propagation*. 2007;**55**(3):637-641. DOI: 10.1109/TAP.2007.891509
- [8] Semenov B. Effective iterative methods for contoured beams reflector antenna synthesis. In: *Proceeding of the IEEE 39th European Microwave Conference (EuMC 2009)*; 29 September-1 October. Vol. 2009. Rome, Italy: IEEE; 2009. pp. 1500-1503. DOI: 10.23919/EUMC.2009.5296389
- [9] Chou HT, Hsaio YT, Pathak P, Nepa P, Janpugdee P. A fast DFT planar array synthesis tool for generating contoured beams. *IEEE Antennas Wireless Propagation Letters*. 2004;**3**: 287-290. DOI: 10.1109/LAWP.2004.837504
- [10] Chou HT. An efficient successive projection method for the synthesis of phased array antennas to radiate contoured field patterns. In: *Proceedings of IEEE International Conference on Wireless Information Technology and Systems (ICWITS 2012)*; 11-16 November 2012; Maui, HI, USA: IEEE; 2012. pp. 1-4. DOI: 10.1109/ICWITS.2012.6417699
- [11] Poulton GT. Power pattern synthesis using the method of successive projections. In: *Proceeding of IEEE Antennas and Propagation Society International Symposium (AP-S)*; 8-13 June 1986; Philadelphia, PA, USA: IEEE; 1986. pp. 667-670. DOI: 10.1109/APS.1986.1149679
- [12] Han Y, Wan C, Sheng W, Tian B, Yang H. Array synthesis using weighted alternating projection and proximal splitting. *IEEE Antennas Wireless Propagation Letters*. 2015;**14**:1005-1009. DOI: 10.1109/LAWP.2015.2389804
- [13] Shieh WY, Lee WH, Tung SL, Ho CD. A novel architecture for multilane-free-flow electronic-toll-collection systems in the millimeter-wave range. *IEEE Transactions on Intelligent Transportation Systems*. 2005;**6**(6): 294-301. DOI: 10.1109/TITS.2005.853708
- [14] Inserra D, Wen G. Communication area synthesis for next generation highway ETC systems. In: *Proceeding of IEEE International Conference on Communications in China (ICCC '16)*; 27-29 July 2016; Chengdu, China: IEEE; 2016. pp. 1-6. DOI: 10.1109/ICCCChina.2016.7636820

- [15] Inserra D, Wen G, Hu W. Linear optimization of antenna array for radiation pattern defined on a planar surface. *Journal of Electromagnetic Waves and Applications*. 2018. DOI: 10.1080/09205071.2018.1488624
- [16] Inserra D, Hu W, Wen G. Antenna array synthesis for RFID-based electronic toll collection. *IEEE Transactions on Antennas and Propagation*. 2018. DOI: 10.1109/TAP.2018.2851292
- [17] Inserra D, Wen G, Hu W. Planar antenna array design considerations for RFID electronic toll collection systems. In: *Proceeding of IEEE MTT-S International Wireless Symposium (IWS '16)*; 14–15 March 2016; Shanghai, China: IEEE; 2016. pp. 1-4. DOI: 10.1109/IEEE-IWS.2016.7585452
- [18] Bevelacqua P. Antenna arrays: Performance limits and geometry optimization [Ph.D thesis]. Arizona State University; 2008
- [19] Carver K, Mink J. Microstrip antenna technology. *IEEE Transactions on Antennas and Propagation*. 1981; **29**(1):2-24. DOI: 10.1109/TAP.1981.1142523
- [20] MATLAB, version 7.10.0 (R2010a). Natick, Massachusetts: The MathWorks Inc.; 2010
- [21] Rappaport TS. *Wireless Communications: Principles and Practice*. United States: Prentice Hall; 1996
- [22] Finkenzeller K. *RFID Handbook*. 3rd ed. Chichester: Wiley; 2010. 462 p
- [23] Cidronali A, Maddio S, Passafiume M, Manes G. Car talk: Technologies for vehicle-to-roadside communications. *IEEE Microwave Magazine*. 2016;**17**(11): 40-60. DOI: 10.1109/MMM.2016.2600949
- [24] EPCglobal Std. *EPC Radio Frequency Identify Protocols Class-1 Generation-2 UHF RFID, Protocol for Communications at 860–960 MHz*. Rev. version 1.1.0. 2005
- [25] Impinj Monza R6-P tag chip datasheet. [Internet]. Available from: <https://www.impinj.com/platform/endpoints/monza-r6/>
- [26] Impinj Indy R2000 UHF Gen2 RFID reader chip datasheet. [Internet]. Available from: <https://www.impinj.com/platform/connectivity/indy-r2000/>
- [27] Inserra D, Hu W, Wen G. Design of a microstrip series power divider for sequentially rotated non uniform antenna array. *International Journal of Antennas and Propagation*. 2017. DOI: 9482979. 8 p. DOI: 10.1155/2017.9482979
- [28] Impinj Speedway R420 RFID reader datasheet. [Internet]. Available from: <https://www.impinj.com/platform/connectivity/speedway-r420/>
- [29] Colella R, Catarinucci L, Coppola P, Tarricone L. Measurement platform for electromagnetic characterization and performance evaluation of UHF RFID tags. *IEEE Transactions on Instrumentations and Measurement*. 2016;**65**(4):905-914. DOI: 10.1109/TIM.2016.2516322

# Design and Optimization of Photonics-Based Beamforming Networks for Ultra-Wide mmWave-Band Antenna Arrays

*Mikhail E. Belkin, Dmitriy Fofanov, Vladislav Golovin, Yuriy Tyschuk and Alexander S. Sigov*

## Abstract

In this chapter, we review the worldwide progress referred to designing optical beamforming networks intended to the next-generation ultra-wideband millimeter-wave phased array antennas for incoming fifth-generation wireless systems, which in recent years is under the close attention of worldwide communication community. Following the tendency, we study in detail the design concepts below true-time-delay photonics beamforming networks based on switchable or continuously tunable control. Guided by them, we highlight our NI AWRDE CAD-based simulation experiments in the frequency range of 57–76 GHz on design of two 16-channel photonics beamforming networks using true-time-delay approach. In the first scheme of the known configuration, each channel includes laser, optical modulator, and 5-bit binary switchable chain of optical delay lines. The second scheme has an optimized configuration based on only 3-bit binary switchable chain of optical delay lines in each channel, all of which are driven by four lasers with wavelength division multiplexing and a common optical modulator. In the result, the novel structural and cost-efficient configuration of microwave-photonics beamforming network combining wavelength division multiplexing and true-time-delay techniques is proposed and investigated.

**Keywords:** ultra-wideband millimeter-wave antenna array, computer aided design and optimization, photonics-based beamforming network

## 1. Introduction

Generally, antenna unit is a requisite of any on-air radio frequency (RF) system forming its service area and bandwidth capability. At present, implementing an active phased array antenna (PAA) [1] results in remarkably increased footprint and operation flexibility thanks to electronic beam steering function, which is realized by a beamforming network (BFN). The concept of electronically beam-steered PAA was proposed for radar application more than 50 years ago [2]; and due to the limited requirements for the bandwidth, up to the first decade of this century, microwave diode- or ferrite-based phase shifters were widely used in BFN as control elements. In the course of further development of radar technology, new requirements that

arose referred to the increase in the area of PAA and the sector of beam scanning, also to the expansion of operating frequency range and instantaneous bandwidth [3]. To meet all of them in BFN based on standard phase-shifter approach, a serious barrier has arisen associated with the so-called beam squint effect, which leads to beam expansion and deflection from its intended target [1]. The search for solution of the limited instantaneous bandwidth issue led to the conclusion that the most effective way for radars, both pulsed and continuous probing, is to replace phase shifters in the PAA feed network with time-delay units, which will operate as true time delay (TTD) negating the effect of the finite fill time of PAA aperture [2].

Conceptually, the operation principles of microwave phase-shifter and TTD units are similar, since the both has to adjust a large number of antenna elements to force the electromagnetic wave to add up at a particular angle to the PAA regulating such uniquely related parameters, as phase and time delay. However, in the first case, steering is provided by changing transmission phase angle (phase of  $S_{21}$ ) of a two-port network, but in the second one, by changing the length of the set of the passive microwave delay lines controlled by pin-diode or transistor switching circuits. So when implemented in the form of microstrip or coplanar microwave lines, it is possible to provide a bandwidth of up to tens of GHz. The main disadvantages of microwave TTD-based BFN are cumbersomeness and large insertion loss, the value of which can vary significantly at each step of the delay. Other shortcoming of microwave implementation of TTD BFN includes crosstalk due to leakage in the microwave switches that results in reflections and irregularities of transmission characteristics.

The progress of radar technique at the beginning of the current century has led to the emergence and development of ultra-wideband radar systems. The typical examples are radars with low probability of interception of signals in which the carrier frequency of signals is rapidly reconstructed during operation in wide ranges, or radars using ultra-wideband probing signals allowing to receive an image of the object in the microwave range and distinguish close targets [4]. In addition, a number of radio electronic systems operating in different frequency bands are installed and simultaneously function on mobile carriers, in particular, the marine ones. In such systems, the application of TTD-based BFN was the only solution, which induced the numerous researches aimed to eliminating the drawbacks noted above. One example of advanced microwave beamforming schemes became so-called Rotman lens that is compact in size and provides true time delay [2]. However, this concept suffers from various additional losses, the main mechanism among which is beam-angle-dependent scanning loss that could reduce significantly the level of the main lobe of the PAA radiation pattern. Another intriguing concept, which is widely utilizing in the modern receiving PAA, is a processing at an intermediate frequency using a digital BFN [4]. Nevertheless, in the transmission PAA, where the delay is usually introduced into the microwave path, the issue of using the digital BFN is still open.

When creating such systems, combining the demands for various components of complex radar systems and ensuring the effective implementation of the required characteristics allow the use of approaches based on microwave photonics (MWP) technologies [5, 6]. At present, for incoming communication networks of fifth generation (5G), an extremely broad instantaneous bandwidth is required too, that is why ultra-wideband phase shifting or true-time-delay techniques must be used. In addition, enlarging the operating frequency of wireless fronthaul in the millimeter range is the mainstream research topic for 5G [7], which will be addressed in detail separately. On this way, MWP approach is extremely attractive for realizing multi-function PAA's optical BFN due to its superior instantaneous operating bandwidth, immunity to electromagnetic interference, lightweight, and reconfigurability [8].

Recently, we compared by NI AWRDE-based simulation, the three versions of photonics BFN arrangements using optical phase shifters, switchable optical delay lines, and the proposed arrangement based on a combination of multichannel

fiber Bragg grating and switchable optical delay lines [9]. Continuing work of the direction, in this chapter, we review the worldwide progress referred to designing photonics-based BFN and highlight our last simulation results on design search of optimized photonics BFNs for next-generation ultra-wide millimeter-wave (mmWave) antenna arrays. In particular, Section 2 reviews the specialties of microwave and mmWave photonics technique in 5G wireless networks of radio-over-fiber (RoF) architecture. In addition, Section 3 presents theoretical background of array antenna beam steering using ideal models of phase shifters and TTD delay lines. There is a short analysis of updated photonics beamforming networks produced on optical fibers, Bragg gratings, or photonics integrated circuits (PIC) in Section 4. The principles and ways to optimize photonics BFN design is discussed in Section 5 based on the known photonics BFN scheme including set of optical delay lines and a novel structural and cost-efficient configuration that, following the results of the previous sections, consists of microwave photonics BFN using wavelength division multiplexing and TTD techniques. All schemes are modeled by NI AWRDE CAD tool. Finally, Section 6 concludes the chapter.

## 2. Microwave and millimeter-wave photonics technique in 5G wireless networks of RoF architecture

The next-generation wireless communications network (usually named as 5G) promises to deliver unprecedented data volumes and services for the mobile and fixed users representing both an evolution and a revolution of mobile technologies [10–13]. Some of these technologies are mainly architectural in nature—for example, moving some of the decision-making to the devices themselves (device-centric architectures and smart devices)—while others are more hardware oriented. The increasing demands for broadband services and the transmission of higher data rates have led to consideration of wireless links operating at higher carrier frequencies and extending well into the mmWave-band where total capacity of the single cell can approach some gigabits per second. **Table 1** lists three interconnected engineering challenges facing 5G [10, 14]. The first one is ultradensification of service areas and users. In the result, femtocell radio-over-fiber (RoF) architecture is proposed [15]. The second one includes utilization of mmWave spectrum [7]. Following it, microwave photonics-based circuit design comes to the forefront. At last, the third one is mobile data traffic explosion. In the result, 1000-fold factor over present-day systems must be reached.

As follows from the table, the ambitious goal to increase explosively mobile traffic is able to achieve by solving two global tasks: architectural referred to RoF and technological referred to MWP. Combining millimeter-wave band and RoF network architecture is one of the promising candidates to deliver intensive bitrate traffic with seamless convergence between optical backhaul and wireless fronthaul. In addition, RoF technique allows converting directly a lightwave spectrum to mmWave radio spectrum using a simple MWP-based up-conversion scheme [16], which is important to keep the remote cells flexible, cost effective, and power

No	Feature	Result
1	Ultra densification	Femtocell RoF architecture
2	Utilization of mmWave spectrum	Microwave photonics-based circuit design comes to the forefront
3	Mobile data traffic explosion	1000-fold factor over present-day systems

**Table 1.**  
*The key engineering challenges facing 5G.*

efficient. **Figure 1** demonstrates an example of mmWave RoF architecture, which consists of central office (CO), a remote or base station (RS) and wireless subscriber terminals (ST). CO is interactively connected with RS through fiber-optic cable, and RS is interactively connected with ST through wireless link. A typical position of RS is in the center of the service area; that is, for omnidirectional covering, four PAAs with an azimuth of  $90^\circ$  would be an optimal decision.

As shown in a large number of studies [7, 17, 18], mmWave 5G wireless network infrastructure must be erected with a lot of small cell sites controlled by the corresponding RS. In order to avoid inter-interference in these cells, one of the promising approaches is to equip the RS with a beam-steerable PAA (as in **Figure 1**), as has been practiced in radars for many years (see section “Introduction”). According to the estimates, mmWave RS would use PAA with hundreds of antenna elements to form directional beams for transmission and to receive similar beams from adjacent STs and RSs.

To implement effective radio communication within these cells, a number of leading countries have already developed a promising spectrum including mmWave-bands up to 100 GHz. **Figure 2** exemplifies USA assignment ranged from 27.5 to 95 GHz [19]. As follows from the figure, there is a continuous operating band between 57 and 76 GHz (fractional bandwidth of 30%), which will be used by us in the following treatment.

The final topic to be highlighted in this section is to design 5G RS’s equipment using microwave and mmWave photonics techniques. Microwave photonics is an interdisciplinary scientific and technological field that combines the domains of microwave engineering and photonics. This field in the last 30 years has attracted immense interest and generated many new R&Ds from both the scientific community and the commercial sector. Emerging applications for 5G networks of RoF architecture indicate that MWP is set to be a subject of increasing importance ([8, 20, 21], and refs. cited there). By common opinion, MWP technology opens the way to super-wide bandwidth transmitting characteristics at lower size, weight, and power as compared with traditional electronic approach [22]. As an example, in a typical arrangement of MWP-based microwave transmitting unit (**Figure 3**), a photonics circuit is inserted between two microwave electronic chains typically including digital-analog converter (DAC), intermediate frequency and power amplifiers (IFA and PA, respectively), and antenna. For forward and reverse transformations of microwave and optical signals, there are two interfacing units at their bounds: electrical-to-optical (E/O) and optical-to-electrical (O/E) converters. Between the interfaces, there are various photonics processing units for frequency up-conversion, filtering, time delaying, beamforming, and so on, of microwave signals in optical domain.

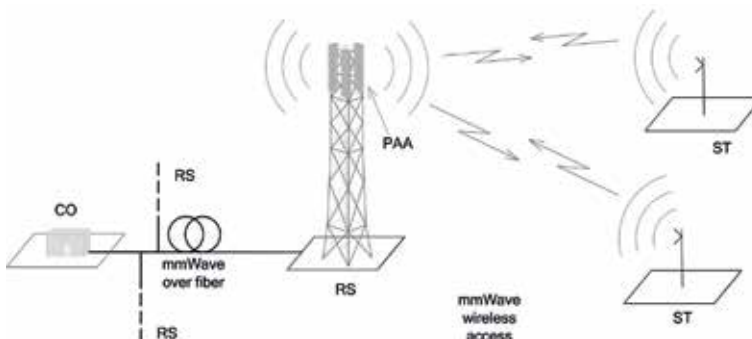


**Figure 1.**  
An example of mmWave RoF architecture.



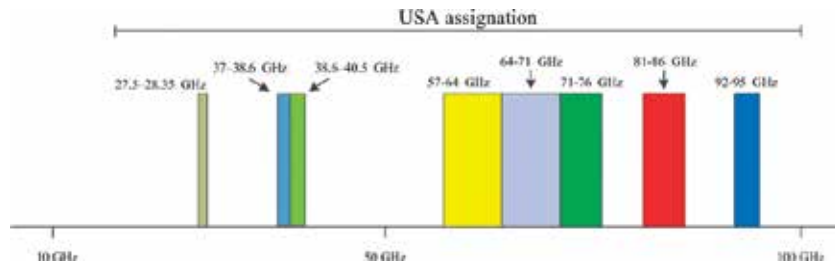


**Figure 2.**  
 5G mmWave spectrum allocation of USA assignment.

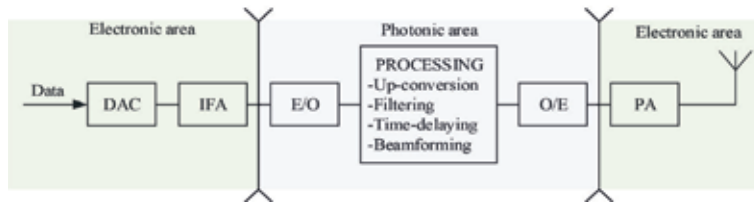


**Figure 3.**  
 A typical arrangement of MWP-based microwave transmitting unit.

*The outcome.* The source data for posterior calculations of PAA are:

- the operating band is 57–76 GHz (see **Figure 2**)
- the maximum azimuth steering of the main lobe deviation is  $\pm 45^\circ$  (see **Figure 1**)

### 3. Theoretical background of array antenna beam steering

As noted in the Introduction, phased array antennas are now widely used in radar equipment due to the possibility of fast electron beam scanning and increased failure-resistant feature compared to continuous aperture antennas and mechanical scanning. The application of PAAs in radar allows achieving high speed of viewing the service area and tracking high-speed maneuvering objects [1]. Besides, PAAs ensure the operability of the radar system in a complicated interference situation due to the adaptive formation of a complex-shape radiation pattern [4]. In many cases, the use of array antenna let reduce the weight of the radar system and lower its total cost. In addition to radar, mmWave array antennas capable of operating in ultra-wide frequency range are considered as one of a key enabling technology for designing RS of 5G network, as noted in the previous section. There, a formation of a narrow steered beam by means of the antenna array makes it possible to increase the directive gain to compensate for the attenuation in the mmWave-band. Besides, the use of a narrow beam would reduce the interference effects from other closely spaced transmitters, and also provide the possibility of spatial multiplexing to increase throughput while simultaneously exchanging information with several STs.

As described above, electronic scanning in the PAA is provided by a beamforming network, which includes phase shifters, or delay lines. The BFN supports a continuous or discrete beam movement in space due to phase control or signal time delay between the array elements. Below, a short theoretical study using ideal models will be presented pursuing the goal to define the complementary input data for the posterior design of the specific photonics-based BFNs for the ultra-wide mmWave-band PAA exploiting widespread microwave-electronic computer-aided design (CAD) environment NI AWRDE.

In general, the array antenna is a collection of antenna elements connected to the transmitter/receiver through RF feeds, which includes a BFN. A typical arrangement of antenna elements is shown in **Figure 4**.

The radiation pattern of an array of identical antenna elements (Eq. (1)) is the product of the diagram of an individual element  $f(\theta, \varphi)$  and the array factor  $F(\theta, \varphi)$ , depending on the mutual arrangement of the elements

$$D(\theta, \varphi) = f(\theta, \varphi) * F(\theta, \varphi), \quad (1)$$

where  $\theta$  is an elevation angle,  $\varphi$  is an azimuth.

The array factor has the form:

$$F(\theta, \varphi) = \sum a_i \exp(-jk \mathbf{r}_i \cdot \mathbf{r}), \quad (2)$$

where  $a_i$  is the transmission gain (weight) in the channel of the feed network connected to the  $i$ -th element,  $\mathbf{r}_i$  is the radius vector of the  $i$ -th element,  $\mathbf{r}$  is the radius-vector specifying the direction  $(\theta, \varphi)$ ,  $k$  is the wave number, referred to the operation wavelength  $\lambda$  as  $k=2\pi/\lambda$ .

When analyzing various configurations of antenna arrays and feed networks, only specific variant of the array factor is often considered, assuming the antenna elements to be isotropic, with the radiation pattern  $f(\theta, \varphi)=\text{const}$ . In the process of the examination, the following basic parameters are analyzed: antenna directivity, mainlobe's half power or null-to-null beamwidth, beam-direction angular error, and maximum sidelobe level [1]. Radiation patterns are usually represented for the azimuth  $\varphi$  and elevation  $\theta$  sections in a Cartesian or polar coordinate system, or in 3D form.

As mentioned above, for scanning PAAs, there are two main ways of designing the feed networks: based on phase shifters and delay lines. Mathematically, the difference between these techniques can be represented as follows. First, expanding  $k$  and multiplying radius-vectors  $\mathbf{r}_i \cdot \mathbf{r}$ , Eq. (2) can be rewritten as

$$F(\theta, \varphi) = \sum a_i \exp(-j\frac{\omega}{c} \mathbf{r}_i \cdot \mathbf{r}) = \sum a_i \exp(-j\omega \tau_i), \quad (3)$$

where  $\omega$  is the angular operating frequency and  $\tau_i$  is the time delay that must be introduced into the channel of the feed network connected to the  $i$ -th element to obtain the required array factor. For the narrow-band case with a central operating frequency  $\omega_0$ , Eq. (3) takes the forms

$$F(\theta, \varphi) = \sum a_i \exp(-j\omega_0 \tau_i) = \sum a_i \exp(-j\Phi_i), \quad (4)$$

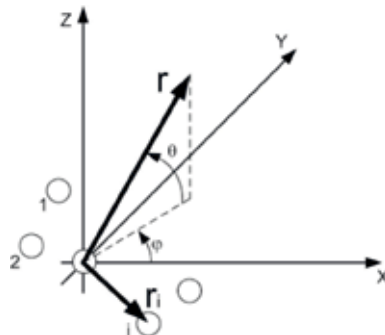


**Figure 4.**  
Array antenna of arbitrary geometry.

where  $\phi_i$  is the phase shift, which must be introduced into the channel of the feed network connected to the  $i$ -th element, to obtain the required array factor. Obviously, if the frequency deviates from  $\omega_0$ , the phase shifts in the channels of the feed network will not provide the required  $F(\theta, \phi)$ . This phenomenon called “beam squint” leads to an error in the direction of the maximum of the PAA pattern, and also to a certain increase in the level of the sidelobes. Nevertheless, despite the beam squint, the BFN based on phase shifter due to the ease of implementation has become widespread in narrowband PAAs, i.e., with a fractional bandwidth, commonly not exceeding 10%, depending on the criterion used [23].

In addition, the important parameters of the PAA are the directive gain and the beamwidth closely related to it. In the simplest case of a linear equidistant array, the full width at half-maximum (FWHM) of the beam,  $\Delta_{0,5}$ , is inversely proportional to the aperture length  $L$  and in the antenna, broadside is determined in radians according to:

$$\Delta_{0,5} = 0.886 \lambda/L \quad (5)$$

For an array of  $N$  elements with the distance between them of  $\lambda/2$ , which is often used in practice and will be considered below, Eq. (5) can be reduced to a form convenient for calculating the beamwidth in degrees:

$$\Delta_{0,5} = 101.5/N \quad (6)$$

It should be noted that the beamwidth increases with the deviation from the PAA broadside direction. For this reason, the variants of the antenna array construction are often compared along the beamwidth in the direction of the normal, taking into account the broadening effect at large deviation angles.

The directive gain, which is also considered in the direction of the broadside, and for the array of  $N$  elements, the distance, between which is equal to  $\lambda/2$ , is determined according to:

$$D = 2 * N, \quad (7)$$

where the factor of 2 is caused by the presence of the conducting plane in the majority of PAAs, which guides (reflects) the entire radiation flux into one half-space. In the absence of such a plane, the gain is reduced accordingly.

In the mmWave-band, it is sometimes not possible to arrange array elements at the intervals of  $\lambda_{min}/2$ , where  $\lambda_{min}$  is the minimum wavelength corresponding to the upper operating frequency. When the interval between elements in the radiation pattern increases, the grating lobes limiting the range of scanning angles might arise. Mathematically, this effect is due to the periodicity of the exponent in Eq. (2). For a linear array, the condition for the occurrence of a grating lobe in the azimuth  $\varphi$  with the direction of the beam  $\varphi_0$  is:

$$kd(\sin\varphi - \sin\varphi_0) = m * 2\pi, \quad (8)$$

where  $d$  is the distance between antenna elements, and  $m$  is an integer. It can be shown from Eq. (2) that the range of scanning angles  $\pm\varphi_{max}$  for the distance  $d$  is limited by the expression:

$$d/\lambda_{min} \leq (1 + \sin\varphi_{max})^{-1} \quad (9)$$

From Eq. (9), it follows that to ensure the absence of grating lobes when scanning in the range of  $\varphi_{max} = 90^\circ$ , the distance between antenna elements  $d$  should not exceed  $\lambda_{min}/2$ .

The phase shifters or delay lines used in BFNs can be steered continuously or in discrete steps. Because of the operation convenience, the later type is most widely exploited. Such BFNs are usually controlled by binary codes and are steered in the range from 0 to  $(2^R - 1) * \delta$ , where  $\delta$  is the sampling period (SP) that determines the error of the BFN operation due to discrete time sampling;  $R$  is the number of bits of the binary phase shifter or delay line. For phase shifters, the parameter  $R$  is selected in such a way as to cover the phase shift range of  $360^\circ$  with a step  $\delta$ . For delay lines, the number of bits must provide the necessary time-delay setting  $\tau_{max}$  for deviating the PAA diagram by the maximum operating angle. For a given number of bits  $R$ , the SP is determined by:

$$\delta \geq \tau_{max} / (2^R - 1) \tag{10}$$

The sampling error within  $\pm\delta/2$  affects primarily the direction and level of the sidelobes. For a PAA with a small number of elements, there is a primary error in the position of the beam. On the contrary, for large PAAs, the sampling error does not affect the position of the beam, since it has an average value of 0. Reducing the directivity for large PAAs due to the error of phase quantization and amplitude errors in the channels of the feed network might be described statistically in the form:

$$D = D_0 / (1 + \sigma_\Phi^2 + \sigma_A^2), \tag{11}$$

where  $D_0$  is the directivity without taking into account the quantization error,  $\sigma_\Phi^2$ ,  $\sigma_A^2$  are the variances of the phase quantization error or the amplitude error, respectively. Thereafter, the average level of the sidelobes might increase in more than  $(\sigma_\Phi^2 + \sigma_A^2)$  times. It should be noted that the sidelobe closest to the main beam has the maximum level. Its level is determined by the distribution of the transmission gain  $a_i$  in the channels of the feed network, and for uniform distribution is  $-13$  dB relative to the main beam level.

The influence of the PAA's parameters considered above was examined for the example of a linear equidistant array of 16 isotropic elements (**Figure 5**) designed for operation at the frequency range of 57–76 GHz. To ensure scanning without grating lobes, the distance between the elements of 2 mm was selected in accordance with Eq. (9), starting from the minimum wavelength of 4 mm. This distance leads to beamwidth of  $6.3^\circ$  at highest frequency and antenna gain of 15 dB in accordance with Eqs. (6) and (7), respectively.

The beam FWHM of the PAA under test varies in accordance with Eq. (5) from  $8.4^\circ$  at 57 GHz to  $6.3^\circ$  at 76 GHz. The necessity of transmitting an ultra-wideband signal with a fractional bandwidth of up to 30% by means of this PAA will inevitably lead to significant distortion of the normalized radiation pattern (NRP) shape when using a phase-shifter based BFN. We will illustrate this with the example of a signal with a 19 GHz bandwidth and a central frequency of 66.5 GHz, for which phase shifts for a beam direction of  $30^\circ$  are calculated according to Eq. (4). The NRPs formed by the BFN with ideal phase shifters at 57, 66.5, and 76 GHz are shown in **Figure 6**. It can be seen from the figure that the deviation of the maximum of the NRP from the desired direction is  $4-6^\circ$  when the frequency is varied within the operating range.

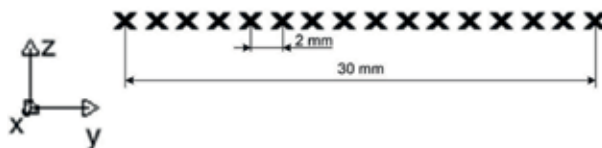


**Figure 5.**  
Configuration of the PAA under test.

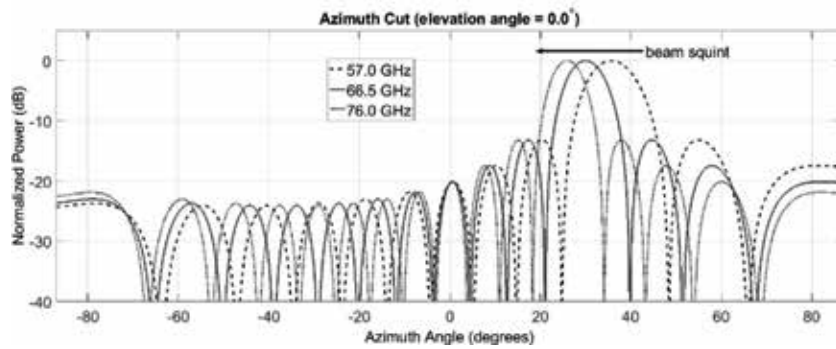


**Figure 6.** Normalized radiation patterns formed by the BFN with ideal phase shifters at 57, 66.5, and 76 GHz in the case of transmitting a signal with a 30% fractional bandwidth.

Moreover, at the edges of the frequency band, the power radiated by the PAA in the given direction falls by 4 dB. Because of the squint effect, the different frequency components of the signal will be radiated in different directions. As the result, a receiver would experience a decrease in amplitude at the edges of the RF signal frequency spectrum up to 4 dB, which causes a distortion of the waveform and the occurrence of reception errors. Signal components emitted in undesired directions also might cause interference in the receivers, for which this signal was not intended. For comparison, **Figure 7** shows the NRPs formed by the BFN with delay lines at the same frequencies. It is seen from the figure that the squint phenomenon is completely absent in the entire frequency range. This well-known benefit ensures the superiority of the use of TTD-steered BFNs in PAAs with a relative bandwidth of more than 10% [23], in spite of the fact that TTD solution in principle is more expensive, bulky, and technically complex than the BFN on phase shifters. Thus, for the BFN under consideration, TTD-steered technique is the only suitable solution that ensures operability in the frequency range from 57 to 76 GHz.

Essential schematic simplification can be achieved if binary switchable delay lines (BSDL) are used instead of continuously tuned ones. To determine the parameters of such a BSDL providing scanning angle of  $\pm 45^\circ$ , the maximum time delay calculated in accordance with Eq. (3) is 70.8 ps. Following Eq. (10), the use of 4, 5 and 6-bit BFNs makes it possible to obtain a sampling period of 4.7, 2.3, and 1.1 ps, respectively. The growth of SP leads to a corresponding increase of the variance for the phase quantization error, which contributes to distortions and directivity decay described by Eq. (11).

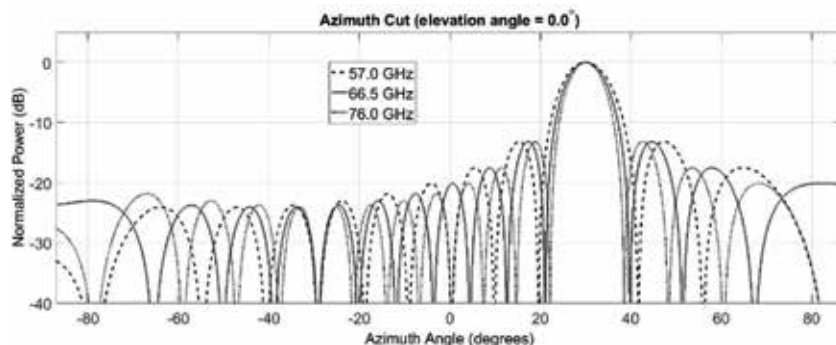


**Figure 7.** Normalized radiation patterns formed by the BFN with ideal delay lines at 57, 66.5, and 76 GHz in the case of transmitting a signal with a 30% fractional bandwidth.

Number of bits	SP (ps)	Relative peak SLL (dB)	Relative average SLL (dB)
4	4.7	-3.3	-5.2
5	2.3	-8.1	-10.9
6	1.1	-10.7	-12.4

**Table 2.**  
FoMs for BSDL with various number of bits.

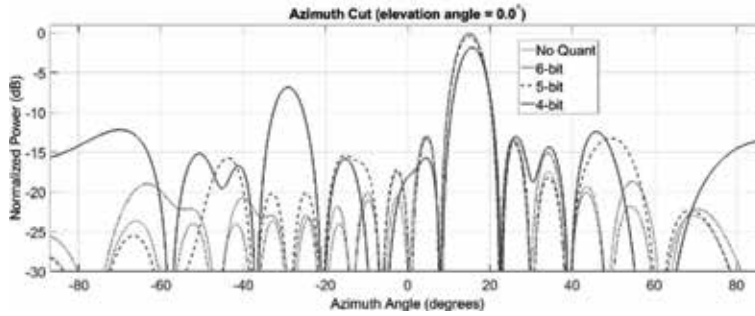


**Figure 8.**  
Examples of radiation pattern distortion due to quantization errors.

One possible way to characterize the amount of distortion is to simulate all possible scan angles and calculate maximum sidelobe level (SLL) using the above calculated SP values [4]. Peak and average values obtained through the entire scan range can be considered as figures of merit (FoMs) that determine the performance of BSDL. **Table 2** lists the results of calculations carried out by the above technique.

**Figure 8** exemplifies the distortions for BSDLs with different number of bits, which affect NRPs in different directions of scanning range.

When using a 4-bit BSDL, a sharp increase in the level of the sidelobes, a decay in directivity, and a deviation of the beam position from the desired one are observed. However, it is acceptable to use a 5-bit BSDL with a sampling period of 2.3 ps, for this case.

To summarize, the following outcomes could be concluded:

1. The use of phase shifters in ultra-wideband antenna array leads to beam squint phenomenon; so only TTD-based BFN is suitable in such case.
2. Minimum interelement distance for an array that is operable at the frequency range of 57–76 GHz without grating lobes is 2 mm.
3. The maximum time delay required to ensure scanning range of  $\pm 45^\circ$  is 70.8 ps for the array under consideration and 5-bit BSDL is feasible to simplify TTD-based BFN construction. They provide a sampling period of 2.3 ps and a relative average sidelobe level of  $-10.9$  dB over the entire scanning range (see **Table 2**).

#### 4. Microwave photonics beamforming networks

As follows from Section 3, the optimal way to design ultra-wideband PAAs of mmWave-band is to steer the radar beam with TTD-based photonics BFN. Below, we will briefly review the current level of MWP BFN in order to select, using the data in **Table 2**, the optimal principle and scheme of its construction for efficient

No	Requirement	Result
1	Suppressing sidelobe level	Preserve the directive gain of the main beam
2	Null control	Reduce the effects of interference and jamming signals
3	Simplifying the complexity of feed network	Cost and power efficiency
4	Reducing the mutual coupling between BFN elements	Enlarge the PAA's figures of merit

**Table 3.**  
 Primary requirements to optical TTD-based microwave photonics BFNs.

No	Time-delay unit	Scheme	Bandwidth	Steering method, settling time	Delay range	Source
1	Silicon waveguide	Binary, 2 × 2 switches, MZM	8–12 GHz	Discrete <1 μs	Up to 2.5 ns	[24]
2	Linearly chirped fiber Bragg grating	TLS and separate pump laser	56 GHz	Continuously, optical pump power	200 ps	[25]
3	Dispersive fiber prism	TLS with MUX	4–8 GHz	Continuously, hopping 1 ns	—	[26]
4	Dispersive photonics crystal fibers	TLS, four fiber channels, MZM	8–12 GHz	Continuously	±31 ps	[27]
5	Match in length fibers, 5 bit	Spatial light modulators	6–18 GHz	Polarization switched, 20 ms	6–178.4 ps	[28]
6	Dispersion compensation fiber	TLS, 8 channels, MZM	8–12 GHz	Continuously	±43.3 ps	[29]
7	Holographic grating	8 × 8 2D delay matrix	18–26.5 GHz	Switchable, binary, 6-bit	443.3 ps	[30]
8	Integrated ring resonators	TLS, binary tree, 1 × 8, MZM	2.5 GHz	Continuously, thermo-optical	1200 ps	[31]
9	FBG prism and fiber-optic delay lines matrix	2D, 2 × 2 switches	Narrow-band 1GHz	Switchable, sampling period 120 ps	±200 ps 360 ps	[32]
10	Integrated waveguide	Binary with 2 × 2 switches, MZM	Narrow-band, 42.7GHz	Switchable, 4 bit, 20 ns	15.7 ps	[33]
11	Integrated ring resonator-based delay lines	Binary with 2 × 2 switches, MZM	3–7 GHz	Switchable, few nanoseconds	34 ps	[33]

No	Time-delay unit	Scheme	Bandwidth	Steering method, settling time	Delay range	Source
12	TLS, integrated ring resonators	Phase modulation	3–7 GHz	Continuously	300 ps	[34]
13	Dispersion compensation fiber	TLS	5.9–17 GHz	Continuously	±200 ps	[35]
14	Linearly chirped fiber Bragg grating	Wavelength-dependent recirculating loop	11.2 GHz	Continuously	2500 ps	[36]
15	Integrated ring resonators	Binary tree, MZM	2.05 GHz	Switchable, 1 ms	630 ps	[37]

**Table 4.**  
*Examples of TTD-based photonics BFNs.*

application in RSs of incoming RoF-based 5G networks. **Table 3** lists the primary requirements to a TTD-based MWP BFN from the point of view of a hardware developer for PAA.

To meet the requirements of **Table 3**, a TTD-based photonics BFN should have enough bandwidth and delay range and support small level of settling time and crosstalk. Besides, it must be either continuously tunable or switchable with a sufficiently small sampling period. At present, many implementations of TTD-based photonics BFNs exist for PAA application. Such devices are often based on a set of fiber or integrated delay lines, ring resonators, spatial light modulators, semiconductor optical amplifiers, dispersive fibers, and so on. Optical channel is usually formed based on single-carrier technique using untunable laser or on multicarrier one with wavelength division multiplexing (WDM) using tunable laser source (TLS) and spectral multiplexer (MUX). RF-to-optical conversion is advantageously realized with the help of a Mach-Zehnder intensity modulator (MZM), but other types of optical modulators are also used. For reverse optical-to-RF conversion, pin-photodiodes are exclusively utilized. **Table 4** lists the key results of our search using journal and conference contributions have been published.

As one can see from table, the developed MWP-based BFNs provide time delays from tens of picoseconds to units of nanoseconds in the bandwidth up to tens of GHz. The results being presented allow us to conclude that it is possible to meet requirements 1 and 2 of **Table 3** by using a known approach based on the concept of weighted amplitudes and phases [38]. In particular, to precisely control loss and delay time, the optical fibers of a slightly different length (example no 5) and the dispersion effect in standard single-mode (example no 3), dispersion-compensated (examples nos 6 and 13) or photonics crystal fibers (example no 4) were in use at the early stage. Later, with the development of photonics integrated technology, which ensured a significant reduction in a device footprint and simplifying the complexity of feed network (see point 3 of **Table 3**), the switchable integrated silicon waveguides (example nos. 1 and 10) or the ring microresonators (example nos 8, 11, and 15) began to be exploited. In addition, if it is necessary to ensure a continuous adjustment of the delay time, a tunable TLS (example nos 2–4, 6, 8, and 12–14) is in common use. The requirement to reduce the mutual coupling (see point 4 of **Table 3**), usually quantified as crosstalk level, occurs in common elements of



the optical channel, for example, in optical splitters or multiplexers. Its effect in photonics BFNs has been still poorly studied and will be considered in Section 5.3.

## 5. Principles and ways to photonics BFN design

In the process of design, a developer of new MWP-based RF apparatuses is facing a problem of choosing an appropriate software. As of today, the existing optical and optoelectronic CAD tools (OE-CAD) are not developed like being perfected for three decades CAD tools intended for modeling of RF circuits (E-CAD). On the contrary, operating at symbolic level modern high-power microwave E-CAD tool solves this problem enough simply and with high precision, but there are no models of specific active and passive photonics components in its library. To overcome this problem, we have proposed and validated experimentally a new approach to model a broad class of promising analog microwave radio-electronics systems based on microwave photonics technology. Guided by them, the electrical equivalent circuit models for the different types of semiconductor laser, photodetector, optical modulator, and so on were proposed and verified [39 and refs. cited there]. Using these components, a simple PAA's BFN was proposed and initially studied using NI AWRDE software [9]. Below, continuing work of the direction, we model a typical photonics BFN scheme including a set of switchable optical delay lines (see examples of Table 4), and a novel structural and cost-efficient configuration that, following the results of the previous sections, consists of microwave photonics BFN combining wavelength division multiplexing and TTD techniques.

### 5.1 The schematics for simulation

Figure 9 shows first photonics BFN schematic for comparison that is a part of 16-element PAA's feed network.

In this case, 16 unmodulated untunable lasers of different wavelengths  $\lambda_1-\lambda_{16}$  are used. Using the same RF signal, each transmission channel is converted by the

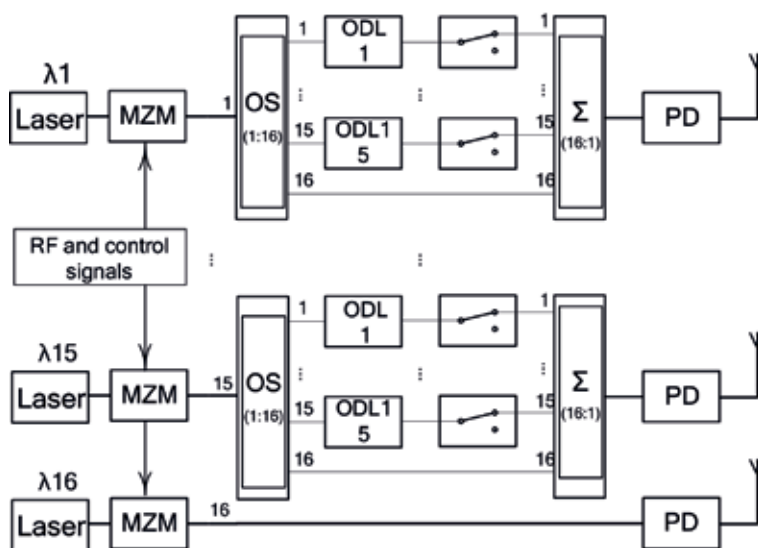


**Figure 9.**  
 16-element RF photonics BFN based on switchable optical delay lines.

corresponding Mach-Zehnder modulator (MZM) to optical range and shared into 16 branches by optical splitter (OS). Each branch consists of a switchable optical delay lines (ODL). Then, the delayed optical signals are summarized, converted into RF band by a photodiode (PD), and emitted by an ideal isotropic antenna element.

Important drawback of this scheme is the need to use a large number of lasers and MZMs (16 lasers and the same MZMs for a 16-element array), which makes it impractical due to the cumbersomeness and large energy consumption, even for such a relatively small PAA. In addition, according to the results of Section 3, each ODL must provide total delay of at least 71 ps and of digit capacity of at least 5 bits. That is, even when this BFN is implemented in the integrated version (see **Table 4**) using the waveguide material with the lowest losses [40], the difference in losses at the minimum and maximum step will be more than 30 times, which, according to Section 3, will lead to unacceptable distortions of the radiation pattern.

To overcome the above issues, **Figure 10** demonstrates an advanced photonics BFN scheme that is a part of the same 16-element PAA's feed network. In this case, only four unmodulated untunable lasers of different wavelengths  $\lambda_1-\lambda_4$  in accordance to 200 GHz ITU WDM grid are used. Laser emissions are summarized in a spectral multiplexer (MUX), modulated in the common MZM by RF signal, and, through optical circulator, are input to four-channel reflected Bragg grating (RBG). The levels of corresponding delayed signals are recovered by an optical amplifier (OA) with an optical bandpass filter (OBF) after it, and shared into 16 branches by OS. Each branch consists of a 3-bit switchable ODL unit delayed once more optical signals for 2.3, 4.6, and 9.2 ps (see results of Section 3), a spectral demultiplexer (DMUX),  $1 \times 4$  optical switch (OSW), a PD, and a PAA's antenna element. In addition, the schematic of 3-bit binary delay line is shown in **Figure 11**.

## 5.2 Models

**Figures 12, 13** demonstrate the equivalent models of the BFN schemes discussed above that are developed using the NI AWRDE microwave electronic CAD tool. The proposed scheme of **Figure 13** contains two units that can be implemented based on PICs: 3-bit optical delay line and a four-channel reflected Bragg grating module. The equivalent model of the first unit is shown in **Figure 14**. The NI AWRDE equivalent model of the second one was proposed and studied in detail elsewhere [41].

## 5.3 Simulation experiments

With the help of the developed models, a number of simulation experiments were carried out, the main task of which was to check the stability of the proposed scheme for the nonideality of the transmission characteristics of the modules and units that make up its composition in according with the primary requirements to

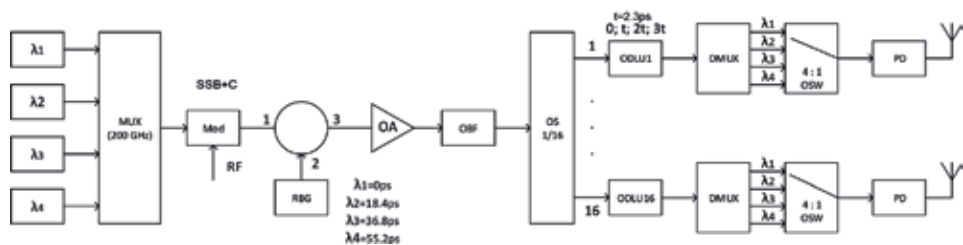


**Figure 10.** 16-element RF photonics BFN based on a combination of multichannel fiber Bragg grating and switchable optical delay lines.

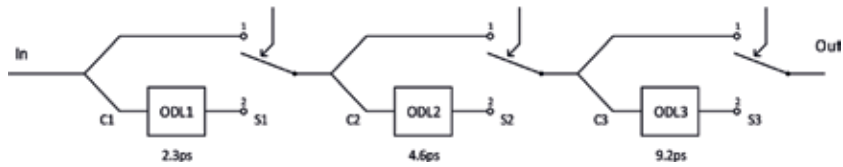


**Figure 11.**  
 The schematic of 3-bit binary delay line.

a TTD-based MWP BFN (see **Table 3**). The key parameter providing the requirements of point 4 of this table is a crosstalk interference, the permissible level of which in the TTD-based photonics BFN is still poorly studied. For example, in the scheme of **Figure 10**, there are a number of sources of crosstalk interference, including insufficient isolation of the arms of an optical circulator, an OS, and a DMUX. Experiments were carried out on the basis of specific input data received and substantiated in Sections 2 and 3. First, the known and the proposed schemes containing ideally isolated arms were modeled. A comparison of their NRPs showed

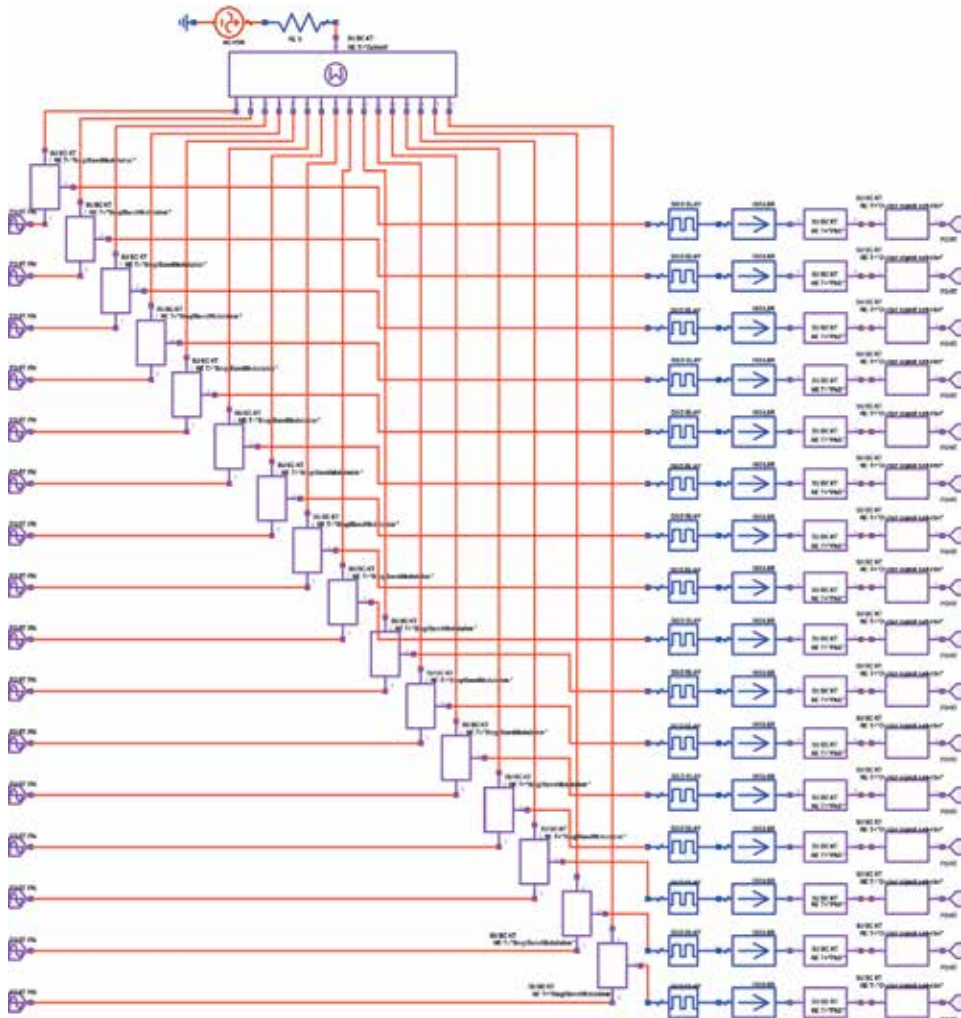


**Figure 12.**  
 N/AWRDE model of 16-element RF photonics BFN based on switchable optical delay lines.

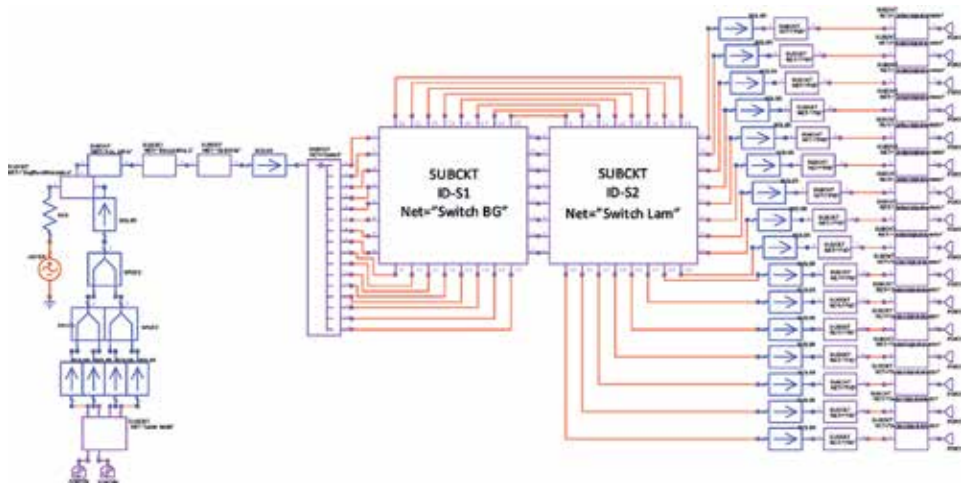


**Figure 13.**  
NI AWRDE model of 16-element RF photonics BFN combining four-channel optical source, four-channel reflected Bragg grating, and 3-bit switchable optical delay lines.

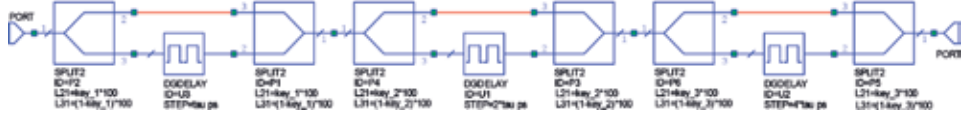


**Figure 14.**  
NI AWRDE model of 3-bit optical delay line.

their complete identity. **Figure 15** exemplifies the calculation results of NRP characteristics for the both schemes under testing at the lower, middle, and upper frequencies of the PAA's operating range for beam deflection angles of 45° (a) and 30° (b). Comparison with the results of formal calculations given in Section 3 allows us to draw a conclusion about the correctness of the developed models.

Investigation of the effect of crosstalk interference showed the overall stability of the proposed scheme. **Figure 16** exemplifies the NRPs for the case of a joint effect of crosstalk (CS) in an optical circulator and amplitude asymmetry of the levels at the output of the optical splitter (AiOS). As one can see, their effect causes a phase shift of sidelobes, which leads to an increase in their level. However, their suppression meets the standard requirements for phased arrays.

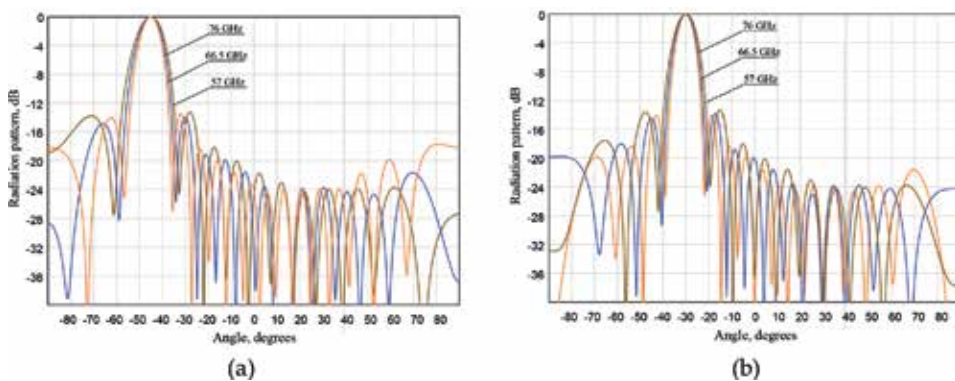


**Figure 15.**  
Normalized radiation patterns of the both TTD-steered 16-element photonics BFNs.

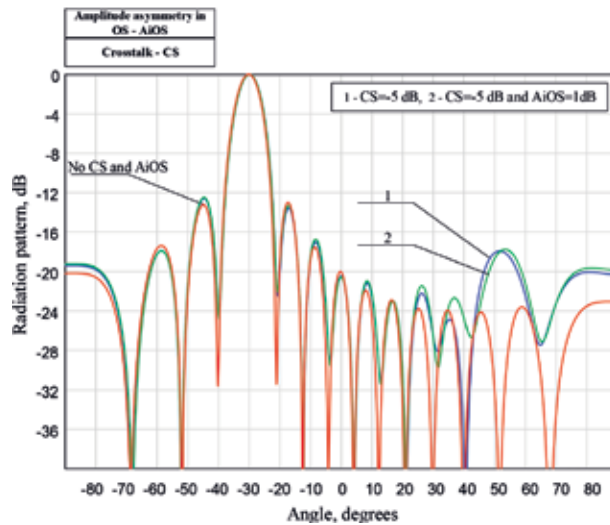


**Figure 16.** Normalized radiation patterns of 16-element BFN combining 4-channel optical source, four-channel Bragg grating, and 3-bit switchable optical delay lines.

## 6. Conclusions

In the chapter, we explored and demonstrated the availability of using the phased array antennas, which were known for a long time in the radar technique, in the incoming fifth-generation wireless communication systems. The study was carried out using a specific example of designing a photonics-steered beamforming network (BFN) of a transmitting-phased array antenna for a remote station operating in the V-band with a 30% fractional bandwidth allocated in the USA as a promising one for future 5G systems. For this goal, we first reviewed the specialties of microwave and millimeter-wave photonics technique in 5G wireless networks of radio-over-fiber architecture. Then, to determine the input data for subsequent design, a theoretical background of array antenna beam steering using ideal models of phase shifters and true-time-delay lines was presented. A brief analysis of updated optical beamforming networks produced on optical fibers, Bragg gratings or photonics integrated circuits, showed the possibility and efficiency of constructing the delay elements required for the device being developed, on the basis of photonics integrated circuits. The developed models and executed simulation of two versions of photonics BFN based on known scheme including set of optical delay lines and a novel structurally and cost-efficient configuration using wavelength division multiplexing and TTD techniques demonstrated the advantages of the proposed scheme from the point of view of the simplicity, key figures of merit, size, weight, and power features.

## Acknowledgements

This work was supported by the Russian Foundation for Basic Research, Grant No. 17-57-10002.

## Conflict of interest

The authors declare the lack of the conflict of interest.

## **Author details**

Mikhail E. Belkin<sup>1\*</sup>, Dmitriy Fofanov<sup>1</sup>, Vladislav Golovin<sup>2</sup>, Yuriy Tyschuk<sup>2</sup> and Alexander S. Sigov<sup>1</sup>

1 Moscow State Technological University (MIREA), Scientific and Technological Center “Integrated Microwave Photonics”, Moscow, Russian Federation

2 Sevastopol State University (SevSU), Sevastopol, Russian Federation

\*Address all correspondence to: belkin@mirea.ru

## **IntechOpen**

---

© 2018 The Author(s). Licensee IntechOpen. This chapter is distributed under the terms of the Creative Commons Attribution License (<http://creativecommons.org/licenses/by/3.0>), which permits unrestricted use, distribution, and reproduction in any medium, provided the original work is properly cited. 

## References

- [1] Mailloux RJ. Phased Array Antenna Handbook. Boston: Artech House; 2005. 515 p
- [2] Skolnik MI, editor. Radar Handbook. New York City: McGraw Hill Publishing; 2001. 1351 p
- [3] Bradsell P. Phased arrays in radar. Electronics & Communications Engineering Journal. 1990;2(2):45-51
- [4] Hansen RC. Phased Array Antennas. New Jersey: John Wiley & Sons Inc; 2009. 547 p
- [5] Matthews P. Practical photonic beamforming. In: Proceedings on IEEE International Topical Meeting on Microwave Photonics. 1999. pp. 271-274
- [6] Seeds AJ, Williams KJ. Microwave photonics. IEEE/OSA Journal of Lightwave Technology. 2006;24(12):4628-4641
- [7] Alavi SE, Soltanian MRK, et al. Towards 5G: A photonic based millimeter wave signal generation for applying in 5G access fronthaul. Scientific Reports. 2016;6:11
- [8] Capmany J, Novak D. Microwave photonics combines two worlds. Nature Photonics. 2007;1(1):319-330
- [9] Belkin ME, Golovin V, Tyschuk Y, Sigov AS. Comparison of RF photonics-based beamformers for super-wide bandwidth phased array antennas. IOP Conference Series: Materials Science and Engineering. 2017;198:1-4
- [10] Andrews JG et al. What will 5G be? IEEE Journal on Selected Areas in Communications. 2014;32(6):1065-1082
- [11] Chen S, Zhao J. The requirements, challenges and technologies for 5G of terrestrial mobile telecommunication. IEEE Communications Magazine. 2014;52(5):36-43
- [12] Munn J. Our 5G future: In the fast lane with numerical simulation. Microwaves & RF. 2016;55(11):48-50
- [13] Frenzel L. Making 5G happen. Microwaves & RF. 2017;56(12):1-5
- [14] Boccardi F et al. Five disruptive technology directions for 5G. IEEE Communications Magazine. 2014;52:74-80
- [15] Novak D, Waterhouse R. Emerging disruptive wireless technologies – Prospects and challenges for integration with optical networks. In: Proceedings of Optical Fiber Communication Conference. 2013. pp. 1-3
- [16] Al-Dabbagh RK, Al-Raweshidy HS. 64-GHz millimeter-wave photonic generation with a feasible radio over fiber system. Optical Engineering. 2017;56(2):11
- [17] Vook F, Ghosh A, Thomas T. MIMO and beamforming for 5G technology. In: Proceedings of IEEE International Microwave Symposium. 2014. 4 p
- [18] Browne J. What role will millimeter waves play in 5G wireless systems? Microwaves & RF. 2018;57(4):38-42
- [19] 5G Americas White Paper on 5G Spectrum Recommendations; Apr. 2017. 28 p
- [20] Yao J. Microwave photonics. Journal of Lightwave Technology. 2009;27(3):314-335
- [21] Urlick VJ, McKinney JD, Williams KJ. Fundamentals of Microwave Photonics. New Jersey: Hoboken; 2015. 489 p
- [22] Paoletta AC, De Salvo R, Middleton C, Logan C. Direction in radio frequency photonic systems. In: WAMICON 2015: Proceedings of the IEEE 16th Wireless and Microwave Technology Conference. Cocoa Beach, FL, USA. 6 p

- [23] Frank J. Bandwidth criteria for phased-array antennas. In: Oliner A, Knittel G, editors. *Phased-Array Antennas*. Dedham, MA: Artech House; 1972. pp. 243-253
- [24] Fathpour S, Riza NA. Silicon-photonics-based wideband radar beamforming: Basic design. *Optical Engineering*. 2010;**49**(1):018201. 7 p
- [25] Shahoei H, Li M, Yao JP. Continuously tunable time delay using an optically pumped linearly chirped fiber Bragg grating. *Journal of Lightwave Technology*. 2011;**29**(10):1465-1472
- [26] Vidal B, Mengual T, Marti J. Fast optical beamforming architectures for satellite-based applications. *Advances in Optical Technologies*. 2012;**2012**:5. Hindawi Publishing Corporation
- [27] Jiang Y, Howley B, Shi Z, et al. Dispersion-enhanced photonic crystal fiber array for a true time-delay structured X-band phased array antenna. *IEEE Photonics Technology Letters*. 2005;**17**(1):187-189
- [28] Vodjdani N, Granger G, Mongardien D, Enard A, Fourdin C, Chazelas J. 8 channels, 5 bits wideband optical beam steering up to Ku band. In: *International Topical Meeting on Microwave Photonics*. 2003. pp. 389-391
- [29] Shi N, Li M, Deng Y, Zhang L, Sun S, Tang J, et al. Experimental demonstration of a multi-target detection technique using an X-band optically steered phased array radar. *Optics Express*. 2016;**24**(13):14438-14450
- [30] Yihong C, Chen RT. A fully packaged true time delay module for a K-band phased array antenna system demonstration. *IEEE Photonics Technology Letters*. 2002;**14**(8):1175-1177
- [31] Zhuang L et al. Ring resonator-based single-chip  $1 \times 8$  optical beam forming network in LPCVD waveguide technology. In: *LEOS Benelux Proceedings*. 2006. pp. 45-48
- [32] Jung BM, Yao J. A two-dimensional optical true time-delay Beamformer consisting of a fiber Bragg grating prism and switch-based fiber-optic delay lines. *IEEE Photonics Technology Letters*. 2009;**21**(10):627-629
- [33] Piqueras MA et al. Optically beamformed beamswitched adaptive antennas for fixed and mobile broadband wireless access networks. *IEEE Transactions on Microwave Theory and Techniques*. 2006;**54**(2):887-899
- [34] Zhuang L et al. On-chip microwave photonic beamformer circuits operating with phase modulation and direct detection. *Optics Express*. 2014;**22**(14):17079-17091
- [35] Yang DH, Lin WP. Phased-array beam steering using optical true time delay technique. *Optics Communication*. 2015;**350**:90-96
- [36] Zhang J, Yao J. Photonic true-time delay Beamforming using a switch-controlled wavelength-dependent recirculating loop. *Journal of Lightwave Technology*. 2016;**34**(16):3923-3929
- [37] Zhuang L et al. Novel ring resonator-based integrated photonic beamformer for broadband phased array receive antennas— Part II: Experimental prototype. *Journal of Lightwave Technology*. 2010;**28**(1):19-31
- [38] Mohammed JR, Sayidmarie KH. Synthesizing asymmetric SideLobe pattern with steered nulling in non-uniformly excited linear arrays by controlling edge elements. *International Journal of Antennas and Propagation*. 2017;**2017**. Article ID 9293031, 8 pages



[39] Belkin ME, Golovin V, Tyschuk Y, Vasil'ev M, Sigov AS. Computer-aided design of microwave-photonics-based RF circuits and systems. In: Loo XS, editor. RF Systems, Circuits and Components. United Kingdom: IntechOpen Publishing. 20 p. (in print)

[40] Zhuang L et al. Low-loss, high-index-contrast Si<sub>3</sub>N<sub>4</sub>/SiO<sub>2</sub> optical waveguides for optical delay lines in microwave photonics signal processing. *Optics Express*. 2011;**19**(23):23162-23170

[41] Belkin ME, Golovin V, Tyschuk Y, Sigov AS. A simulation technique for designing next-generation information and communication systems based on off-the-shelf microwave electronics computer tool. *International Journal of Simulation and Process Modelling*. 2018;**13**(3):238-254



# Array Pattern Based on Integrated Antenna

*Daehee Park and Dong-Ho Cho*

## Abstract

The number of required antenna elements is rapidly increasing, in compliance with the development of massive multiple-input multiple-output (MIMO) and beamforming techniques in 5G technology. Integrated antenna, which is composed of multiple antenna elements, will be considered for next-generation technologies. Therefore, in this chapter, we provide the mathematical and practical explanation of the integrated antenna for the next-generation technologies. First, we introduce a mathematical expression of an antenna element based on spherical vector wave modes and explain channel models for the integrated antenna and the antenna array based on the integrated antenna. Second, we provide practical antennas designed as the integrated antenna and verify that the integrated antenna array can be implemented practically. Lastly, we evaluate the performance of the integrated antenna array compared to mono-polarization and dual-polarization dipole arrays.

**Keywords:** integrated antenna, integrated antenna array, spherical vector wave, channel model, practical antenna

## 1. Introduction

As more high speed is required, many 5G communication systems have been proposed. While there are a lot of technologies for the 5G communication system, multiple-input multiple-output (MIMO) system is a basis for the 5G communication system. MIMO system has been proposed to increase spectral efficiency and diversity gain in wireless communication. The MIMO technology enhances the spectral efficiency and diversity gain by utilizing multiple antennas, because the multiple antennas provide multiple channels [1, 2]. In order to obtain multiple channels, the antenna elements have to be separated from the other antenna elements with larger gap than half-wavelength distance. However, it is difficult to increase the number of antennas because the antenna size is limited in wireless communication.

To enhance the spectral efficiency with compact antenna size, dual-polarization antenna array has been used for 5G technology [3]. It is possible to obtain two uncorrelated channels using the orthogonality of the dual-polarization antenna. However, the dual-polarization antenna still has limitation to increase the spectral efficiency without expanding antenna space.

It has been studied to enhance the spectral efficiency without increasing antenna space by using multiple radiation patterns of the antennas [4–7]. It was theoretically proposed that six times of spectral efficiency can be obtained compared to a single antenna by using three electric dipoles and three magnetic dipoles allocated at the same position. It means that the multiple antennas can be integrated within a compact size and provide multiplexing gain. Thus, the MIMO system can increase the spectral efficiency by not only using larger antenna array size but also combining multiple radiation patterns.

On the other hand, there have been studies of array optimization technologies for the linear antenna array according to various objective functions [8, 9]. This antenna array could have better interference cancelation using genetic algorithms. Then, it is also possible to enhance the spectral efficiency and diversity gain by combining the array optimization technologies and the integrated antenna-based array system.

In this chapter, we introduce an integrated antenna array which is a type of the MIMO systems. The integrated antenna array consists of multiple array elements, and the array element has multiple antenna elements. Each antenna element of the integrated antenna has different radiation patterns to increase the spectral efficiency in wireless communication area. The purpose of this chapter is to introduce the concept of the integrated antenna array and to show the possibility to apply it practically to wireless communication technology. We will also explain a framework for next-generation technology so that we can provide further works as well.

We organize the chapter as follows. In Section 2, we explain channel models for the integrated antenna array. In Section 3, several practical integrated antennas are introduced to verify that the integrated antenna array can be implemented practically. In Section 4, we verify the performance of the integrated antenna array in urban macro-cell environment compared with mono-polarization and dual-polarization dipole antenna arrays.

## 2. Channel model

The channel model is dependent on the structure of the MIMO system. To provide the channel model for the integrated antenna array, firstly we provide a channel model for a general case as given in **Figure 1** [1]. We develop the channel model with considering complex structures.

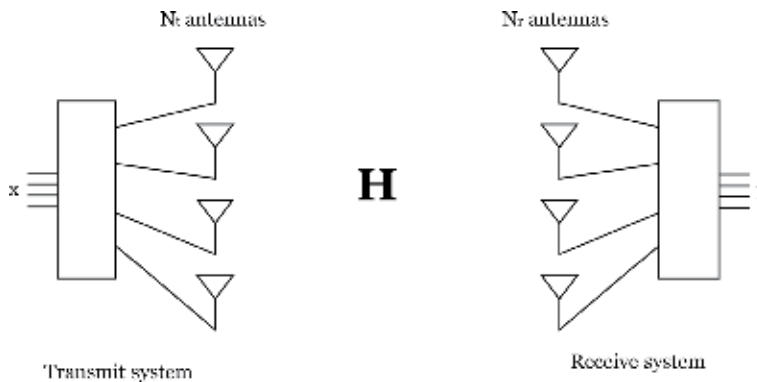


**Figure 1.**  
Configuration of general MIMO system.

## 2.1 MIMO channel model

We consider a MIMO channel with a transmit and receive system, which is equipped with  $N_t$  antennas and  $N_r$  antennas, respectively. The received signal  $\mathbf{y}$  can be expressed as

$$\mathbf{y} = \mathbf{H}\mathbf{x} + \mathbf{n}, \quad (1)$$

where  $\mathbf{H}$  is the  $N_r \times N_t$  MIMO channel,  $\mathbf{x}$  is an  $N_t \times 1$  transmit signal and  $\mathbf{n}$  is an  $N_r \times 1$  complex Gaussian noise. Based on spatial fading correlation, the elements of  $\mathbf{H}$  can be described as

$$\mathbf{h} = \text{vec}(\mathbf{H}) = \mathbf{R}_{\mathbf{h}}^{1/2} \text{vec}(\mathbf{H}_w), \quad (2)$$

where  $\mathbf{H}_w$  is an  $N_r \times N_t$  Rayleigh fading channel with uncorrelated and zero mean entries which follow complex Gaussian distribution,  $\mathbf{R}_{\mathbf{h}} = \mathbb{E}\{\mathbf{h}\mathbf{h}^\dagger\}$  is the  $N_r N_t \times N_r N_t$  covariance matrix and  $(\cdot)^\dagger$  and  $\mathbb{E}\{\cdot\}$  are Hermitian and expectation operator, respectively [1]. Here,  $\text{vec}(\mathbf{A})$  is a vectorization operation to produce a vector with the columns of  $\mathbf{A}$ .

We assume that the sizes of the transmit and receive antenna are negligible compared to the distance between the transmit system and the receive system. Then, the covariance matrix of the MIMO channel is given by

$$\mathbf{R}_{\mathbf{h}} = \mathbf{R}'_{\mathbf{H}_t} \otimes \mathbf{R}_{\mathbf{H}_r}, \quad (3)$$

where  $\mathbf{R}_{\mathbf{H}_t} = \mathbb{E}\{\mathbf{H}\mathbf{H}^\dagger\}$ ,  $\mathbf{R}_{\mathbf{H}_r} = \mathbb{E}\{\mathbf{H}^\dagger\mathbf{H}\}$  and  $(\cdot)'$  and  $\otimes$  are matrix transpose and Kronecker product operator, respectively. Therefore, the MIMO channel can be described as [1]

$$\mathbf{H} = \mathbf{R}_{\mathbf{H}_t}^{1/2} \mathbf{H}_w \mathbf{R}_{\mathbf{H}_r}^{1/2}. \quad (4)$$

This channel model is called by the Kronecker model of MIMO system in general case.

## 2.2 Spherical vector wave-based channel model

There are spherical vector wave (SVW) modes which are orthonormal basis functions for arbitrary radiation pattern [10–12]. The radiation pattern of an arbitrary transmitter antenna is described as

$$\begin{aligned} \mathbf{F}(\hat{\mathbf{r}}) &= k\sqrt{2\eta} \sum_{i=1}^{i_{\max}} \sum_{\nu=0}^i \sum_{\tau=1}^2 \sum_j j^{\tau-i+2} T_{i\nu\tau} \mathbf{A}_{i\nu\tau}(\hat{\mathbf{r}}) \\ &= k\sqrt{2\eta} \sum_{\alpha=1}^{\alpha_{\max}} j^{\tau-i+2} T_{\alpha} \mathbf{A}_{\alpha}(\hat{\mathbf{r}}) = k\sqrt{2\eta} \mathbf{A}'(\hat{\mathbf{r}}) \mathbf{t}, \end{aligned} \quad (5)$$

where  $\hat{\mathbf{r}}$  is the direction of the radiation,  $\mathbf{A}_{i\nu\tau}(\hat{\mathbf{r}}) = \mathbf{A}_{\alpha}(\hat{\mathbf{r}}) = [A_{\theta,\alpha}(\hat{\mathbf{r}}) A_{\phi,\alpha}(\hat{\mathbf{r}})]$  is  $\alpha$ th SVW mode with the multi-index  $\alpha = 2(i(i+1) - 1 + (-1)^\nu \nu) + \tau$ ,  $\alpha_{\max}$  is the maximum number of SVW modes,  $\mathbf{A}(\hat{\mathbf{r}})$  is an  $\alpha_{\max} \times 2$  matrix containing the row vector  $j^{\tau-i+2} \mathbf{A}_{\alpha}(\hat{\mathbf{r}})$  and  $\mathbf{t}$  is an  $\alpha_{\max} \times 1$  vector with the element  $T_{\alpha}$  which is the transmitting coefficient of the transmitter antenna [10]. The SVW mode  $\mathbf{A}_{\alpha}(\hat{\mathbf{r}})$  is described well in Appendix. In order to decompose the radiation pattern of a receiver antenna, the

receiving coefficient  $R_{\nu\sigma\tau}$  can be given by  $R_{\nu1\tau} = (-1)^\nu T_{\nu2\tau}$  and  $R_{\nu2\tau} = (-1)^\nu T_{\nu1\tau}$  by using the reciprocity relationship [10, 12].

Consider that the transmit and the receive systems have an integrated antenna without array structure, which are composed of  $N_t$  and  $N_r$  antennas as shown in **Figure 2**, respectively. From (1), the MIMO channel  $\mathbf{H}$  may be expressed as

$$\mathbf{y} = \mathbf{RMT}\mathbf{x} + \mathbf{n}, \quad (6)$$

where  $\mathbf{R}$  is an  $N_r \times M_r$  matrix with the receiving coefficient  $R_{n_r, m_r}$ ,  $\mathbf{T}$  is a  $M_t \times N_t$  matrix with the transmitting coefficient  $T_{m_t, n_t}$  and  $\mathbf{M}$  is a  $M_r \times M_t$  matrix which is the channel between SVW modes [10, 12, 13]. Then, the covariance matrix of the channel  $\mathbf{H}$  can be derived by [14]

$$\mathbf{R}_h = (\mathbf{T}' \otimes \mathbf{R}) \mathbf{R}_m (\mathbf{T}' \otimes \mathbf{R})^\dagger, \quad (7)$$

where  $\mathbf{h} = \text{vec}(\mathbf{H}) = (\mathbf{T}' \otimes \mathbf{R}) \mathbf{m}$ ,  $\mathbf{m} = \text{vec}(\mathbf{M})$  and  $\mathbf{R}_m = \mathbb{E}\{\mathbf{m}\mathbf{m}^\dagger\}$ . The covariance matrix of the channel for the SVW modes can be described as

$$\mathbf{R}_m = 4\pi^2 \iint \tilde{\mathbf{A}}(\hat{\mathbf{k}}_r, \hat{\mathbf{k}}_t) \mathbf{P}(\hat{\mathbf{k}}_r, \hat{\mathbf{k}}_t) \tilde{\mathbf{A}}^\dagger(\hat{\mathbf{k}}_r, \hat{\mathbf{k}}_t) d\Omega_r d\Omega_t. \quad (8)$$

Here,  $\tilde{\mathbf{A}}(\hat{\mathbf{k}}_r, \hat{\mathbf{k}}_t) = \mathbf{A}(\hat{\mathbf{k}}_r) \otimes \mathbf{A}(\hat{\mathbf{k}}_t)$ , and  $\mathbf{P}(\hat{\mathbf{k}}_r, \hat{\mathbf{k}}_t) = \text{diag}(\mathcal{P}_{\theta\theta}, \mathcal{P}_{\theta\phi}, \mathcal{P}_{\phi\theta}, \mathcal{P}_{\phi\phi})$  where  $\mathcal{P}_{\alpha\beta} \equiv \mathcal{P}_{\alpha\beta}(\hat{\mathbf{k}}_r, \hat{\mathbf{k}}_t)$  are functions of the power angular spread (PAS) which is expressed by

$$\mathcal{P}_{\alpha\beta}(\hat{\mathbf{k}}_r, \hat{\mathbf{k}}_t) = P_{\alpha\beta} p_{\alpha\beta}(\hat{\mathbf{k}}_r, \hat{\mathbf{k}}_t), \quad (9)$$

where  $\alpha \in \{\theta, \phi\}$ ,  $\beta \in \{\theta, \phi\}$  and  $P_{\alpha\beta}$  is coupling power from  $\beta$  to  $\alpha$  [15]. The joint probability function  $p_{\alpha\beta}(\hat{\mathbf{k}}_r, \hat{\mathbf{k}}_t)$  is required to be normalized as follows:

$$\iint p_{\alpha\beta}(\hat{\mathbf{k}}_r, \hat{\mathbf{k}}_t) d\Omega_r d\Omega_t = 1. \quad (10)$$

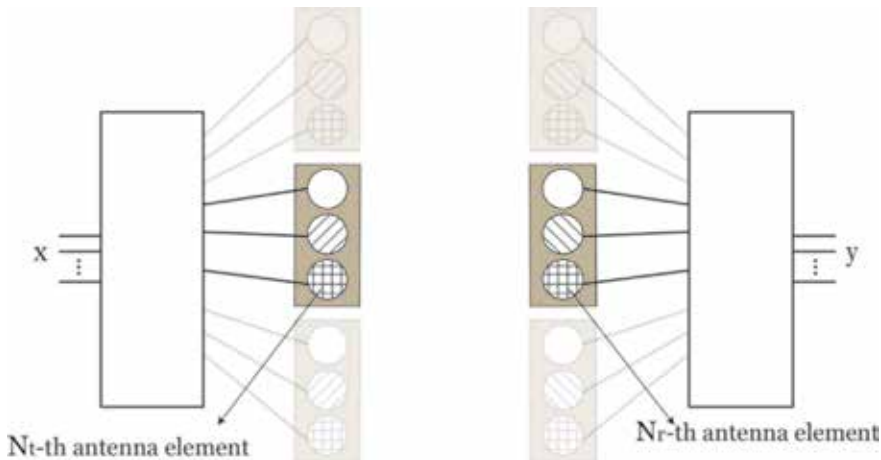


**Figure 2.** Configuration of MIMO system with integrated antenna.

It is also assumed that the joint probability density function of the PAS in (10) can be decomposed by

$$p_{\alpha\beta}(\hat{\mathbf{k}}_r, \hat{\mathbf{k}}_t) = p_{\alpha\beta}(\hat{\mathbf{k}}_r) p_{\alpha\beta}(\hat{\mathbf{k}}_t). \quad (11)$$

Then, the SVW mode channel of the transmitter is obtained by [14].

$$\mathbf{R}_{M_t} = 2\pi \int \mathbf{A}^*(\hat{\mathbf{k}}_t) \mathbf{P}(\hat{\mathbf{k}}_t) \mathbf{A}'(\hat{\mathbf{k}}_t) d\Omega_t, \text{ and } \mathbf{R}_{M_r} = 2\pi \int \mathbf{A}^*(\hat{\mathbf{k}}_r) \mathbf{P}(\hat{\mathbf{k}}_r) \mathbf{A}'(\hat{\mathbf{k}}_r) d\Omega_r. \quad (12)$$

where  $\mathbf{P}(\hat{\mathbf{k}}_t) = \text{diag}\{\mathcal{P}_\theta(\hat{\mathbf{k}}_t), \mathcal{P}_\phi(\hat{\mathbf{k}}_t)\}$ ,  $\mathcal{P}_\alpha(\hat{\mathbf{k}}_t) = P_\alpha p_\alpha(\hat{\mathbf{k}}_t)$  and  $p_\alpha(\hat{\mathbf{k}}_t)$  is the PAS of orthogonal polarization  $\alpha$  at transmitter side and  $\alpha$  stands for  $\theta$  and  $\phi$ .

From (3) and (7), therefore, we can see that

$$\mathbf{R}_{H_t} = \mathbf{T}^\dagger \mathbf{R}_{M_t} \mathbf{T}, \mathbf{R}_{H_r} = \mathbf{R} \mathbf{R}_{M_r} \mathbf{R}^\dagger. \quad (13)$$

We can describe the channel model for the integrated antenna by using the SVW modes.

### 2.3 Channel model for integrated antenna array

For 5G communication technology, it is important that the integrated antenna is expandable to array structure. Thus, it is necessary to derive the channel model for the MIMO system equipped with the integrated antenna array. The structure of the integrated antenna array is illustrated in **Figure 3**.

Each antenna element has not only a radiation pattern but also a relative position to the other antenna elements. The received signal of the MIMO system with the integrated antenna arrays is given by

$$\mathbf{y} = \check{\mathbf{R}} \check{\mathbf{M}} \check{\mathbf{T}} \mathbf{x} + \mathbf{n}, \quad (14)$$

where  $\check{\mathbf{M}}$  is the  $M_r L_r \times M_t L_t$  extended SVW mode channel, which considers antenna positions;  $\check{\mathbf{R}} = \mathbf{I}_{L_r} \otimes \mathbf{R}$ , where  $\mathbf{R}$  is an  $B_r \times M_r$  receiving coefficient matrix of the receive integrated antenna; and  $\check{\mathbf{T}} = \mathbf{I}_{L_t} \otimes \mathbf{T}$ , where  $\mathbf{T}$  and  $\mathbf{I}_N$  are a  $M_t \times B_t$

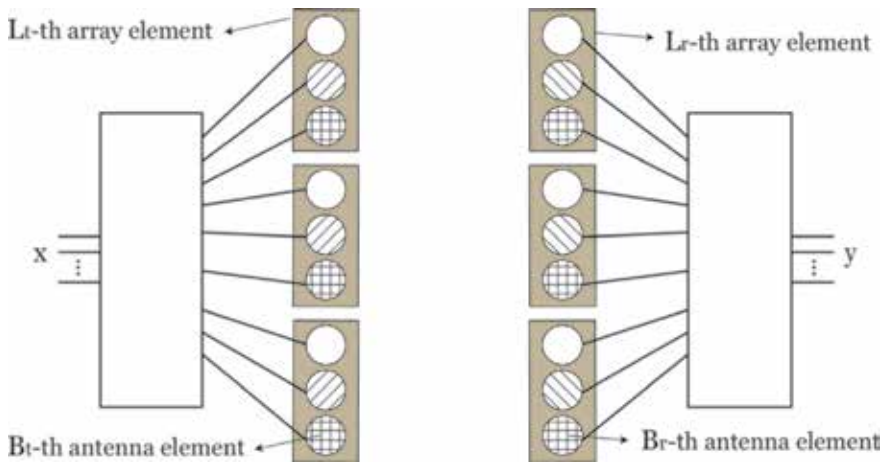


**Figure 3.** Configuration of MIMO system with integrated antenna array.

transmitting coefficient matrix of the transmit integrated antenna and an  $N \times N$  identity matrix. The covariance matrix of the MIMO channel  $\mathbf{H}$  can be described as

$$\mathbf{R}_{\mathbf{h}} = \left( \check{\mathbf{T}}' \otimes \check{\mathbf{R}} \right) \mathbf{R} \check{\mathbf{m}} \left( \check{\mathbf{T}}' \otimes \check{\mathbf{R}} \right)^\dagger, \quad (15)$$

where  $\mathbf{h} = \left( \check{\mathbf{T}}' \otimes \check{\mathbf{R}} \right) \check{\mathbf{m}}$ ,  $\check{\mathbf{m}} = \text{vec}(\check{\mathbf{M}})$  and  $\mathbf{R} \check{\mathbf{m}} = \mathbb{E} \left\{ \frac{\check{\mathbf{m}} \check{\mathbf{m}}^\dagger}{\check{\mathbf{m}}^\dagger \check{\mathbf{m}}} \right\}$ . Here, the correlation matrix of the channel of the SVW modes can be given by

$$\mathbf{R} \check{\mathbf{m}} = 4\pi^2 \iint \tilde{\mathbf{B}}(\hat{\mathbf{k}}_r, \hat{\mathbf{k}}_t) \mathbf{P}(\hat{\mathbf{k}}_r, \hat{\mathbf{k}}_t) \tilde{\mathbf{B}}^\dagger(\hat{\mathbf{k}}_r, \hat{\mathbf{k}}_t) d\Omega_r d\Omega_t, \quad (16)$$

where  $\tilde{\mathbf{B}}(\hat{\mathbf{k}}_r, \hat{\mathbf{k}}_t) = \mathbf{B}(\hat{\mathbf{k}}_r) \otimes \mathbf{B}(\hat{\mathbf{k}}_t)$ . Here,  $\mathbf{B}(\hat{\mathbf{k}}_r) = \mathbf{e}_r(\hat{\mathbf{k}}_r) \otimes \mathbf{A}(\hat{\mathbf{k}}_r)$ , and the  $\mathbf{E}(\hat{\mathbf{k}})$  is an array element response matrix with the elements of  $e_l(\hat{\mathbf{k}}) = e^{j\beta(\mathbf{r}_l - \mathbf{r}_o) \cdot \hat{\mathbf{k}}}$ , where  $\mathbf{r}_l$  is the position of the  $l$ th array element and  $\mathbf{r}_o$  is the position of the antenna array system.

We explained the channel models for the MIMO system with the integrated antenna arrays mathematically. In the following section, we will verify the performance of the integrated antenna array based on the channel model we discussed.

### 3. Practical antenna design

There have been many practical antennas which are designed for the integrated antenna. Through some practical antennas, we can see that the integrated antenna may be implemented for the wireless communication. Design of the integrated antenna is dependent on the system requirement such as array structure and channel environment. In this section, we introduce various practical integrated antennas for several cases.

#### 3.1 Practical integrated antenna

It is important to integrate multiple antennas with compact size, which have orthogonal radiation patterns of each other. There are practical integrated antennas without considering array structure as shown in **Figure 4**. It is found that the integrated antenna has two types of antenna elements which have radiation patterns of electric dipole antenna and magnetic loop antenna. Planer inverted-F antennas (PIFA) are used for the electric dipole antenna, and quarter-wavelength slot antennas are used for the magnetic loop antenna [16, 17]. It is also seen that the integrated antennas have three-dimensional structures because the array structure was not considered. Therefore, it is noted that the integrated antenna may consist of more than two antenna elements practically.

#### 3.2 Practical integrated antenna array

The integrated antenna array may be implemented as shown in **Figure 5**. It is found that the practical integrated antenna array is composed of  $L_t$  array elements. Each array element consists of  $B_t$  antenna elements, which are designed by utilizing a planer Yagi-Uda antenna [18].

To reduce the antenna size, we eliminated a conduct strip in front of the antenna element and designed that  $l_3$  is larger than  $w_2$  as shown in **Figure 5a**. The radiation



direction of the antenna element can be changed according to  $\theta_{\text{rad}}$ , because the antenna element radiates perpendicularly to the antenna structure. The parameters are given by  $L = 70$  mm,  $W = 66$  mm,  $l_c = 22$  mm,  $w_c = 1.5$  mm,  $l_s = 24.5$  mm,  $w_s = 1.5$  mm,  $l_f = 6.2$  mm,  $w_p = 8$  mm and  $l_p = 32$  mm. It is possible to control the impedance matching by modifying  $l_7$  and  $w_6$ . The integrated antenna is produced on a CER-10 substrate with a permittivity of 10 and a thickness of 0.64 mm. The

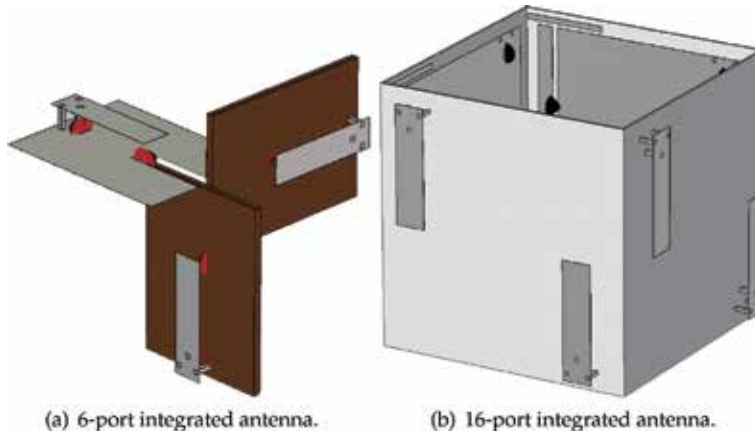


**Figure 4.** Configuration of practical integrated antennas. (a) 6-port integrated antenna and (b) 16-port integrated antenna.

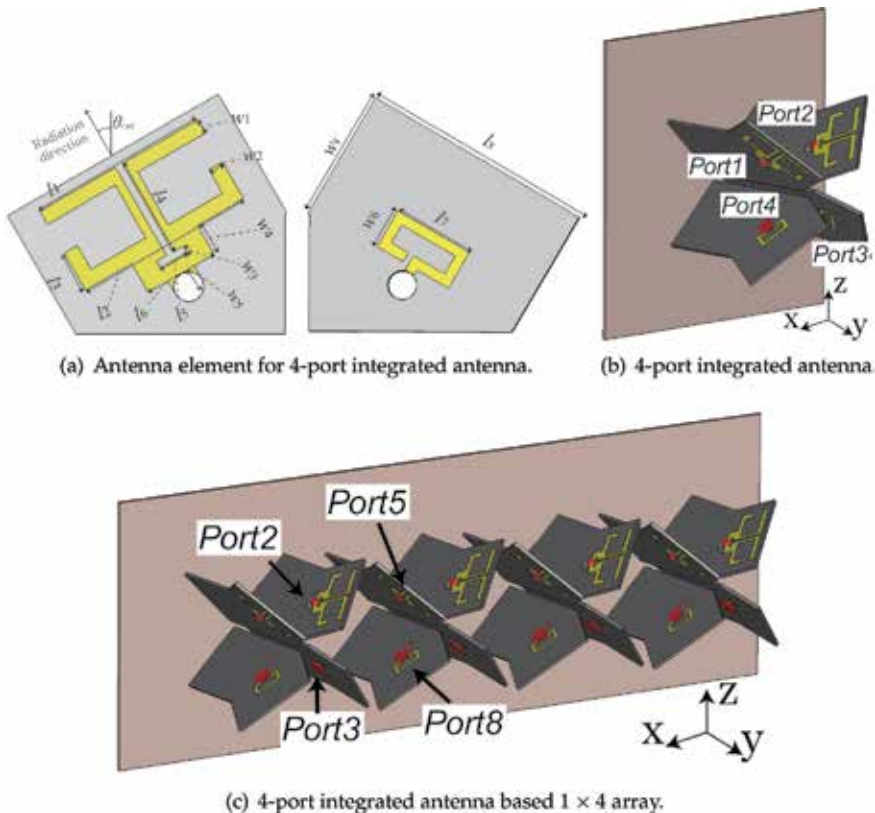


**Figure 5.** Configuration of practical integrated antenna array. (a) Antenna element for 4-port integrated antenna, (b) 4-port integrated antenna and (c) 4-port integrated antenna based  $1 \times 4$  array.

integrated antenna is expandable to the array structure as shown in **Figure 4c**, because of the compactness of the integrated antenna.

It is necessary to verify that the integrated antenna has reasonable antenna characteristics such as radiation efficiency, bandwidth and mutual coupling. The proposed four-port integrated antenna was implemented as shown in **Figure 6**. For the integrated antenna, the antenna elements have the same antenna characteristics of each other because of symmetric configuration. The simulated and the measured S-parameters of the integrated antenna are shown in **Figure 7a** and **b**, respectively, where  $S_{aa}$  means  $S_{1,1}$ ,  $S_{2,2}$ ,  $S_{3,3}$  and  $S_{4,4}$ ;  $S_{ab}$  means  $S_{1,2}$ ,  $S_{1,4}$ ,  $S_{2,3}$  and  $S_{3,4}$ ; and  $S_{ac}$  means  $S_{1,3}$  and  $S_{2,4}$ . The integrated antennas radiate at 5.7 GHz with a bandwidth of about 300 MHz satisfying  $|S_{aa}| = -10$  dB in the simulation and measurement. It is also found that the antenna elements have less than  $-12$  dB mutual couplings in the simulation and measurement.

The simulated and measured S-parameters of the integrated antenna-based  $1 \times 4$  array system are shown in **Figure 8a** and **b**, respectively. Only the S-parameters for *Port 5* are illustrated because the integrated antenna-based array has

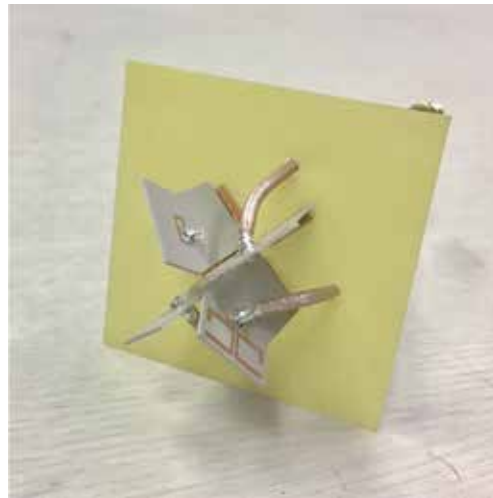


**Figure 6.**  
Prototype of four-port integrated antenna.

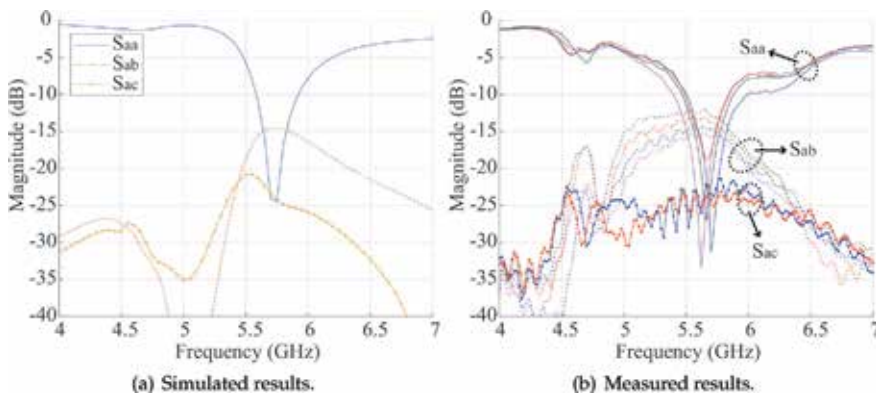


**Figure 7.**  
S-parameters of four-port integrated antenna. (a) Simulated results and (b) measured results.

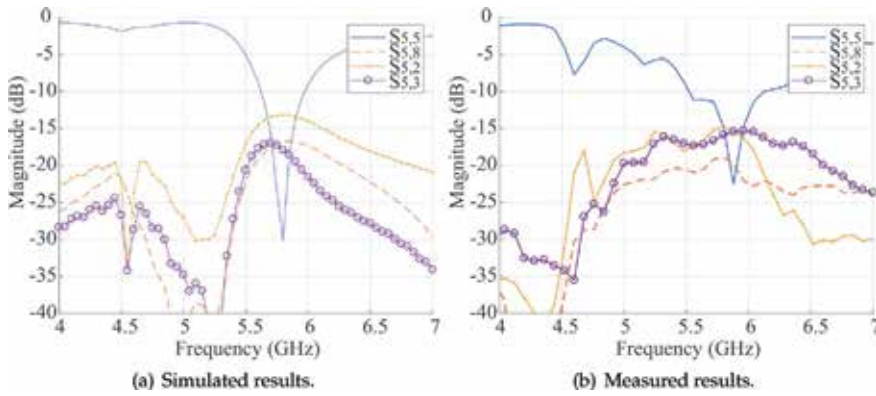


**Figure 8.** S-parameters of integrated antenna-based  $1 \times 4$  array. (a) Simulated results and (b) measured results.

a symmetric configuration. It is found that the mutual coupling between antenna elements of different array elements is lower by about  $-13$  dB in simulation and measurement results. Thus, it can be noted that the integrated antenna is scalable in the array structure.

The radiation patterns of the integrated antenna are illustrated in **Figure 9**. It is found that the simulated and measured radiation patterns are agreed well. It is shown that the antenna elements radiate to y-axis in order to support the front area of the antenna structure and have different radiation patterns. The radiation patterns generated by using the transmitting coefficient matrix  $T$  are similar to the simulated radiation patterns as well. Thus, it can be noted that the radiation patterns of the practical antenna can be described in a mathematical expression.

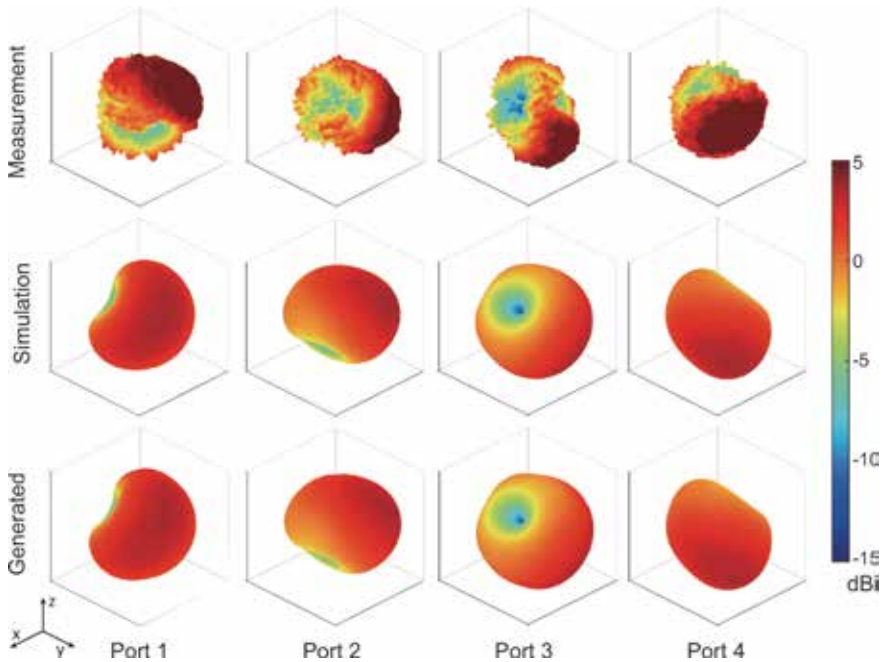


**Figure 9.** Radiation patterns of proposed four-port pattern antenna.

#### 4. Array optimization based on integrated antenna array

It is important to combine the integrated antenna array and the array optimization algorithm. We assume that the integrated antenna array is utilized as a transmit system, and then the channel capacity of the MIMO system may be described as

$$C = \mathbb{E} \left\{ \log \det \left( \mathbf{I}_{N_r} + \frac{\text{SNR}}{N_t} \mathbf{H} \mathbf{W} \mathbf{W}^\dagger \mathbf{H}^\dagger \right) \right\}, \quad (17)$$

where SNR is signal-to-noise ratio and  $\mathbf{W}$  is a precoding matrix [19]. To simplify the optimization problem, we consider that the receive system has ideal channel condition, which means  $\mathbf{R}_{\mathbf{H}_r} = \mathbf{I}$ . From (4) and (13), the MIMO channel  $\mathbf{H}$  is given by  $\mathbf{H} = \mathbf{H}_w \mathbf{R}_{\mathbf{H}_t}^{1/2}$ , where  $\mathbf{R}_{\mathbf{H}_t} = \check{\mathbf{T}}^\dagger \mathbf{R}_{\check{\mathbf{M}}_t} \check{\mathbf{T}}$ . There are three variables  $\mathbf{R}_{\check{\mathbf{M}}_t}$ ,  $\check{\mathbf{T}}$  and  $\mathbf{W}$  in (17). We can control  $\check{\mathbf{T}}$  and  $\mathbf{W}$  according to  $\mathbf{R}_{\check{\mathbf{M}}_t}$ , which is given by the channel environment.

However,  $\check{\mathbf{T}}$  and  $\mathbf{W}$  have different characteristics. First,  $\check{\mathbf{T}}$  is determined by the structure of the integrated antenna array, while  $\mathbf{W}$  can be changed in real time. Second,  $\check{\mathbf{T}}$  is dependent on the specification of the integrated antenna such as antenna space, required bandwidth and the number of antenna elements.  $\mathbf{W}$  is dependent on the specification of RF chains such as resolutions of phase shifter and attenuator. Lastly, it is not clear to implement a specific integrated antenna according to an arbitrary  $\check{\mathbf{T}}$ .

Therefore, it is necessary to optimize the  $\check{\mathbf{T}}$  and  $\mathbf{W}$  with different constraints. We study the optimization of  $\mathbf{W}$  under practical  $\check{\mathbf{T}}$ .

##### 4.1 Performance of integrated antenna

In order to show the possibility of the integrated antenna in wireless communication area, we verify the performance of the integrated antenna by optimizing  $\mathbf{W}$  under fixed  $\mathbf{T}$  given by the practical 16-port and 4-port integrated antennas in the previous section.

There are various objective functions for optimization of  $\mathbf{W}$ , such as maximizations of spectral and energy efficiency and minimizations of interference and side lobe level [12]. Here, we consider an objective function as a maximization of spectral efficiency expressed by

$$f = \max_{\text{Tr}\{\mathbf{W}\mathbf{W}^\dagger\}=N_t} C. \quad (18)$$

To obtain the optimum value of  $\mathbf{W}$ , we apply a singular value decomposition (SVD) precoding method into the integrated antenna array [19]. This SVD precoding method provides the precoding matrix  $\mathbf{W} = [\mathbf{v}_1 \cdots \mathbf{v}_{N_t}]$ , where  $\mathbf{U}\mathbf{S}\mathbf{V}^\dagger = \text{svd}(\mathbf{H})$  and  $\mathbf{V} = [\mathbf{v}_1 \cdots \mathbf{v}_{N_t}]$ .

We consider the 16-port integrated antenna as the integrated antenna without array structure. We assume that the receive system has 16 antennas and that the channel is a full-scattering environment, which has the PAS given by

$$p_{\theta_i}(\theta, \phi) = p_{\phi_i}(\theta, \phi) = \frac{1}{2\pi^2}, \theta \in [0, \pi], \phi \in [-\pi, \pi]. \quad (19)$$

The channel capacity of the 16-port integrated antenna is described in **Figure 10**. It is found that the channel capacity of 16-port integrated antenna achieves channel capacity close to that of the ideal 16-port antenna.

#### 4.2 Performance of integrated antenna array

We consider the four-port integrated antenna, which was proposed in Section 3 as the array element of the integrated antenna array. We assume that all antenna arrays have  $N_t = 16$  antenna elements and that the receive system has ideal channel condition which means  $\mathbf{R}_H = \mathbf{I}_{N_r}$ . We verify the performance of the integrated antenna array compared to two reference arrays as shown in **Figure 11**. The reference arrays are mono-polarization (MPOL) and dual-polarization (DPOL) antenna arrays. The MPOL and DPOL antenna arrays have array elements which are composed of mono-polarization dipole and dual-polarization dipoles, respectively. Then, MPOL, DPOL and integrated antenna arrays have  $B_t = 1, 2$  and 4 and  $L_t = 16, 8$  and 4, respectively. Here, we consider a channel model describing an urban macro-cell environment [20].

The channel capacities of the integrated MPOL and DPOL antenna arrays are illustrated in **Figure 12**. Although the integrated antenna array occupies smaller size than the others, the integrated antenna array has higher channel capacity than the MPOL and DPOL antenna arrays. It means that the multiple radiation patterns of various antenna elements for the integrated antenna may enhance the channel capacity without increasing antenna space to utilize spatial gain.

#### 4.3 Further works

To optimize an integrated antenna array in wireless communication area, we study the mathematical optimization of the integrated antenna array. Under assumption of  $\mathbf{W} = \mathbf{I}$ , we can derive an optimization problem given by

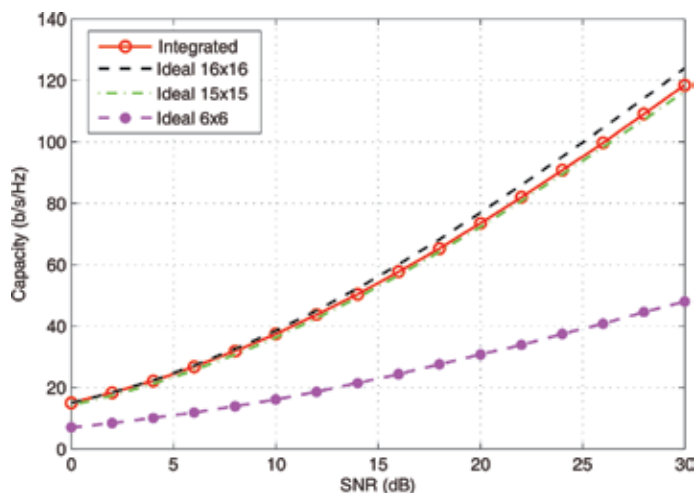


**Figure 10.**  
 Channel capacity of practical 16-port integrated antenna.

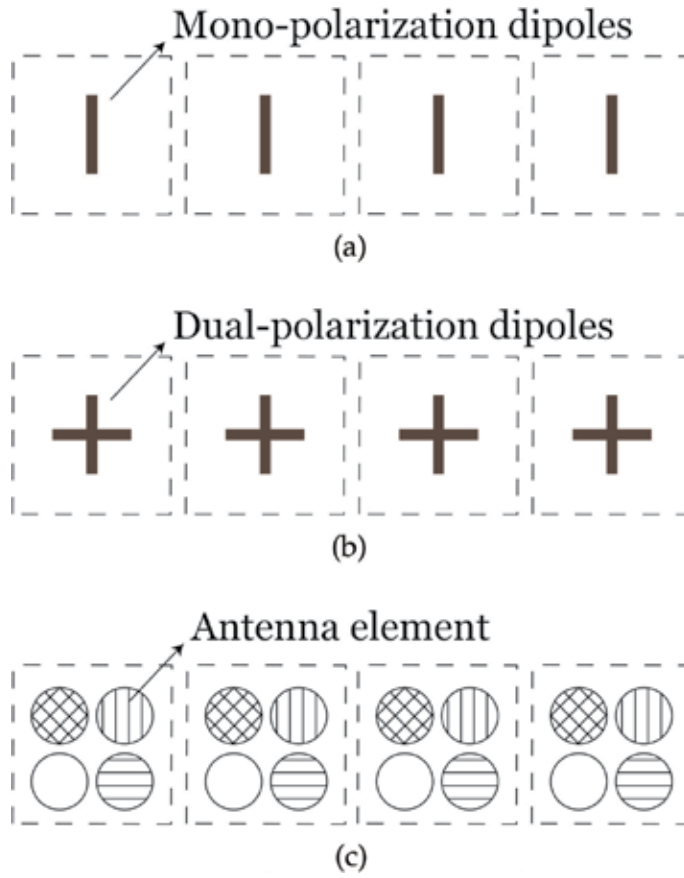


**Figure 11.**  
Configuration of antenna arrays.

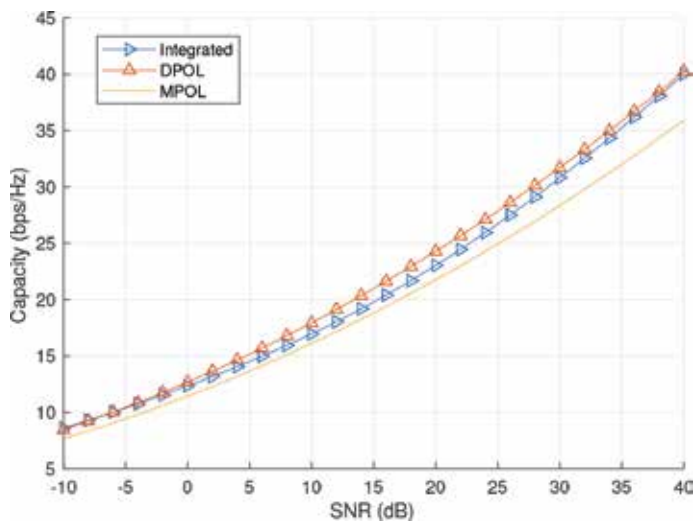


**Figure 12.**  
Channel capacities of various antenna arrays.

$$f = \max_{\text{Tr}\{\mathbf{T}^\dagger \mathbf{T}\} = M_t} \mathbb{E} \left\{ \log \det \left( \mathbf{I}_{N_r} + \frac{\text{SNR}}{N_t} \mathbf{H} \mathbf{H}^\dagger \right) \right\}. \quad (20)$$

However, the achievable  $\mathbf{T}$  is related to various physical parameters such as antenna space and Q-factor. Thus, it is necessary to design the structure of the integrated antenna which has a specific  $\mathbf{T}$ .

On the other hand, there are different constraints and objective functions for  $\mathbf{T}$  and  $\mathbf{W}$  as we mentioned. It is possible to apply various beamforming and precoding methods appropriately according to the structure of the integrated antenna array, such as hybrid-beamforming and low-complex precoding. It is also required to support multiple users with the integrated antenna array.

## 5. Conclusion

We introduced the integrated antenna array for the 5G communication technology and provided the MIMO channel model for the integrated antenna array. We showed that the integrated antenna can be implemented as practical antenna systems for the wireless communication. We also proposed the practical integrated antenna array with the four-port integrated antenna. Based on the MIMO channel model, we explained the optimization problems for the integrated antenna array. The performance of the integrated antenna array was verified compared to dual-polarization antenna array. It has been shown that the integrated antenna array can achieve higher spectral efficiency than the conventional antenna arrays. Therefore, it could be seen that the integrated antenna array would be an attractive solution for the next wireless communication technology.

## A. Appendix

In a source-free region  $V$  filled with a homogeneous medium, the electric field and magnetic field, with assumption of time dependence of  $\exp(-j\omega t)$ , satisfy

$$\nabla \times \nabla \times \mathbf{A}(\mathbf{r}) - k^2 \mathbf{A}(\mathbf{r}) = \mathbf{0}. \quad (21)$$

$\mathbf{A}(\mathbf{r})$  is derivable from the scalar potential  $\Psi(\mathbf{r})$  which satisfies

$$(\nabla^2 + k^2)\Psi(\mathbf{r}) = 0. \quad (22)$$

Consider vector wave functions  $\mathbf{M}(\mathbf{r})$ ,  $\mathbf{N}(\mathbf{r})$  and  $\mathbf{L}(\mathbf{r})$  given by

$$\mathbf{M}(\mathbf{r}) = \nabla \times \mathbf{c}\Psi(\mathbf{r}), \quad \mathbf{N}(\mathbf{r}) = \frac{1}{k} \nabla \times \mathbf{M}(\mathbf{r}), \quad \mathbf{L}(\mathbf{r}) = \Psi(\mathbf{r}), \quad (23)$$

where  $\mathbf{c}$  is a pilot vector. Here,  $\mathbf{M}(\mathbf{r})$  and  $\mathbf{N}(\mathbf{r})$  are divergence-free and orthogonal.  $\mathbf{L}(\mathbf{r})$  is curl-free and orthogonal with  $\mathbf{M}(\mathbf{r})$  and  $\mathbf{N}(\mathbf{r})$ . Then, an arbitrary electromagnetic field can be described with  $\mathbf{M}(\mathbf{r})$  and  $\mathbf{N}(\mathbf{r})$  and  $\mathbf{L}(\mathbf{r})$  [21].

In spherical coordinates, we can obtain the solution to (22) for unbounded media as

$$\Psi(k, \mathbf{r}) = z_n^{(c)}(kr) Y_{nm}(\theta, \phi), \quad (24)$$

where  $z_n^{(c)}$  is the radial function and  $Y_{nm}(\theta, \phi)$  is the complex spherical harmonic function. The radial function  $z_n^{(c)}$  is determined by an upper index ( $c$ ) as one of the following functions:

$$z_n^{(1)}(kr) = j_n(kr) \quad (\text{spherical Bessel function}) \quad (25)$$

$$z_n^{(2)}(kr) = n_n(kr) \quad (\text{spherical Neumann function}) \quad (26)$$

$$z_n^{(3)}(kr) = h_n^{(1)}(kr) = j_n(kr) + jn_n(kr) \quad (\text{spherical Hankel function of the first kind}) \quad (27)$$

$$z_n^{(4)}(kr) = h_n^{(2)}(kr) = j_n(kr) - jn_n(kr) \quad (\text{spherical Hankel function of the second kind}), \quad (28)$$

where  $c = 1$  and  $c = 2$  indicate standing waves and  $c = 3$  and  $c = 4$  indicate an outgoing wave and incoming wave, respectively. The complex spherical harmonic function  $Y_{nm}(\theta, \phi)$  is expressed as

$$Y_{nm}(\theta, \phi) = C_{nm} P_n^m(\cos \theta) e^{jm\phi} = \sqrt{\frac{(n-m)!(2n+1)}{(n+m)!4\pi}} P_n^m(\cos \theta) e^{jm\phi}, \quad (29)$$

where  $P_n^m(\cos \theta)$  is the associated Legendre polynomial,  $C_{nm}$  is a normalization factor,  $n = 0, 1, \dots$  and  $m = -n, -n+1, \dots, 0, 1, \dots, n-1, n$  [10]. The complex spherical harmonic function  $Y_{nm}(\theta, \phi)$  can be defined by the real combinations of the azimuth functions as follows [22]:

$$Y_{\sigma nm}(\theta, \phi) = \sqrt{2} C_{nm} P_n^m(\cos \theta) \begin{cases} \cos m\phi \\ \sin m\phi \end{cases}, \quad (30)$$

where  $m = 0, 1, \dots, n-1, n$  and  $\sigma = e, o$  (even or odd in  $\phi$ ).

The normalized vector spherical harmonics  $\mathbf{A}_{\sigma nm}(\hat{\mathbf{r}})$  can be defined with using the real spherical harmonic function  $Y_{\sigma nm}(\hat{\mathbf{r}}) = \hat{\mathbf{r}} Y_{\sigma nm}(\theta, \phi)$  as follows [11]:

$$\begin{cases} \mathbf{A}_{1\sigma nm}(\hat{\mathbf{r}}) = \frac{1}{\sqrt{n(n+1)}} \nabla \times \hat{\mathbf{r}} Y_{\sigma nm}(\hat{\mathbf{r}}), \\ \mathbf{A}_{2\sigma nm}(\hat{\mathbf{r}}) = \frac{1}{\sqrt{n(n+1)}k} \frac{1}{r} \nabla Y_{\sigma nm}(\hat{\mathbf{r}}), \\ \mathbf{A}_{3\sigma nm}(\hat{\mathbf{r}}) = \hat{\mathbf{r}} \nabla Y_{\sigma nm}(\hat{\mathbf{r}}). \end{cases} \quad (31)$$

where  $n = 0, 1, \dots$ , and  $m = 0, 1, \dots, n-1, n$  and  $\sigma = e, o$ . In this case, (23) may be modified by

$$\begin{aligned} \mathbf{M}_{\sigma nm}(k, \mathbf{r}) &= \nabla \times \mathbf{r} z_n^{(c)}(kr) Y_{\sigma nm}(\theta, \phi), \\ \mathbf{N}_{\sigma nm}(k, \mathbf{r}) &= \frac{1}{k} \nabla \times \nabla \times \mathbf{r} z_n^{(c)}(kr) Y_{\sigma nm}(\theta, \phi), \\ \mathbf{L}_{\sigma nm}(k, \mathbf{r}) &= \frac{1}{k} \nabla z_n^{(c)}(kr) Y_{\sigma nm}(\theta, \phi). \end{aligned} \quad (32)$$

Because of the orthogonal relationship, furthermore, an arbitrary field  $\mathbf{E}(\mathbf{r})$  can be represented as



$$\mathbf{E}(\mathbf{r}) = \sum_{\sigma=e, o} \sum_{n=1}^{\infty} \sum_{m=0}^m \int_0^{\infty} dk k^2 [a_{\sigma nm}(k) \mathbf{M}_{\sigma nm}(k, \mathbf{r}) + b_{\sigma nm}(k) \mathbf{N}_{\sigma nm}(k, \mathbf{r}) + c_{\sigma nm}(k) \mathbf{L}_{\sigma nm}(k, \mathbf{r})]. \quad (33)$$

From (25) and (32), the outgoing vector waves  $\boldsymbol{\psi}_{\tau\sigma nm}$  are expressed as

$$\begin{cases} \boldsymbol{\psi}_{1\sigma nm}(\theta, \phi) = \nabla \times \mathbf{r} h_n^{(1)}(kr) Y_{\sigma nm}(\theta, \phi), \\ \boldsymbol{\psi}_{2\sigma nm}(\theta, \phi) = \frac{1}{k} \nabla \times \nabla \times \mathbf{r} h_n^{(1)}(kr) Y_{\sigma nm}(\theta, \phi), \end{cases} \quad (34)$$

These spherical vector waves may become the solutions to the vector wave functions  $\mathbf{M}_{\sigma nm}$  and  $\mathbf{N}_{\sigma nm}$ . The outgoing spherical vector waves can be described approximately as

$$\boldsymbol{\psi}_{\tau\sigma nm}(\theta, \phi) = (-j)^{n+2-\tau} \frac{\exp jkr}{kr} \mathbf{A}_{\tau\sigma nm}(\hat{\mathbf{r}}) + o((kr)^{-1}), \quad \tau = 1, 2. \quad (35)$$

The far field is the outgoing spherical vector waves when the  $r$  is a very large value relatively to the wavelength. Therefore, the general expression of the far field can be decomposed approximately as

$$\mathbf{F}(\hat{\mathbf{r}}) = \sum_{\alpha} (-j)^{n+2-\tau} f_{\alpha} \mathbf{A}_{\alpha}(\hat{\mathbf{r}}), \quad (36)$$


where multi-index  $\alpha = 2(n(n+1) - 1 + (-1)^s m) + \tau$  and  $s = 1, 2$  for  $\sigma = e, o$ , respectively.

## Author details

Daehee Park\* and Dong-Ho Cho  
 Korea Advanced Institute of Science and Technology (KAIST), Republic of Korea

\*Address all correspondence to: [indeener@gmail.com](mailto:indeener@gmail.com)

## IntechOpen

© 2018 The Author(s). Licensee IntechOpen. This chapter is distributed under the terms of the Creative Commons Attribution License (<http://creativecommons.org/licenses/by/3.0>), which permits unrestricted use, distribution, and reproduction in any medium, provided the original work is properly cited. 

## References

- [1] Paulraj A, Nabar R, Gore D. Introduction to Space-time Wireless Communications. United Kingdom: Cambridge University Press; 2003
- [2] Larsson EG, Edfors O, Tufvesson F, Marzetta TL. Massive MIMO for next generation wireless systems. IEEE Communications Magazine. 2014;**52**(2): 186-195
- [3] Ji H, Kim Y, Lee J, Onggosanusi E, Nam Y, Zhang J, et al. Overview of full-dimension MIMO in LTE-advanced pro. IEEE Communications Magazine. 2017; **55**(2):176-184
- [4] Andrews MR, Mitra PP, et al. Tripling the capacity of wireless communications using electromagnetic polarization. Nature; 2001;**409**(6818): 316-318
- [5] Poon AS, David N. Degree-of-freedom gain from using polarimetric antenna elements. IEEE Transactions on Information Theory. 2011;**57**(9): 5695-5709
- [6] Glazunov AA, Zhang J. Some examples of uncorrelated antenna radiation patterns for MIMO applications. In: PIERS Proceedings. 2011. pp. 598-602
- [7] Jeon W, Chung SY. The capacity of wireless channels: A physical approach. In: Information Theory Proceedings (ISIT), 2013 IEEE International Symposium on IEEE; 2013. pp. 3045-3049
- [8] Mohammed J. Optimal null steering method in uniformly excited equally spaced linear arrays by optimising two edge elements. Electronics Letters. 2017; **53**(13):835-837
- [9] Mohammed JR. Element selection for optimized multi-wide nulls in almost uniformly excited arrays. IEEE Antennas and Wireless Communication Letters Digital Object Identifier. 2018; **10**:629-632
- [10] Hansen JE. Spherical Near-field Antenna Measurements. Vol. 26. United Kingdom: Stevenage Herts England Peter Peregrinus Ltd IEE Electromagnetic Waves Series; 1988
- [11] Boström A, Kristensson G, Ström S. Transformation properties of plane, spherical and cylindrical scalar and vector wave functions. Acoustic, Electromagnetic and Elastic Wave Scattering, Field Representations and Introduction to Scattering. 1991;**1**: 165-210
- [12] Gustafsson M, Nordebo S. Characterization of MIMO antennas using spherical vector waves. IEEE Transactions on Antennas and Propagation. 2006;**54**(9):2679-2682
- [13] Glazunov AA, Gustafsson M, Molisch AF, Tufvesson F, Kristensson G. Spherical vector wave expansion of Gaussian electromagnetic fields for antenna-channel interaction analysis. IEEE Transactions on Antennas and Propagation. 2009;**57**(7):2055-2067
- [14] Glazunov A. Expansion of the kronecker and keyhole channels into spherical vector wave modes. Antennas and Wireless Propagation Letters. 2011; **10**:1112-1115
- [15] Alayon Glazunov A. A survey of the application of the spherical vector wave mode expansion approach to antenna-channel interaction modeling. Radio Science. 2014;**49**(8):663-679
- [16] Chiu CY, Yan JB, Murch RD, Yun JX, Vaughan RG. Design and implementation of a compact 6-port

antenna. *IEEE Antennas and Wireless Propagation Letters*. 2009;**8**:767-770

[17] Park D, Cho DH. Analysis of pattern gain of compact directional 16-port antenna. *IEEE Antennas and Wireless Propagation Letters*. 2015;**14**:902-905

[18] Capobianco AD, Pigozzo FM, Assalini A, Midrio M, Boscolo S, Sacchetto F. A compact MIMO array of planar end-fire antennas for WLAN applications. *IEEE Transactions on Antennas and Propagation*. 2011;**59**(9): 3462-3465

[19] Tse D, Viswanath P. *Fundamentals of Wireless Communication*. United Kingdom: Cambridge University Press; 2005

[20] Glazunov AA, Gustafsson M, Molisch AF, Tufvesson F. Physical modelling of multiple-input multiple-output antennas and channels by means of the spherical vector wave expansion. *IET Microwaves, Antennas and Propagation*. 2010;**4**(6):778-791

[21] Chew WC. *Waves and Fields in Inhomogeneous Media*. United States: IEEE Press; 1995

[22] Whittaker ET, Watson GN. *A Course of Modern Analysis*. United States: Cambridge University Press; 1996



# Smart Antenna Systems Model Simulation Design for 5G Wireless Network Systems

*Vincenzo Inzillo, Floriano De Rango, Luigi Zampogna and Alfonso A. Quintana*

## Abstract

The most recent antenna array technologies such as smart antenna systems (SAS) and massive multiple input multiple output (MIMO) systems are giving a strong increasing impact relative to 5G wireless communication systems due to benefits that they could introduce in terms of performance improvements with respect to omnidirectional antennas. Although a considerable number of theoretical proposals already exist in this field, the most common used network simulators do not implement the latest wireless network standards and, consequently, they do not offer the possibility to emulate scenarios in which SAS or massive MIMO systems are employed. This aspect heavily affects the quality of the network performance analysis with regard to the next generation wireless communication systems. To overcome this issue, it is possible, for example, to extend the default features offered by one of the most used network simulators such as Omnet++ which provides a very complete suite of network protocols and patterns that can be adapted in order to support the latest antenna array systems. The main goal of the present chapter is to illustrate the improvements accomplished in this field allowing to enhance the basic functionalities of the Omnet++ simulator by implementing the most modern antenna array technologies.

**Keywords:** smart antenna systems, planar array, massive MIMO, Omnet++

## 1. Introduction

Since the start of wireless communications, concerning to the network node physical layer, there are two main types of antenna which can be used as a way to make a certain behavior on transmission/reception: omnidirectional antennas which radiates and receives equally in all directions, and directional antennas which have the capability to radiate in a specific direction. Omnidirectional approaches can be straight and detrimentally impact on spectral efficiency of the system, restricting frequency reuse [1]. These limitations force system designers and network planners to develop progressively advanced and costly remedies. Lately, the requirements of broadcast antenna technology on the quality, capacity, and coverage of wireless systems have motivated the development in the fundamental design and role of the antenna in a wireless system. In pervasive environments, such as mobile ad hoc network (MANET) or wireless sensor networks, employing an omnidirectional approach is hard and an inconvenient way to create efficient

systems, because of the high burden of power of network nodes [2] that may result in destructive phenomena such as low battery depletion and interference. A single antenna may also be built to have certain fixed preferential transmission and reception directions to maximize its energy consumption in a specific direction conserving power in other directions [3]. Using directional antenna could lead to several advantages, in terms of reduction of packet delay or improvement of the overall routing process [4]. In wireless communications, when a single antenna is utilized both to the transmitter and receiver we talk about single input, single output (SISO) [5] systems. Therefore, nowadays, with regard to the latest antenna technologies, the concept of smart antenna systems has spread. SAS are intelligent systems equipped with high efficiency data processing unit. This sort of systems can boost the coverage area and the capability of a radio communication system. The coverage area is simply the area where the communication link between a mobile and the base station can be performed. The capability is a way of measuring the amount of users a system can support in certain area. A smart antenna system generally combines an antenna array with a digital signal processing capacity to transmit and receive in an adaptive, spatial manner. Quite simply, such a system can quickly change the directionality of its radiation patterns in response to its environment. This may considerably increase the performance characteristics (such as capacity) of a wireless system. The employment of SAS in wireless mobile environments allows a much more reliable medium utilization with regards to the classical omnidirectional strategy. For instance, spatial division multiple access (SDMA) attempts to raise the capacity of a system. Generally, smart antennas get into three major categories: single input, multiple output (SIMO), multiple input, single output (MISO), and multiple input, multiple output (MIMO). In SIMO technology, one antenna is used at the source, and two or more antennas are used at the destination. In MISO technology, several antennas are used at the transmitter, and one antenna is utilized at the destination. In MIMO technology, multiple antennas are used at both source and destination.

**Figure 1** illustrates an example of SISO and MIMO systems. In the SISO case, either the transmitter or the receiver uses a single antenna for the communication process; while in the MIMO, an antenna array is employed. In literature, it has been demonstrated how the use of directional antennas and the most recent smart antenna systems (SAS) technology is capable of significantly allowing high quality of service (QoS) requirements in spite of the omnidirectional systems that foresee

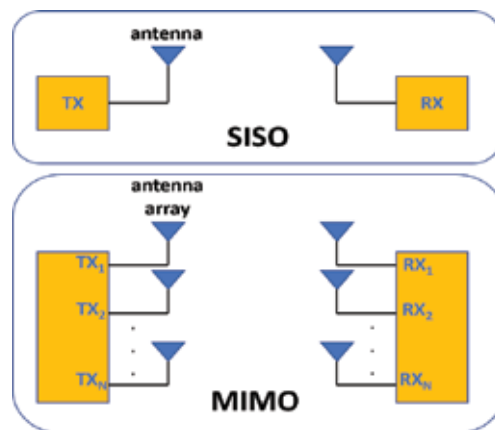


**Figure 1.**  
SISO and MIMO structure example.

limited functionalities [6, 7]. However, these solutions are unlikely to satisfy the requirements for 5G wireless communication systems technology. For this purpose, the massive MIMO technology has been proposed as efficient solution for satisfying the requirements for 5G that certainly include very high antenna gain and very high data rate in order to achieve huge system performance [8–10]. The term massive, means that this kind of systems employs a large number of antenna elements (at least 50 antennas) in the hardware architecture; indeed, relating to the modern wireless networks, for achieving high communication benefits in terms of throughput, we need for a massive number of elements that is not less than 70–80 antennas [11]. This is mainly due to the fact that, theoretically, as the number of elements improves, the overall gain of the system also increases, and in fact, each single antenna element contributes to enhance the total gain. More specifically, from the antenna array theory, it is known that the overall gain is affected by the single element factor as well as the array factor, and this gain increases with the number of antenna elements. The massive MIMO are strongly recommended for beamforming environments by the most recent IEEE802.11n and IEEE802.11ac standards. Remember that we refer to a beamforming wireless network context when communications between nodes occur through the beamforming process; the beamforming is defined as the capability of a node to scan and drive the antenna beam pattern toward a certain area or a set of directions. One of the most critical aspects in wireless communication environments is represented by the fact of using an adequate network simulator that is able to well emulate and reproduce an appropriate real scenario. Unfortunately, most of the existing network simulators do not provide any support for directional and asymmetrical communications, and thus also for SAS and MIMO technology. In this field, only an extremely limited amount of network simulators allow to emulate these very complex technologies. Unfortunately, in such cases, with regard to these network simulators, the cost of the license allowing the end user to access to the 5G package modules could result very expensive [12]. In this chapter, we present a set of features extending the default functionalities provided by one of the most used open source network simulator, that is the Omnet++ simulator, with the goal to illustrate how it is possible to actualize the existing simulation instruments to be suitable also for 5G wireless network communication environments. The chapter is organized as follows: Sections 2 and 3 provide a theoretical overview about SAS and massive MIMO, respectively, while Sections 4 and 5 explain the implementation strategies in Omnet++ related in the aforementioned technologies.

## 2. Smart antenna systems

As mentioned, SAS are intelligent systems that allow a good SDMA processing [13, 14]; examples of SAS are: digital beamforming systems, adaptive antenna systems, phased array, and others. Smart antennas are customarily categorized, however, as either switched beam or adaptive array systems. There could be a distinction between two major categories of smart antennas in terms of the operation mode:

- **Switched beam:** A finite number of fixed and predefined patterns without channel feedback.
- **Adaptive array:** An infinite number of patterns that are adjusted in real time based on such parameters, for example, channel noise conditions.

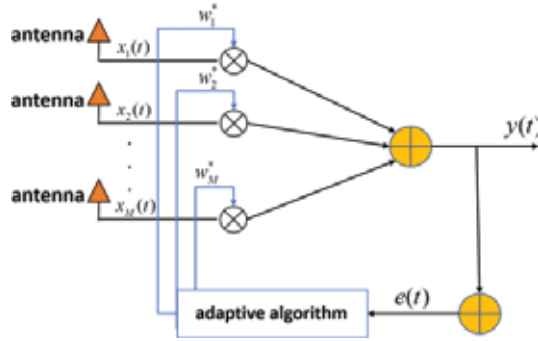


**Figure 2.**  
SAS basic operation principle.

Switched beam antenna systems form multiple fixed beams with high sensitivity in particular directions. These antenna systems detect signal strength, choose from one of several predetermined, fixed beams, and switch from one beam to another as the mobile moves throughout an area. So, they produce a static fixed beam that could be electronically controlled. Adaptive antenna technology, instead, uses adaptive algorithm because of its ability to effectively locate and track various types of signals to dynamically minimize interference and maximize the intended signal reception. In this case, produced beam is variable and adapts itself depending on transmission channel conditions and a weight array that dynamically varies in time. In this context, the spatial structure is used to estimate the direction of arrive (DOA) or angle of arrive (AOA) by nodes. However, both systems attempt to increase gain according to the location of the user. The basic SAS operation principle can be summarized by the following figure.

In **Figure 2**, inputs  $x_1(t), \dots, x_M(t)$  are multiplied by elements of a weight vector  $\bar{W} = [w_1, w_2, \dots, w_M]$  that varies according to an adaptive algorithm (used only in the adaptive array version);  $y(t)$  is the output, while  $e(t)$  denotes the error; all terms are defined in functions of the discrete time  $t$ . Instead, when a switched beam approach is employed, because any adaptive algorithm is executed, the weight array can be considered missing or simply as a constant. Based on the kind of produced geometry pattern, SAS can be categorized into different ways. The most common categories include, rectangular, hexagonal, and the circular arrays. However, in 5G technology, the antenna arrays should be adaptive, and it is required that they have an adaptive capability to point the main beam toward the desired direction and steer the nulls toward the undesired interfering directions. In all cases, this adaptive mechanism should be optimized to get best performance or maximum signal to interference plus noise ratio (SINR) at the system's output [15–17].

### 3. The massive MIMO systems

Massive MIMO is a rising technology that considerably enhances the basic MIMO features. The term massive MIMO is referred to the whole of systems that use antenna arrays with at least few hundred antennas, simultaneously serving multiple terminals in the same time frequency resource.

**Figure 3** illustrates the basic operation principle of a massive MIMO; few users are served from a macrodevice (for example a rectangular array) having a large number of base stations (antennas). Generally, massive MIMO is an instrument that allows to enable the development of future broadband (fixed and mobile) networks which will satisfy special requirements in terms of energy-efficiency, security,





**Figure 3.**  
*Massive MIMO operation principle.*

and robustness. Structurally, a massive MIMO system consists of a group of small (relatively) antennas, supplied from an optical or electric digital bus that operates simultaneously related to a certain task. Massive MIMO, as well as the SAS systems are able to well exploit the spatial division multiple access (SDMA) allowing for an efficient resource channel utilization, both on the uplink and the downlink [18, 19]. In conventional MIMO systems, like the long-term evolution (LTE), the base station transmits waveforms depending on terminals channel response estimation, and then these responses are quantized by some processing units and sent out back to the base station. Fundamentally, this is not possible in massive MIMO systems, especially concerning high-mobility environments [20], because optimal downlink pilots should be mutually orthogonal between the antennas. Therefore, in spite of the difficult hardware and designing implementation, these systems are becoming increasingly prevalent in the modern applications due to the great benefits that could introduce; in particular, massive MIMO can increase the wireless channel capacity up to 10 times and the radiated energy-efficiency up to 100 times with respect to the traditional LTE systems. This translates into higher gains and higher performance. However, the employment of these systems entails a series of issues that should be properly considered, for example, the interferences between terminals increase as the data rate increases. Other issue is the fact that terminals consume a lot of energy during the communication process in spite of the well SDMA exploitation. Finally, the difficulty of designing a system of limited size improves proportionally with the increasing of the number of antennas in the system. For this reason, it is necessary to find a trade-off between the number of elements and the requirements. Although there exist several kinds of massive MIMO systems depending on the geometry pattern, in this chapter, only the planar massive MIMO technology is exposed. We use the term planar to indicate that the array can scan the beam along the elevation plane  $\theta$  and the azimuth plane  $\phi$  as opposed to the linear arrays that scan the main beam only along  $\theta$  or  $\phi$  [21]. Planar arrays offer more gain and lower sidelobes than linear arrays at the expense of using more elements [22].

### 3.1 Planar massive MIMO

From an architectural point of view, a massive MIMO is structured depending on the geometry pattern that is able to form. There exist several design configurations that usually are function of the kind of application to which these systems are destined. Anyway, in this chapter, we consider three different types of planar antenna arrays: the uniform rectangular planar array (URPA), the hexagonal planar array (HPA), and the circular planar array (CPA). Substantially, the term uniform means that the weight parameters  $w_1, w_2, \dots, w_M$  are all unity, thus it cannot be readjusted as mentioned earlier in Section 2, **Figure 2**. The following subsections synthesize the main feature of the mentioned configurations.

### 3.1.1 Massive MIMO URPA

The uniform rectangular planar array technology is the most simple planar massive MIMO configuration presenting a 2D (two-dimensional) element plane disposition. The geometry pattern, in this case, can be considered as a two-dimensional matrix within which the antenna elements are placed.

**Figure 4** illustrates an example of massive MIMO URPA configuration. Basically, a URPA is a two-dimensional matrix filled with a certain number of antenna elements (the circles in the figure) both along the x- and y-axis; these antenna elements are equally spaced between any successive pair of elements and this spacing is usually expressed in wavelengths. If we denote the number of elements placed on the x-axis with  $M$  (the rows of the matrix) and with  $N$  the number of antennas lying in the y-axis (the columns of the matrix), the total number of elements of the URPA is given by [22]:

$$NumElem = M \times N \quad (1)$$

where  $M$  and  $N$  are arbitrary integers typically higher than 1. In the first versions of the URPA,  $M$  and  $N$  were identical and limited to 8; in the modern application,  $M$  and  $N$  are commonly different and chosen between 8 and 12. In general, the radiation field formed by the antenna elements (known also with the term *element factor*) is expressed as:

$$E_m(r, \theta, \phi) = A \times f(\theta, \phi) \frac{e^{-jkr}}{r} \quad (2)$$

In Eq. (2),  $A$  is the nominal field amplitude,  $f(\theta, \phi)$  is the radiation field pattern of the element, and  $r$  is the radial distance between the element and the observation point, which highlights the decrease of the field in function of the distance. According to the pattern multiplication principle, the antenna array total electrical field can be expressed as:

$$E_{TOT} = E_m \times AF(\theta, \phi) \quad (3)$$

In the case of URPA, the array factor equation is very similar to the ULA with the only difference that is designed by considering two dimensions [15, 22]:

$$AF_{URPA}(\theta, \phi) = \left[ \frac{\sin\left(\frac{M\Psi_M}{2}\right)}{\sin\left(\frac{\Psi_M}{2}\right)} \right] \left[ \frac{\sin\left(\frac{N\Psi_N}{2}\right)}{\sin\left(\frac{\Psi_N}{2}\right)} \right] \quad (4)$$

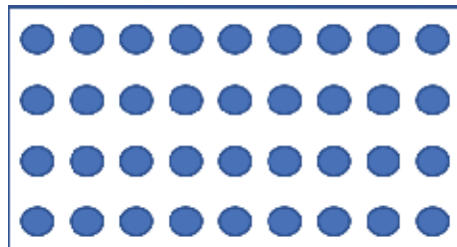


**Figure 4.** Massive MIMO URPA example.

With:

$$\begin{aligned}\psi_M &= kd \sin\theta \cos\phi + \beta_M, & \psi_N &= kd \sin\theta \sin\phi + \beta_N \\ \beta_M &= -kd \sin\theta_0 \cos\phi_0, & \beta_N &= -kd \sin\theta_0 \sin\phi_0\end{aligned}\quad (5)$$

The terms  $\psi_M$  and  $\psi_N$  indicate the array phase along the x- and y-axis, respectively, while the terms  $\beta_M$  and  $\beta_N$  denote the scanning steering factors along x and y in function of the steering angle; finally,  $\phi_0$  is the elevation angle relative to the steering angle  $\theta_0$ . Please observe that the array factor expression related to Eq. (6) is not normalized with respect to  $M$  and  $N$ . The overall gain of the URPA is expressed by the following [21]:

$$G(\theta, \phi) = \frac{4\pi |f(\theta, \phi) AF(\theta, \phi)|^2}{\int_{\phi=0}^{2\pi} \int_{\theta=0}^{\pi} |f(\theta, \phi) AF(\theta, \phi)|^2 \sin\theta \, d\theta d\phi} \quad (6)$$

Equation (6) is the generic expression of the gain valid for all antenna types and is function of the element factor and the array factor. If the antenna elements are isotropic, we have  $f(\theta, \phi) = 1$  and the gain becomes [23]:

$$G(\theta, \phi) = D(\theta, \phi) = \frac{4\pi |AF(\theta, \phi)|^2}{\int_{\phi=0}^{2\pi} \int_{\theta=0}^{\pi} |AF(\theta, \phi)|^2 \sin\theta \, d\theta d\phi} \quad (7)$$

Equation (7) also expresses the directivity of the antenna; thus, from antenna array theory, it is possible to obtain the expression which corresponds to the maximum gain in case of isotropic antenna elements [23]:

$$G_{MAX}(\theta, \phi) = \frac{4\pi \times |AF_{MAX}(\theta, \phi)|^2}{\int_{\phi=0}^{2\pi} \int_{\theta=0}^{\pi} |AF_{MAX}(\theta, \phi)|^2 \sin\theta \, d\theta d\phi} \quad (8)$$

where  $|AF_{MAX}(\theta, \phi)|^2$  is the square modulus related to the maximum value of the array factor.

### 3.1.2 Massive MIMO HPA

An HPA configuration usually consists of  $M$  hexagonal rings, each one having a total number of  $6m$ , where  $m$  is the  $m$ th ring of the system; the antenna elements are uniformly distributed in the hexagonal side (**Figure 5**).

In case of isotropic elements, because the excitation amplitude is set to 1, the array factor can be expressed as the following expressions [24]:

$$AF_{UHPA} = \sum_{m=-M}^M e^{j\pi[mv_y - \frac{N}{2}v_x - \frac{m}{2}v_x]} \sum_{n=0}^N e^{j\pi n v_x} \quad (9)$$

$$N = 2M - |m|; \quad v_x = \sin\theta \cos\phi; \quad v_y = \sin\theta \sin\phi \quad (10)$$

Note that in Eq. (9), the dependence on  $\theta$  and  $\phi$  is omitted and furthermore the steering factor for beam scanning is not considered, while  $v_x$  and  $v_y$  denote the planar vectorial components along the x- and y-axis, respectively. The maximum theoretical gain is the same of the URPA case, except from the array factor term.

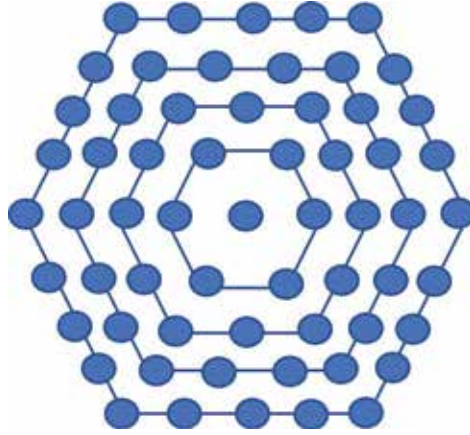


**Figure 5.**  
Massive MIMO HPA example.

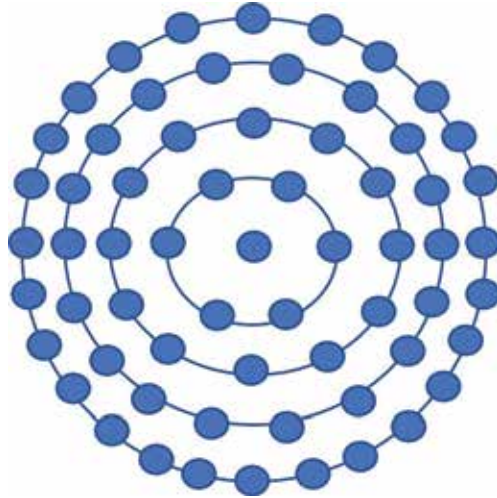


**Figure 6.**  
Massive MIMO CPA example.

### 3.1.3 Massive MIMO CPA

The geometry structure of a circular planar array is very similar to a HPA, except from the fact that the hexagonal ring is replaced by a circular ring. As assumed for the HPA, we can consider the widespread configuration having  $6m$  antenna elements uniformly placed around the circular edge of the  $m$ th radius.

**Figure 6** illustrates the CPA configuration that consists of a certain number of circular rings having same center but different radius with the antenna elements placed on the circumference of each ring. Because a CPA is a particular case of the hexagonal structure, the array factor equation is quite similar to the HPA expression. In case of isotropic elements, the array factor could be expressed by the following [25, 26]:

$$AF_{UCPA} = 1 + \sum_{m=1}^M \sum_{n=1}^{6m} e^{-j(\pi m \sin \theta \cos(\phi - \phi_n) + \beta_M)} \quad (11)$$

$$\phi_n = \frac{2\pi n}{6m} = \frac{\pi n}{3m}; \quad \beta_M = \sin \theta_0 \cos(\phi_0 - \phi_n) \quad (12)$$

Equation (11) considers the possibility to scan the beam through the use of the term  $\beta_M$ , which is a function of the steering elevation  $\phi_0$ . The  $M$  and  $\theta_0$  terms are already defined in the previous subsection. From the theory, it is also known that the steering vector and the array factor are closely related to the number of antenna elements, the array configuration, and the antenna elements excitation (which in this case is unitary in amplitude). It is easy to conclude that the maximum achievable gain is the same of the HPA and URPA case. However, as verified for the HPA, the total number of elements is usually an odd number and depends on the number of circular ring in the structure.

#### 4. SAS design and implementation on Omnet++

Omnet++ [27] is a discrete event simulation environment that provides component architecture for models. Components (modules) are programmed in C++, and then assembled into larger components and models using a high-level language (NED). There are several reasons for using Omnet++ for implementing a SAS or a Massive MIMO. Firstly, it is an open source instrument allowing the reusability of models for free. Yet, it provides a full set of features and protocols especially relating to wireless network; hence, the end user developer can create new modules or extend the default models quite comfortably. Nevertheless, it provides an extremely intuitive user interface for both in developing and simulations. Unfortunately, by default, Omnet++ does not support asymmetrical communication between nodes. For enabling the simulator to support directional communications and so the SAS, some modifications on the original source code are required. Let us suppose that we aim to implement the most simple SAS technology, that is the switched beam, the first step needed is to design the module. For example, a phased array system could be implemented. In our case, we created a new directive antenna model and the relative module called *PhasedArray* that implements all features of a phased array system [28]. The main definition of the class could be synthesized as follows (Figure 7).

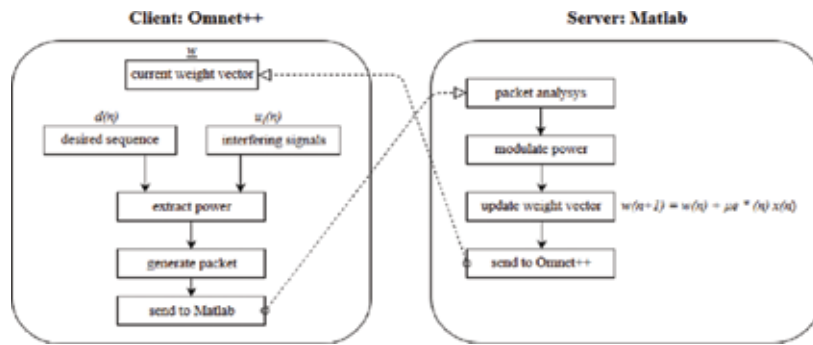
The function *initialize* initializes the module in the simulation setup. Basically, the function *computeGain*, as the name suggests, computes the antenna gain; in the omnidirectional case, this function simply returns 1. This function could be modified by implementing the expression defined by Eq. (2). The second step concerns the modifications related to the mobile node module used in Omnet, that is, the *StandardHost* module.

Figure 8 illustrates the typical *StandardHost* structure which consists of sub-modules organized according to the TCP/IP layer stack. In this regard, several modifications in the physical layer are required. The physical layer defines the functions relating to channel model propagation, power management, and modulation. More specifically, the *ScalarAnalogModelBase* class implements the channel propagation

PhasedArray
+ Attribute 1 : distance
+ Attribute 2 : thetazero
- Attribute 3 : frequency
- Attribute 4 : length
+ void Initialize ( int stage)
+ computeGain ( EulerAngles direction ) : double
+ setThetazero ( double thetazero ) : double

Figure 7.  
*PhasedArray* main parameters class definition.





**Figure 10.**  
 Co-simulation for SAS adaptive array.

to provide for a co-simulation. The co-simulation, for instance, can be performed using any combination of network simulators and Matlab [29]. Matlab enhances the working of network, simulating tool, and increases the speed of testing and processing by using different toolboxes. In this case, it is possible to divide the overall task, that is, the simulation into two subtasks. The first subtask is handled by Omnet++ that provides for the network scenario; while the second subtask is managed by Matlab that performs the adaptive algorithm operations [30].

**Figure 10** represents the communication process between the two parts based on a client-server paradigm. Omnet++ executes the simulation and dynamically sends the physical parameters (the power and noise in this case) related to a certain communication between couple of nodes to Matlab; Matlab executes the adaptive algorithm (the least mean algorithm in this case) based on the data received in input, computes the updated weighted vector, and sends backwards the data to Omnet++. The communication between the two parts can be easily realized by using TCP sockets.

## 5. Massive MIMO design and implementation on Omnet++

The latest release of the Omnet++ simulator (the 5.3 version), does not offer a support to asymmetrical communications and does not implement the latest IEEE802.11ac standard. More specifically, Omnet++ offers a complete support for 802.11b/g and the most recent 802.11n standard, but does not support the specifications related to the 802.11ac standard. Furthermore, these features are not sufficient for emulating the latest massive MIMO technologies in the simulator. In fact, the maximum data rate supported in the *radio* module used in the current latest version of Omnet++ is 54 Mbps, along with a 64-QAM modulation, according to the 802.11n specifications. In view of these issues, it is possible to extend the Omnet++ features both by providing a full 802.11ac radio environment and a new massive MIMO antenna module suitable for 5G wireless network environments operating according to the IEEE802.11ac.

### 5.1 IEEE802.11ac implementation

The first step consists of the implementation of the 802.11ac standard in the physical modules of Omnet++. Basically, this process involves modifications as regards two microlayers: the *error model* and the *modulation*. The error model determines the computation of the bit error rate (BER) curves and the error probability in function of the data rate. Obviously, as already stated, the current error models

are determined by considering the maximum data rate of 54 Mbps. For this reason, this aspect should be fixed in order to design a support of data rates in the order of the Gbps. The modulation is the feature that offers the possibility to achieve the data rate values specified for VHT (very high throughput) and in the current latest version Omnet++ is limited to 64-QAM; this aspect determines the data rate upper-bound in the simulations. The family of modules related to the error model and modulation are contained in the *physicallayer* package.

**Figure 11** illustrates the structure of the *physicallayer* package. The package consists of a remarkable number of subpackages, each one determining a feature for the physical layer, observing that the error model and the modulation microlayers are contained in this package along with main modeling channel attributes, such as the propagation and the pathloss management. Thus, in order to understand updates introduced for implementing the IEEE802.11ac standard, the following figures show a block diagram including the main Omnet++ classes (known also as *modules*) involved in the modification process.

**Figure 12** represents the module block diagram related to the implementation of the VHT features for the transmitter at physical layer. Each class/module is represented by a rectangle, while the dashed-line arrows and the continued-line arrows indicate the *use* and the *inheritance* relationship, respectively. The *Ieee80211Radio* module uses the *Ieee80211TransmitterBase* module that is defined by the following NED (network description language) code lines:

In **Listing 1**, the main parameters of the *Ieee80211TransmitterBase* module are illustrated. The *opMode* parameter indicates the kind of IEEE802.11 standard that is determined by a lower-case letter. In this regard, we modified the default code by adding the ac operation mode. Note that also the 5-GHz frequency band configurations have been added. The transmitter uses the class *Ieee80211CompliantBands* for retrieving the available bands and the *Ieee802ModeBase* class obtaining the operation mode. This latest class inherits the parameters offered by the classes *Ieee80211VHTMode* and *Ieee80211VHTCode* that contains the new data rate values specified by the 802.11ac standard according to the VHT specifications. For this purpose, we added all the data rate values provided by the standard by varying the carrier frequency and the number of spatial streams. The *Ieee80211VHTCode* is the module that computes the error probability functions depending on the kind of modulation used in simulation. A similar block diagram could be designed for the receiver.

In the diagram of **Figure 13**, it is possible to analyze the hierarchical relationships at the receiver. It is important to highlight that the error model is mainly used by the receiver rather than the transmitter. Omnet++ uses some of the error models offered from the NS3 (Network Simulator 3) simulator that are the Yans and the

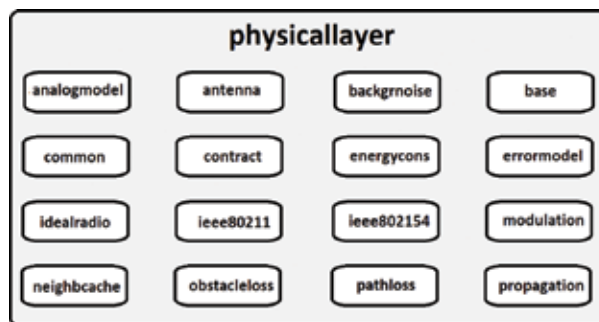


**Figure 11.** *Physicallayer Omnet++ package structure.*



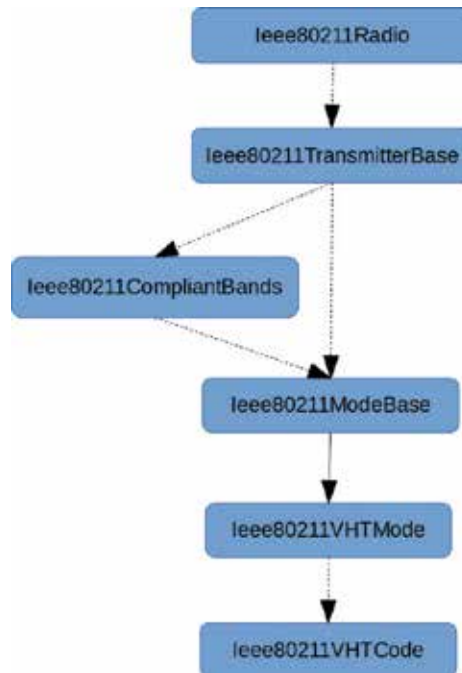


**Figure 12.**  
 VHT implementation in the transmitter.

**Listing 1:** *ieee80211TransmitterBase.ned* definition

```

1 module ieee80211TransmitterBase ...
2 parameters:
3   string opMode @enum{"a", "b", "g(exp)", "g(mixed)", "n(mixed)",
4     "-2.4GHz)", "p", "ac"}
5   string bandName @enum{"2.4 GHz", "5 GHz", "5 GHz+20 MHz", "5
6     GHz+40 MHz", "5 GHz+80 MHz", "5 GHz+160 MHz"}
7   int channelNumber;
8   modulation = default("BPSK");
    
```

**Listing 1.**  
*ieee80211TransmitterBase.ned* definition.

Nist models [31]. Basically, these error modules compute the BER probability values in function of the modulation. For enabling the 802.11ac, we extended the default code of Omnet++ by adding the BER computation functions for 256, 512, and 1024-QAM modulation.

**Listing 2** contains a part of the full code of the *Ieee80211NistErrorModel* class. The function *get256QamBer* computes and returns the BER relating to a 256-QAM modulation; the BER is evaluated by computing the Zeta function that depends on the SINR.

## 5.2 Massive MIMO module design and implementation

Once we modified the physical layer in order to support the specifications of the VHT standard including the error model and modulations, we designed the massive MIMO antenna modules. The antenna modules are defined in the *physicallayer* package, as depicted in **Figure 12**. Actually, the default antennas in the *physicallayer* package are:

- **ConstantGainAntenna:** A simple antenna having a unique basic parameter: the gain. As suggested by the name, the gain set in the configuration file remains constant, while a simulation run is executed.

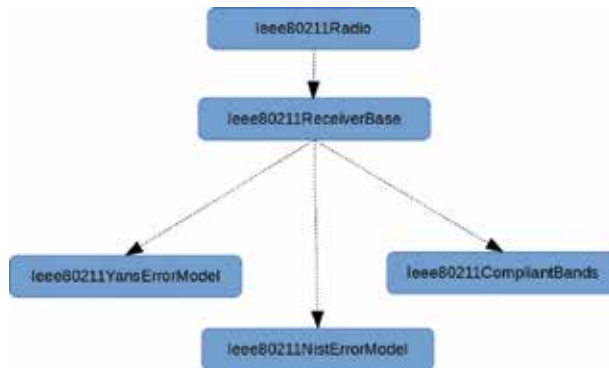


**Figure 13.**  
Error model designing at the receiver.

- **CosineAntenna:** It is the cosine pattern antenna designed in [32]. This model results very usefully for W-CDMA systems.
- **DipoleAntenna:** The well-known dipole antenna; it is possible to set in the configuration file the length of the dipole (expressed in meters).
- **InterpolatingAntenna:** This antenna model computes the gain in function of the direction of the signal, using linear interpolation.
- **IsotropicAntenna:** It is the classical omnidirectional/isotropic antenna; it provides for unity gain by radiating the signal at the same way toward all directions.
- **ParabolicAntenna:** This model is based on a parabolic approximation of the main lobe radiation pattern.

However, the detailed description of all kinds of antennas is beyond the scope of this chapter, which instead aims to illustrate the features of the designed massive MIMO modules.

**Listing 3** illustrates the main definition parameters of the *MassiveMIMOURPA* antenna module. Note that the module inherits the basic features of the *AntennaBase* module; besides the main antenna array parameters such as the *length* the *distance* and the *frequency* the module provides for the setting of the steering angle *thetazero* in order to support the beam piloting; as already mentioned in Section 3.1.1, *M* and *N* represent the number of elements to be placed on the y- and x-axis, respectively. As a further example, in order to understand the implementation of the logic operations of the modules, the following pseudocode illustrates a portion of the *MassiveMIMOURPA.cc* definition:

The algorithm in **Figure 14** depicts the main functions of the *MassiveMIMOHPA.cc* class. The function *getMaxGain* computes the maximum

```

1 double Ieee80211NistErrorModel::get256QamBer (double snr)
  const {
2   double z = std::sqrt (snr / (85.0 * 2.0));
3   double ber = 15.0 / 32.0 * 0.5 * erfc (z);
4   EV << "256-Qam" << " snr=" << snr << " ber=" << ber;
5   return ber; }
  
```

**Listing 2.**  
Nist error model, BER computation example.

```

1 module MassiveMIMOURPA extends AntennaBase {
2   parameters:
3     double length @unit(m); // length of the antenna
4     double distance; // distance between elements
5     double freq; // frequency
6     double thetazero; // steering angle
7     int M; //number of columns
8     int N; //number of rows
9     .....}
    
```

**Listing 3.**  
*MassiveMIMOURPA.ned* definition.

**Algorithm 1** MassiveMIMOUHPA.cc pseudo-code

```

1: procedure INITIALIZE(int stage)
2:   initialize the module
3: end procedure
1: procedure GETMAXGAIN
2:   double maxG;
3:   int numel = getNumAntennas();
4:   double numer = 4 * MP1 * numel * numel;
5:   maxG = 20 * log10(numer/risInt);
6:   return maxG;
7: end procedure
1: procedure COMPUTEGAIN(EulerAngles direction)
2:   const std::complex < double > i(0, 1);
3:   double heading = direction.alpha;
4:   for (int m=-emme; m<=emme ; ++m) do
5:     int val = (2*emme) - abs(m);
6:     sum2 = 0;
7:     for (int n=0; n<= val; ++n) do
8:       double aux = (double)n * (sin(heading) *
9:         cos(elevation) + betaM);
10:      complex <double> aux2 = exp(i * MP1 * aux);
11:      sum2 += aux2;
12:     end for
13:   end for
14:   return gain;
14: end procedure
1: procedure COMPUTEINTEGRAL
2:   double risInt = computes the double integral
3:   return risInt;
4: end procedure
    
```

**Figure 14.**  
*MassiveMIMOUHPA.cc* pseudo-code.

gain according to Eq. (10); the function *getNumAntennas* returns the total number of antennas of the massive MIMO; the result of double integral (given by the *risInt* variable) is evaluated by implementing the Simpson method in C++ in the function *computeIntegral*; Observe that the integral could be computed by using some mathematical software tools such as Matlab and then passed to *Omnet++*, but in this case, we decided to implement the evaluation in C++ because the computation is once and because the use of MATLAB with this kind of very complex antenna module could significantly slow down the simulation. Finally, the function *computeGain* evaluates the gain in function of the direction *EulerAngles* components and the steering angle according to Eq. (9) (that however does not consider the scan term); the portion of code of *computeGain* function that is shown in **Figure 14** is related to the implementation of the summations of Eq. (9).

### 5.3 Planar massive MIMO model validation

The validation of the designed models is accomplished by illustrating some log screens related to the debug runs and by analyzing some useful statistics extracted from the simulations. The following table includes the most important simulation set parameters.

The simulations have been accomplished by using 20 different seeds and extracting the confidence intervals obtained by the repetitions considering a confidence level set to 95%. The traffic is represented by user datagram protocol (UDP) data packets randomly generated (based on the simulation seed) by different couples of nodes. The number of spatial streams is set to 8. Therefore, most of the antenna parameters including the number of elements and the spacing in the system are the same used in [26], with the only exception that we also provide the beam steering angle setting. For simulations, we considered such data rates provided by the IEEE802.11ac standard in function of the number of spatial streams. In order to validate the model, the first test consists of the analysis of such run simulation logs.

**Figure 15** represents a portion of log extracted by a randomly chosen simulation run related to the case of URPA; the result of the log is printed on the console perspective of *Omnnet++*; the red rectangle highlights the main line of the log, which displays the result of the computed gain in function of the current angle; the main line synthesizes that the value of the gain corresponding to the angle of 43.59° is 41.96 dB; considering the steering angle of 45°, we can manually compute the maximum gain that is the gain corresponding to the maximum radiation angle (thus the steering angle) by using Eq. (10) and replacing the terms of the equation with the values used in **Table 1**:

$$G_{MAX}(\theta_0 = 45^\circ, \phi) = \frac{4\pi \times 90^2}{772.97} - \delta_{\theta_0} = 42.16 \text{ dB} \quad (13)$$

where  $\delta_{\theta_0}$  represents the attenuation in dB related to the steering angle with respect to the maximum gain corresponding to  $\theta_0 = 0^\circ$  (which is 42.39 dB). In Eq. (13), the value of 772.97 at the denominator is the result of the double integral computed by the simulator, using the Simpson method [33]. The gain value of

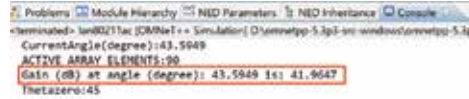


**Figure 15.**  
Portion of log extracted by simulations.

Antenna model	Massive MIMO URPA/HPA/CPA
Network standard	IEEE802.11ac
Num. of elements	90 (URPA), 91 (HPA), 91 (CPA)
Steering angle	45°
Elem. spacing	0.5 $\lambda$
Carrier freq.	5 GHz
Channel bandwidths [MHz]	20, 40, 80, 160
Data rates [Mbps]	from 57.8 to 6933.3
Traffic data type	UDP
Sim. area size	500 × 500 m
Sim. time	300 s

**Table 1.**  
Main simulation parameter set.

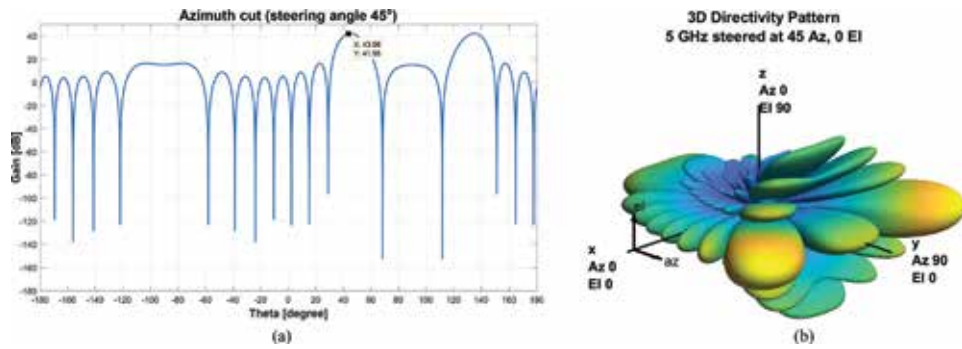


**Figure 16.**  
*Designed model radiation pattern: (a) Az cut rectangular plot, (b) 3D polar plot.*

41.9647 dB related to the angle of  $43.5949^\circ$  is almost about close to the maximum gain value, as we could expect, because the considered angle lies in the main lobe region.

For a further investigation, by using the sensor array analyzer tool provided by Matlab [29], it is possible to represent the radiation pattern plots related the designed massive MIMO URPA model. In **Figure 16(a)**, it can be observed that the obtained gain value, achieved corresponding to the angle of  $43.5949^\circ$  is very consistent with the obtained gain value related to log of **Figure 16**. Finally, **Figure 16(b)** illustrates the three-dimensional polar radiation pattern of the designed model.

## 6. Conclusions

This chapter illustrated the most recent research works in the simulation field about SAS and planar massive MIMO 5G technologies, with the aim to make an overview about research advances accomplished in this context. In this regard, after a brief analysis, useful for providing a minimum of theoretical knowledge about these kinds of technologies and applications, the chapter illustrated some aspects of the latest related works in this area. Relative to the experimental and practical analysis, one of the most used simulation tool, that is the Omnet++ simulator, has been considered. In this respect, it has been highlighted that, by modifying the default physical operations provided by the simulator in terms of power management, modulations and channel propagation model and at the same time, by designing a proper SAS or massive MIMO antenna module, it is possible to emulate a wireless network scenario consistent with the latest 5G standard specifications. Nevertheless, it also highlighted that, for enabling the simulator to support these kinds of technologies, it is required to implement the specifications defined by the most recent IEEE standards such as the 802.11n and 802.11ac to establish an interconnection between the logical operations and the physical simulation resources.

## **Author details**

Vincenzo Inzillo<sup>1\*</sup>, Floriano De Rango<sup>1</sup>, Luigi Zampogna<sup>1</sup> and Alfonso A. Quintana<sup>2</sup>

1 University of Calabria, Rende, CS, Italy

2 University of Malaga, Malaga, Spain

\*Address all correspondence to: [v.inzillo@dimes.unical.it](mailto:v.inzillo@dimes.unical.it)

## **IntechOpen**

---

© 2018 The Author(s). Licensee IntechOpen. This chapter is distributed under the terms of the Creative Commons Attribution License (<http://creativecommons.org/licenses/by/3.0>), which permits unrestricted use, distribution, and reproduction in any medium, provided the original work is properly cited. 

## References

- [1] Shu S et al. Synthesizing omnidirectional antenna patterns, received power and path loss from directional antennas for 5G millimeter-wave communications. In: Proceedings of the Global Communications Conference (GLOBECOM); IEEE; 2015
- [2] Sisodia S, Sandeep R. Performance evaluation of a table driven and on-demand routing protocol in energy constraint MANETs. In: Proceedings of International Conference on Computer Communication and Informatics (ICCCI); IEEE; 2013
- [3] Kumari N, Rohit K, Rohit B. energy efficient communication using reconfigurable directional antenna in MANET. *Procedia Computer Science*. 2018;125:194-200
- [4] Chen Y et al. Throughput analysis in mobile ad hoc networks with directional antennas. In: *Ad Hoc Networks* 11.3. Netherlands: Elsevier; 2013. pp. 1122-1135
- [5] Hong W et al. Study and prototyping of practically large-scale mmWave antenna systems for 5G cellular devices. *IEEE Communications Magazine*. 2014;52(9):63-69
- [6] Jain M, Agarwal R. Capacity and coverage enhancement of wireless communication using smart antenna system. In: Proceedings of International Conference on Advances in Electrical, Electronics, Information, Communication and Bio-Informatics; IEEE; 2016
- [7] Senapati A, Ghatak K, Roy J. A comparative study of adaptive beamforming techniques in smart antenna using LMS algorithm and its variants. In: Proceedings of International Conference on Computational Intelligence and Networks (CINE); IEEE; 2015
- [8] Lu L, Li G, et al. An overview of massive MIMO: Benefits and challenges. *IEEE Journal of Selected Topic in Signal Processing*. 2014;8(5):742-758
- [9] Gao X et al. Massive MIMO performance evaluation based on measured propagation data. *Transactions on Wireless Communications*. 2015;14(7): 3899-3911. IEEE
- [10] Molisch AF, Ratnam V, Han S, et al. Hybrid beamforming for massive MIMO: A survey. *IEEE Communications Magazine*. 2017;55(9):134-141
- [11] Bjornson E, Larsson E, Debbah M. Massive MIMO for maximal spectral efficiency: How many users and pilots should be allocated? *Transactions on Wireless Communications*. 2016;15(2):1293-1308. IEEE
- [12] Zhang H, Liu N, et al. Network slicing based 5G and future mobile networks: Mobility, resource management, and challenges. *IEEE Communications Magazine*. 2017;55(8):138-145
- [13] Zhang H, Sudhir S, Rohit N. Beamsteering in a spatial division multiple access (SDMA) system. U.S. Patent No. 8; Feb. 2014
- [14] Sahu R, Ravi M, Sumit S. Evaluation of adaptive beam forming algorithm of smart antenna. *International Journal of Emerging Technology and Advanced Engineering*. 2013;3(9):592-599
- [15] Mohammed JR, Sayidmarie KH. Sidelobe cancellation for uniformly excited planar array antennas by controlling the side elements. *IEEE Antennas and Wireless Propagation Letters*. 2014;13:987-990

- [16] Mohammed JR, Sayidmarie KH. Synthesizing asymmetric sidelobe pattern with steered nulling in non-uniformly excited linear arrays by controlling edge elements. *International Journal of Antennas and Propagation*. 2017;2017:9293031. 8 pages
- [17] Mohammed JR. Optimal null steering method in uniformly excited equally spaced linear array by optimizing two edge elements. *Electronics Letters*. 2017;53(11):835-837
- [18] Yan H, Cabric D. Digital predistortion for hybrid precoding architecture in millimeter-wave massive MIMO systems. In: *Proceedings of International Conference on Acoustics, Speech and Signal Processing (ICASSP)*; IEEE; 2017. pp. 3479-3483
- [19] Yang G, Ho C, Zhang R, Guan Y. Throughput optimization for massive MIMO systems powered by wireless energy transfer. *Journal on Selected Areas in Communications*. 2015;33(8):1640-1650. IEEE
- [20] Jungnickel V et al. The role of small cells, coordinated multipoint, and massive MIMO in 5G. *IEEE Communications Magazine*. 2014;52(5):44-51
- [21] Mailloux R. *Phased Array Antenna Handbook*. 2nd ed. Artech House, United States. 2005. Chapter 3
- [22] Vesa A, Alexi F, Balta H. Comparisons between 2D and 3D uniform array antennas. In: *Proceedings of the Federated Conference on Computer Science and Information Systems*; 2015. pp. 1285-1290
- [23] Nikolova N. *Linear Array Theory*. Part I, Lecture 13. Antertop. 2013. Available from: [http://www.antentop.org/017/files/tr\\_017.pdf](http://www.antentop.org/017/files/tr_017.pdf)
- [24] Harry L, Trees V. *Optimum Array Processing: Detection, Estimation, and Modulation Theory, Part IV*. United States: John Wiley & Sons; 2002. Chapter 2
- [25] Harry L, Trees V. *Optimum Array Processing: Detection, Estimation, and Modulation Theory, Part IV*. United States: John Wiley & Sons; 2002. Chapter 4
- [26] Tan W, Assimonis S, Matthaiou D, et al. Analysis of different planar antenna arrays for mmWave massive MIMO systems. In: *Proceedings of Vehicular Technology Conference (VTC)*; IEEE; 2017
- [27] Omnet++ Discrete Event Simulator; 5.3 release. <http://www.omnetpp.org>. Hungary, 2018
- [28] Inzillo V, De Rango F, Santamaria AF, Quintana Ariza A. A new switched beam smart antenna model for supporting asymmetrical communications extending inet OMNET++ framework. In: *Proceedings of International Symposium on Performance Evaluation of Computer and Telecommunication Systems (SPECTS)*; 2017. pp. 1-7
- [29] Matlab and Statistics Toolbox Release 2017a. United States: The Mathworks; 2017
- [30] Inzillo V, Santamaria AF, Quintana Ariza A. Integration of Omnet++ simulator with Matlab for realizing an adaptive beamforming system. In: *Proceedings of International Symposium on Distributed Simulation and Real Time Applications (DS-RT)*; IEEE/ACM; 2017. pp. 1-2
- [31] Pei G, Henderson T. Validation of OFDM Error Rate Model in ns-3. United States: Boeing Research Technology; 2010. pp. 1-15
- [32] Chunjian L. Efficient antenna patterns for three sector WCDMA systems (Master of Science thesis).



Goteborg, Sweden: Chalmers University  
of Technology; 2003

[33] He MX, Wang Q. New algorithm for  
GM (1, N) modeling based on Simpson  
formula. *Systems Engineering - Theory &  
Practice*. 2012;**33**(1):199-202



*Edited by Jafar Ramadhan Mohammed  
and Khalil Hassan Sayidmarie*

Array pattern optimization is a very important and necessary issue in the majority of modern communication systems in a variety of applications such as sonar, radar, navigation, wireless communications, and many other engineering fields. Classical methods for array pattern synthesis have worked mainly with analytical models that are linear, local and, thus, their performances were not optimum. They have always been designed with closed-form mathematical models. Unlike these analytical methods, the global optimization methods with powerful computing tools offer optimum solutions. During the last few years, the design of the antenna arrays has been a topic of significant research activity. This book presents recent advances in the field of array pattern optimization. It is targeted primarily toward students and researchers who want to be exposed to a wide variety of antenna array design and optimization. It includes five chapters as well as the introductory chapter. These five chapters are categorized into five different areas depending on the application. These applications are ordered to address interference suppression, electronic toll collection, mmWave and ultra-wideband, integrated antennas, and educational packages for modeling smart antenna for 5G wireless communications. The book has the advantage of providing a collection of applications that are entirely independent and self-contained; thus, the interested reader can choose any chapter and skip to another without losing continuity.

Published in London, UK

© 2019 IntechOpen  
© JoePhuriphath / iStock

**IntechOpen**

ISBN 978-1-83962-097-3



9 781839 620973

